Advanced Projection Ultrasound Imaging with CMOS-based Sensor Array: Development, Characterization, and Potential Medical Applications

Chu Chuan Liu

Dissertation submitted to the faculty of the Virginia Polytechnic Institute and State University in partial fulfillment of the requirements for the degree of

Doctor of Philosophy

In

Electrical Engineering

Dr. Yue Wang, Chair

Dr. Chris L. Wyatt

Dr. Jason Xuan

Dr. Ge Wang

Dr. Chang-Tien Lu

December 17, 2009

Arlington, Virginia

Keywords: Projection Ultrasound Imaging, PE-CMOS Sensor Array, Ultrasound Computed Tomography, Forward Ultrasound Scatter Modeling

Advanced Projection Ultrasound Imaging with CMOS-based Sensor Array: Development, Characterization, and Potential Medical Applications

Chu Chuan Liu

ABSTRACT

Since early 1960s, ultrasound has become one of the most widely used medical imaging device as a diagnostic tool or an image guider for surgical intervention because of its high portability, non-ionization, non-invasiveness and low cost. Although continuous improvements in commercial equipments have been underway for many years, almost all systems are developed with pulse-echo geometry. In this research, a newly invented ultrasound sensor array was incorporated into the developments of a projection imaging system. Three C-scan prototypes, which included prototypes #1, #2 and an ultrasound mammography system, were constructed. Systematic and Evaluative studies included ultrasound CT, 3-D ultrasound, and multi-modality investigations were also performed. Furthermore, a new analytical method to model ultrasound forward scattering distribution (FSD) was developed by employing a specific annular apparatus. After applying this method, the scattering-corrected C-scan images revealed more detail structures as compared to unprocessed images. This new analytical modelling approach is believed to be effective for most imaging systems operating in projection geometry.

In summary, while awaiting additional clinical validation, the C-scan ultrasound prototypes with the state-of-the-art PE-CMOS sensor arrays can provide veritable value and holds real and imminent promise in medical diagnostic imaging. Potential future uses of C-scan ultrasound include but not limit to computerized tomography, biopsy guidance, therapeutic device placing, foreign object detection, pediatric imaging, breast imaging, prostate imaging, human extremities imaging and live animal imaging. With continuous research and development, we believe that C-scan ultrasound has the potential to make a significant impact in the field of medical ultrasound imaging.

Dedication

To My Family

Acknowledgements

Thanks for the joint educational program between Virginia Polytechnic Institute and State University and Georgetown University Medical Center (GUMC), it has been a great opportunity to work with my academic advisor, Dr. Yue Wang, The Grant A. Dove Professor of Electrical and Computer Engineering, VT; my research advisor, Dr. Shih-Chung Ben Lo, Professor of Radiology, GUMC; and the engineering team at Imperium Inc. Ultrasound imaging prototypes equipped with PE-CMOS two-dimensional ultrasound sensor were made available for the project as arranged by Drs. Yue Wang and Shih-Chung Ben Lo. It has been an invaluable learning experience to have participated in the development of the projection ultrasound imaging prototypes and worked alongside Imperium's engineers in the image characteristics generated from PE-CMOS sensor array. I appreciate the medical and clinical guidance provided by my mentor Dr. Matthew T. Freedman, senior radiologist and Associate Professor of Oncology in the Division of Cancer Genetics and Epidemiology at GUMC, to accomplish this research. Furthermore, special thanks to Dr. Paul C. Wang, director of Biomedical Nuclear Magnetic Resonance Laboratory at Howard University; Dr. Erini V. Makariou at Betty Lou Ourisman Breast Health Center at Georgetown University Hospital; and Ms. Anita Sarcone at Georgetown University Hospital for their supports. Finally, I would like to express my thanks to Dr. Henry Yeh for his editorial help in my dissertation.

This research of the dissertation was supported in part by an US Army research grant (No. DAMD17-0101-0197) and an NIH/NIBIB Grants (No. EB002130).

Contents

1. Introduction ……..1

1.1 Motivations……. 1

1.2 The Objectives, State of Problems, and Strategies……. 3

1.2.1 Specific Objectives…… 3

1.2.2 Statement of the Problems and Strategies……. 6

1.3 Organization of Dissertation……... 8

2. Projection Ultrasound Imaging: Developments and Analyses…….. 10

2.1 Fundamentals of Ultrasound…….…… 11

2.1.1 Ultrasound…… 11

2.1.2 Reflection and Refraction…….……... 11

2.1.3 Attenuation.....13

2.1.4 Scattering.....15

2.1.5 Diffraction……..... 16

2.2 Piezoelectric Material in Ultrasound Imaging..... 17

2.3 Medical Ultrasound Imaging..... 18

2.3.1 A-scan (Amplitude Scan).....19

2.3.2 B-scan (Brightness Scan)..... 21

2.3.3 C-scan (Constant Depth Scan)..... 22

2.4 Developments of Projection Ultrasound Imaging Prototypes.....23

2.4.1 The First Generation Two-Dimensional Sensor Array I-100..... 23

2.4.2 The Fourth Generation Two-Dimensional Sensor Array I-400..... 24

2.4.3 Acoustic Lens Design (*Information extracted from Imperium Inc.*)..... 25

2.4.4 Concept of Projection C-scan Ultrasound Imaging..... 26

2.4.5 The First C-scan Ultrasound Prototype with I-100 PE-CMOS Array..... 27

2.4.6 The Second C-scan Ultrasound Prototype with I-400 PE-CMOS Array..... 28

2.5 Preliminary Evaluations of C-scan Prototypes..... 29

2.5.1 Uniformity.....29

2.5.2 Spatial Resolution..... 30

2.5.3 Dynamic Range.....32

2.5.4 Modulation Transfer Function..... 34

2.6 Breast Phantom Study and *in vitro* Study..... 37

2.6.1 Cyst and Tumor Phantom..... 37

2.6.2 Microcalcification Phantom..... 39

2.6.3 Human Objects..... 41

2.7 Summary..... 42

3. Modeling Ultrasound Forward Scattering: Characteristic and Measurement..... 44

3.1 Mathematical Review of Scattering..... 45

3.1.1 Single Scatterer in Homogeneous Medium..... 45

3.1.2 The Helmholtz Equation and Green's Function Approach..... 47

3.1.3 Incident Plane Waves and Born Approximation..... 50

3.2 Twersky's Multiple Scattering Model..... 52

3.3 Modeling Ultrasound Forward Scattering Distribution..... 54

3.3.1 Concept of Modeling Forward Scattering in C-scan Ultrasound.....54

3.4 Analytical Approach for Modeling Ultrasound Intensity Distribution..... 56

3.4.1 Breast Mimicking Phantom and Annular Aperture…… 56

3.4.2 Design of the Measurement..... 58

3.4.3 Solution for the Forward Scattering Distributions (Arc Scattering Model)..... 60

3.4.4 Algebraic Reconstruction Techniques (ART) Estimation..... 61

3.5 Image Restoration..... 63

3.6 Analyses of Images and Scattering Distributions..... 64

3.6.1 Analyses of Ultrasound Ring Images..... 64

3.6.2 Forward Scattering Distribution and Modulation Transfer Function.....66

3.7 Validation of Computed Coefficients.....69

3.7.1 Verification Using Twersky's General Scattering Model..... 69

3.7.2 Verification Using Edge Scattering Model and Point Spread Function. 71

3.8 Ultrasound Image Restoration of Tissue Specimens..... 74

3.9 Summary.....77

4. Ultrasound Computerized Tomography..... 79

4.1 Computerized Tomography.....80

4.1.1 Fundamentals of Computerized Tomography..... 80

4.1.2 Projection and Fourier Slice Theorem..... 81

4.1.3 Filter Back-projection (Frequency domain)..... 83

4.1.4 Filter Back-projection (Spatial domain)..... 85

4.1.5 Ultrasound CT..... 86

4.2 Ultrasound CT Studies using C-scan prototype #1..... 88

4.2.1 System Configuration of First UCT Study..... 88

4.2.2 Test Targets and C-scan Images..... 89

4.2.3 Ultrasound Attenuation in C-scan Geometry..... 89

4.2.4 Initial UCT Images..... 90

4.2.5 Circular Shadow and the Compensation Method..... 91

4.2.6 Shadow-Compensated UCT Results..... 92

4.2.7 Analyses of UCT Images..... 94

4.2.8 Additional UCT Study – Animal Tissue Specimen..... 95

4.3 Ultrasound CT Studies using C-scan prototype #2..... 96

4.3.1 System Configuration of the Second UCT Study..... 96

4.3.2 Test Targets and C-scan Images..... 98

4.3.3 Ultrasound CT Phantom Images..... 99

4.3.4 Analyses of UCT Images..... 101

4.3.5 Potential 3-D Ultrasound Images..... 101

4.4 Summary..... 103

5. New Sensor Capabilities and Potential Medical Applications..... .105

5.1 Biopsy Simulation using C-scan Prototype #1..... 105

5.2 Foreign Object in Soft-tissue Study (C-scan Prototype #2)..... 107

5.2.1 Design of the Study.....108
5.2.2 The C-scan Images..... 111
5.2.3 The B-Scan Ultrasound Images.....112
5.2.4 The Film-based Radiograph and CR Images..... 113
5.2.5 Visual Comparisons of the C-scan Images and the X-ray Images..... 114
5.2.6 Quantitative Analyses..... 115
5.3 Small Animal Study.....117
5.3.1 Configuration of the Study..... 117
5.3.2 Small Animal MRI..... 118
5.3.3 Image Analyses..... 119
5.4 C-scan Ultrasound Mammography Study..... 121
5.4.1 Initial Breast Phantom Test..... 122
5.4.2 *In vivo* C-scan Images of Human Breast..... 123
5.5 Potential *In vitro* Breast Tissue Examination..... 124
5.5.1 *In vitro* with C-scan Prototype #2.....124
5.5.2 *In vitro* Breast Imaging with C-scan Mammography Prototype.....125
5.6 Summary..... 127
6. Contributions, Future Works, and Conclusions..... 129
6.1 Summary of Original Contributions..... 129
6.1.1 Hardware Developments.....130
6.1.2 Software Developments..... 131
6.1.3 Exploration of Potential Medical Applications.....132
6.2 Future Works.....133

6.2.1 Ultrasound Forward Scattering Data Bank..... 133

6.2.2 Investigate Alternative Filtering Methods for Scatter-reduced C-scan Images..... 133

6.2.3 Continuous Development of PE-CMOS array..... 134

6.2.4 C-scan Ultrasound in Reflection Geometry..... 135

6.3 Conclusions..... 137

Appendix A 138

Bibliography..... 143

List of Figures

Figure 2-1. Diagram of sound waves..... 11
Figure 2-2. Reflection and refraction for non-perpendicular beam incidence.....… 12
Figure 2-3. Wave Scattering from a distribution of small objects..……..15
Figure 2-4. Illustrations of Rayleigh scattering and Mie scattering with an incident wave. ……... 16
Figure 2-5. The wavefronts and beam shape from an aperture insolated by plane waves… …….…….. 17
Figure 2-6. Piezoelectric effects of the reversible relation between a mechanical pressure and an electrical voltage: an applied mechanical stress will generate a voltage and an applied voltage will change the shape of the material……...18
Figure 2-7. Diagram of ultrasound A-scan system.……..……19
Figure 2-8. A sample A-scan display with several reflectors (generated by ACOUSTOCAM^{TM} system, Imperium Inc.).……..……..19
Figure 2-9. Diagram of ultrasound B-Scan system.…….…….20
Figure 2-10. A sample image of a mouse abdomen using a high resolution B-mode ultrasound system (scanned by Ms. Anita Sarcone at Georgetown University Hospital).21
Figure 2-11. Typical types of B-scan arrays: (A) linear array, (B) convex array and (C) phase array..…….…….. 22
Figure 2-12. Basic configuration of a C-Scan system in projection geometry..…….. 22
Figure 2-13. A C-scan image of a human finger in projection mode (acquired by C-scan prototype #2 operated at 5MHz)…….... 23

Figure 2-14. (A) Schematic of the I-100 sensor array. (B) Picture of the 128 x 128 assembled array.……..……... 24
Figure 2-15. Frequency responsive ranges of I-400 sensor array.……24
Figure 2-16. (A) Schematic of the I-400 sensor array. (B) Picture of the I-400 sensor array.…….. 25
Figure 2-17. Ray tracing plots for (A) the compound acoustic lens originally designed for I-100 array and (B) the newly compact design for I-400 array with reduced lens elements. (C) Plots of the compact lens system while a parallel ultrasound beam is used..……. 26
Figure 2-18. Projection ultrasound imaging system and image acquisition..……... 27
Figure 2-19. Laboratory system configuration of the C-Scan prototype #1……. 27
Figure 2-20. (A) The system design and (B) a picture of the completely C-scan prototype #2. (C) A closer view of the components (left to right): the detecting unit, lens system, and transducer……..……..28
Figure 2-21. (A) Inactive pixels. (B) Marked inactive pixels. (C) Original image. (D) Processed image.……30
Figure 2-22. (A) Fan shape pattern with seven wires at 250 microns. (B) Diagram of the spatial resolution phantom. Wires were embedded in a background of Zerdine™……...31
Figure 2-23. Ultrasound images of the phantom and the horizontal intensity plots of the marked lines, which represented ~350 microns and ~500 microns wire-to-wire spacing, obtained by (A) prototype #1 and (B) prototype #2 separately...……..... 31
Figure 2-24. Dynamic range phantom..... 32
Figure 2-25. C-scan images of each attenuation step. Note that the images of last two steps were not displayed because their attenuations were too high.....33
Figure 2-26. Step intensity distributions of I-100 and I-400 sensor arrays..... 34
Figure 2-27. (A)(B) Edge ultrasound images taken by I-100 and I-400 sensor arrays respectively. (C) Plots of the normalized PSF and (D) the MTF curves of two sensor arrays.....36
Figure 2-28. Design of the cyst and tumor phantom..... 38
Figure 2-29. Ultrasound images of 5mm cysts and tumors obtained by I-100 and I-400 sensor arrays. (A)(C) Cysts mimicking spheres with 0.06 $dB \cdot cm^{-1} \cdot MHz^{-1}$ on the left

and 0.15 $dB \cdot cm^{-1} \cdot MHz^{-1}$ on the right. (B)(D) Tumor mimicking spheres with 0.5 $dB \cdot cm^{-1} \cdot MHz^{-1}$ on the left and 0.8 $dB \cdot cm^{-1} \cdot MHz^{-1}$ on the right..... 39
Figure 2-30. A series of C-scan images taken from a CIRS Model 52 breast phantom by the C-scan prototype#2 operating at 7.5 MHz. The destructed structures in the breast phantom are also observable.....39
Figure 2-31. Design of the microcalcification phantom..... 40
Figure 2-32. Ultrasound images of the microcalcification phantoms. (A)(C) 0.7-0.85mm clustered calcifications (B)(D) 0.42-0.45mm clustered calcifications. Note: The phantom employed in (C) and (D) had lower contrast (-3dB) between objects and background.... 40
Figure 2-33. Finger images obtained by C-scan prototype #2: (A) Finger image taken by a 5MHz transducer. (B) Area 2cm below the top of a finger by 5MHz transducer. (C) Area 4cm below the top of a finger by 5MHz transducer. (D) Finger image taken by 7.5MHz transducer. (E) Area 2cm below the top of a finger by 7.5MHz transducer. (F) Area 4cm below the top of a finger by 7.5MHz transducer..... 41
Figure 3-1. The scattering geometry for a single scatterer in a homogeneous medium... 46
Figure 3-2. Plane waves being incident upon a slab of object with thickness d..... 53
Figure 3-3. The ultrasound primary beam, attenuated energy and scattering energy in C-scan geometry..... 55
Figure 3-4. Picture of the three soft-tissue mimicking phantoms made of Zerdine™ with thicknesses of 12mm, 23mm and 31mm..... 57
Figure 3-5. Upper: Photograph of a series of annular apertures with different sizes of opening gaps. Lower: Sample C-scan images of several apertures obtained without target (water only)..... 58
Figure 3-6. (A) Diagram of the experiment configuration. (B) The residual of the attenuated primary beams and the scattered energy coming out from the annular aperture. 59
Figure 3-7. The ultrasound primary beam and scattering energy propagated through an annular aperture to the detector array..... 60
Figure 3-8. An illustration of the arc scattering model. The upper plane is the scattering surface of the phantom and the lower plane is the detecting array. r is the radius of the

annular aperture; L the distance between the two planes; and l the distance from the arc scattering location to the detecting pixel..... 60
Figure 3-9. (A)(C)(E) Ultrasound ring images of 12mm, 23mm, and 31mm soft-tissue phantoms respectively. Each image is at 200x200 pixels. (B)(D)(F) Plots of average radius intensity distribution..... 65
Figure 3-10. The computed FSD coefficients (top) and normalized unit scattering distributions (bottom) of phantoms with thicknesses of 12mm, 23mm and 31mm..... 67
Figure 3-11. (A)(B)(C) The restored intensity plots vs. the original average radius intensity for 12mm, 23mm, and 31mm phantoms, respectively..... 68
Figure 3-12. MTF curves for 12mm, 23mm and 31mm phantoms at 5MHz..... 69
Figure 3-13. Plots of intensity ratio vs. object thickness. Dash curves represent the intensity ratio with different portions of scattering coefficients within the total attenuation. The solid line represents the intensity ratio of attenuation effects along the primary incident beam without considering multiple scattering effects. The star markers represent the intensity ratios of the three phantoms of thickness 12mm, 23mm and 31mm. 70
Figure 3-14. Plot of the average scattering intensity ratio vs. the object's thickness based on Twersky's model..... 71
Figure 3-15. An illustration of the edge scattering model: The upper plane (z = L) is the scattering surface of the phantom and the lower plane (z = 0) is the detecting array. L is the distance between the two planes and l is the distance from the edge scattering location to the detecting pixel p 72
Figure 3-16. (A)(C)(E) Edge ultrasound images for the three phantoms with thicknesses of 12mm, 23mm and 31mm respectively. (B)(D)(F) Plots of the normalized edge-based PSFs (dash lines) and FSD-based PSFs (solid lines)..... 73
Figure 3-17. Plots of intensity distributions of FSD-based PSF and FSD for the 12mm phantom..... 74
Figure 3-18. (A) The ultrasound image of a human finger tip, which has approximate dimensions of 2.0cm × 1.7cm × 1.4cm, generated by the C-scan prototype #2 at 5MHz. (B) Its processed image with the 12mm scattering filter.....75

Figure 3-19. (A) Photograph of a breast tissue specimen which has approximate dimensions of 2.5cm × 2.0cm × 1.1cm. (B) The ultrasound image of the specimen directly taken by the C-scan prototype #2. (C) Its processed image using the 12mm scattering filter..... 75
Figure 3-20. (A) Photograph of a breast reduction tissue specimens consisted of fat, fibrous tissue, mammary glandular tissue and blood vessel with approximate dimensions of 2.5cm × 2.0cm × 0.9cm. (B) The ultrasound image of the specimen directly taken by the C-scan prototype #2. (C) Its processed image using the 12mm scattering filter.....76
Figure 3-21. (A) The original C-scan image, (B) the scatter-reduced image, and (C) the horizontal intensities plots of the indicated edge patterns in the original image (dashed line) and the processed image (solid line)..... 77
Figure 4-1. A simple parallel beam scanning system..... 81
Figure 4-2. Formation of the projection..... 81
Figure 4-3. Diagram of the Fourier slice theorem..... 82
Figure 4-4. Center overlaps of the projections in 2-D frequency space..... 84
Figure 4-5. Magnitude response of back-projection filters: (1) Ram-Lak (ramp) filter, (2) Shepp-Logan filter, (3) Cosine filter, and (4) Hamming filter..... 84
Figure 4-6. Diagram of back-projection in the spatial domain.....85
Figure 4-7. The flowchart of the ultrasound CT procedures: (A) Attenuation profiles calculated from C-scan images. (B) Extract linear information for one detector line from all images to form (C) a sinogram. (D) The reconstructed ultrasound CT result.....87
Figure 4-8. Example of a sinogram which associates with the reconstruction of the corresponding ultrasound CT slice. 400 projections were taken from 180 degree with each increment of 0.45 degree.....87
Figure 4-9. Closer view of the laboratory ultrasound CT system configuration with C-scan prototype #1.....88
Figure 4-10. (A) A photo picture of the test target and its contents. (B) The center cross section slice of test target No.1 in drawing and its C-scan ultrasound image at the initial viewing angle. (C) The center cross section of test target No.2 in drawing and its C-scan ultrasound image at the initial viewing angle..... 89
Figure 4-11. The attenuation profile of the test target with primary ultrasound.....90

Figure 4-12. Initial reconstructed ultrasound CT results: (A) for test target No.1; (B) for test target No. 2. Each ultrasound CT image represents a slice of the target in the position of the dashed line on the C-scan image..... 91
Figure 4-13. (A) The circular shadow model, (B) its inversed image, and (C) the computer reprojection method.....91
Figure 4-14. Comparison of the initial results and the shadow-compensated images for the two targets. Each ultrasound CT image represents a slice of the target in the position of the dashed line on the C-scan image.....93
Figure 4-15. Diagram of the off-axis rotation problem..... 94
Figure 4-16. (A) The test sample with marked portion was used in the experiment. The dimensions of the sample are ~2.5cm in length, ~0.6cm in diameter (tip of the chicken finger) and ~0.9cm in diameter (bottom of the sample). (B) The transmission ultrasound image of the testing sample..... 95
Figure 4-17. Reconstructed ultrasound CT images. Each ultrasound CT image represents a slice of the target in the position of the dashed line on the C-scan image.....96
Figure 4-18. A picture of the new portable ultrasound CT system's configuration.....97
Figure 4-19. A skeleton diagram of the new scanning geometry.....98
Figure 4-20. Materials which were used to fabricate test phantoms.....99
Figure 4-21. (A) The center cross-sectional diagram of phantom No.1 and its C-scan ultrasound image at the initial viewing angle. Notice that the small black area on the right of the image is an air bubble. (B) The center cross-sectional diagram of phantom No.2 and its C-scan ultrasound image at the initial viewing angle..... 99
Figure 4-22. Original reconstructed and "scattering-corrected" ultrasound CT images of test phantoms: (A) test phantom No.1; (B) for test phantom No. 2. Each ultrasound CT image represents a slice of the target in the position of the dashed line on the C-scan images..... 100
Figure 4-23. Alternate views for the 3-D ultrasound image of the test phantom No.1. (A) Generated from original ultrasound CT images and (B) from "scattering-corrected" ultrasound CT images.....102

Figure 4-24. Alternate views for the 3-D ultrasound model of phantom No.2. (A) Generated from original ultrasound CT images and (B) from “scattering-corrected” ultrasound CT images.....103
Figure 5-1. Ultrasound images of the biopsy simulation. The needle first punctured the target (A) and (B), then removed (C), and punctured the target again (D) and (E). The needle was rotated clockwise from (E) to (F). This operation pushed the mass on the right upper corner out of the focal plane.....106
Figure 5-2. These images are of a specific detail of simulated tumors in the CIRS breast phantom Model 52 designed for tissue equivalent ultrasound needle biopsy training. The imaged detail is a spherical echogenic object simulating solid tumor within the phantom. The detail has been punctured multiple times under ultrasound guidance leaving multiple needle tracks.....107
Figure 5-3. The soft-tissue sample composed of skin, fat, and muscle tissues.....109
Figure 5-4. The foreign objects used in the experiment: objects of No.1 are bamboo skewers; Nos. 2, 3, and 7 are plastic sticks; Nos. 4 and 5 are aluminum alloys; No.6 are pieces of glass. Note that only one object in each category was selected..... 109
Figure 5-5. The source emitting direction for all image modalities was perpendicular to the inserting direction..... 110
Figure 5-6. A series of C-scan images for the foreign objects contained in the porcine tissue sample. The bold numbers indicate the specific foreign object according to Table 5-1..... 111
Figure 5-7. The stitched C-scan image of the porcine sample and foreign objects (above). The image reveals a section of the porcine sample (below). The arrows 1 to 7 point to the locations of the foreign objects inserted in the pork. The arrow numbering corresponds to the particular foreign objects as listed in Table 5-1..... 112
Figure 5-8. The B-scan ultrasound images of the porcine tissue with foreign objects. The arrows point to the locations of the foreign objects inserted in the porcine tissue. The numbers indicate the foreign objects and correspond to Table 5-1..... 113
Figure 5-9. (A) The film-based radiograph obtained at 44kVP. (B) The CR image obtained at 40kVP. The arrows point to the locations of the foreign objects inserted in the porcine tissue. The numbers indicate the foreign objects corresponding to Table 5-1...113

Figure 5-10. Displays of the inverted C-scan image with film-based radiograph and CR image: (A) C-scan image vs. film-based radiograph and (B) C-scan image vs. CR image. The numbers indicate the foreign objects corresponding to Table 5-1.....115
Figure 5-11. A diagram of the system configuration for the small animal study.....118
Figure 5-12. Small animal MRI system (4.7 T) at Howard University..... 119
Figure 5-13. Mouse heart beating images and breath movements captured at 3.5 MHz. 119
Figure 5-14. The composite C-scan image (left) and the MRI image (right) of a whole mouse body. Individual C-scan images were obtained at 5MHz.....120
Figure 5-15. The configurations of first C-scan ultrasound mammography prototype. (A) The front view of the complete system. (B) The closer view of the transducer (top) and detecting unit (bottom). (C) The side view of the system with a breast phantom.....121
Figure 5-16. Pictures of the CIRS compressible breast phantom model 013; top view (A) and side view (B).....122
Figure 5-17. C-scan images of three simulated tumor with 0.5cm, 0.9cm and 1.2cm contained in the breast phantom using the C-scan ultrasound mammography prototype. 123
Figure 5-18. C-scan breast images of human breasts acquired by the ultrasound mammography prototype using I-400 sensor array operated at 4MHz.....123
Figure 5-19. Pictures of sample specimens from breast reduction surgery.....124
Figure 5-20. C-scan ultrasound images of human breast specimens obtained by the C-scan prototype #2. The image of skin pores from the skin specimen shown in Figure 5-17 (on the right of the second row) is marked above..... 125
Figure 5-21. Photographs of the breast specimens and their corresponding C-scan images. Arrows indicates the suspicious area in the C-scan images..... 126
Figure 6-1. (A) The sample scatter-reduced C-scan image. (B)(C)(D) Initial results processed by 3x3, 5x5, and 7x7 Wiener filter kernels. (E) Intensity plots of an edge pattern contained in those processed images.....134
Figure 6-2. A diagram of the laboratory reflection system.....136
Figure 6-3. A blueprint of the handheld C-scan reflection ultrasound device.....137

List of Tables

Table 2-1. Typical attenuation of human tissues at 1 MHz dB cm^{-1} 15
Table 5-1. Parameters and acoustic properties of test objects..... 110
Table 5-2. CNR values of each foreign object for all imaging modalities..... 116

List of Acronyms

1-D	One-Dimensional
2-D	Two-Dimensional
3-D	Three-Dimensional
AFSM	Average Forward Scatter Modeling
BNMR	Biomedical Nuclear Magnetic Resonance
BCRP	Army Breast Cancer Research Program
CAT	Computerized Axial Tomography
CIRS	Computerized Imaging Reference Systems
CNR	Contrast-to-Noise Ratio
CR	Computed Radiography
CT	Computerized Tomography
ECG	Electrocardiogram
ESF	Edge Spread Function
FBP	Filtered Backprojection
FSD	Forward Scattering Distribution
GUMC	Georgetown University Medical Center

IRC	Intensity Reflection Coefficient
ISIS	Imaging Science and Information Systems
ITC	Intensity Transmission Coefficient
MTF	Modulation Transfer Function
MRI	Magnetic Resonance Imaging
NIH	National Institutes of Health
NIBIB	National Institute of Biomedical Imaging and Bioengineering
OCT	Optical Coherence Tomography
PE-CMOS	Piezoelectric Complementary Metal Oxide Semiconductor
PET	Positron Emission Tomography
PGA	Pin Grid Array
PSF	Point Spread Function
PVDF	Polyvinylidene Fluoride
PZT	Piezoelectric lead Zirconate Titanate
ROI	Region of Interest
ROIC	Read-Out Integrated Circuit
SBIR	Small Business Innovation Research
SFR	Signal Frequency Response
SPECT	Single Photon Emission Computed Tomography
STTR	Small Business Technology Transfer Program
SRI	Speckle Reduction Imaging

Chapter 1

Introduction

1.1 Motivations

Ultrasound imaging has been widely used in medical practice and diagnostic applications due to the following four principal advantages: (1) ultrasound is a relatively inexpensive imaging modality comparing to computerized tomography and magnetic resonance imaging (MRI), (2) ultrasound can generate real-time images, (3) ultrasound is radiation-free and (4) ultrasound procedures are non-invasive. Current conventional B-scan ultrasound systems are widely used in vivo for medical diagnostic purposes particularly in abdominal, pelvic, heart, breast, and fetal imaging[1-5]. B-scan ultrasound devices have been developed for more than 40 years. However, speckle patterns, which are the result of constructive and destructive interference of echo signals, and tomographic image characteristics make it necessary to require specific training (and practice) in order to understand the technique for diagnostic purposes[6-10]. Recently, some innovative approaches have been developed to tackle speckle issues such as General Electric's (GE) speckle reduction imaging (SRI), Philips' XRES adaptive imaging processing, and Philips' SonoCT real-time compound imaging, etc[11-14].

These attempts show improvements in the overall B-scan image quality for clinical diagnosis.

In year 2001, I received an Army Breast Cancer Research Program (BCRP) Pre-doctoral award (under grant number DAMD17-01-1-0197) entitled "*Computerized Tomography of Projection Ultrasound*". The main objectives of this project were to develop scanning mechanism, data acquisition, and reconstruction algorithms for the development of *Projection Ultrasound Computerized Tomography* breast imaging system. This ultrasound prototype differs from conventional ultrasound devices in many ways, particularly in ultrasound signal acquisition. As an initial research objective, the understanding of the ultrasound paths and signal formation, image characterization, physical evaluating and initial pre-clinical testing of the prototype were investigated.

The key component of the first ultrasound C-scan prototype is the sensing array, which is patented by Imperium Inc. This unique two-dimensional sensor differs in the structure from conventional ultrasound sensor. The piezoelectric sensor array is made in such a way that the piezoelectric material coats onto a complementary metal oxide semiconductor (CMOS) detector[15, 16]. The PE-CMOS sensor array can produce ultrasound images with high resolution, and have good sensitivity and good contrast performance. This research has been directed towards understanding and examining this novel ultrasound system and developing new techniques appropriate for medical applications.

Unlike conventional ultrasound, the projection ultrasound prototypes separate the ultrasound transmitter from the receiver permitting each to be optimized separately. The conventional ultrasound B-scan system provides a cross-sectional image in the x and z (depth) directions. Instead, ultrasound image generated from the PE-CMOS sensor array is in x and y directions with following characteristics: (a) speckle free, (b) completely non-invasive, (c) high data rate (up to 60 full image frames per second), (d) variable magnification / field of view (zoom in, zoom out), (e) fluoroscopy-like image, and (f) high resolution (~350 microns)[17]. The sensor has a wide range of responsive frequency

from 3KHz to 25MHz and an adaptability to be configured as projection or reflection geometry. These properties have allowed the new sensor array to contribute additional values for further development of medical ultrasound in the field of diagnostic imaging. As well, the attenuation characteristics recorded by this novel system, which are currently unavailable in B-scan systems, could provide additional clinical information. With an engineering design, a hand-held system can be made similar to that of commercial camcorders for potential medical uses.

With the professional supports from my mentors and Imperium's engineers, (in the developments of C-scan (projection) ultrasound imaging prototypes,) my research programs were conducted by first evaluating the image characteristics of the ultrasound imaging prototypes. Then I focused on the projection imaging systems' calibration and image processing in both hardware design and software developments. Projection ultrasound prototypes were fabricated to seek potential medical applications such as ultrasound computerized tomography (CT), ultrasound mammography, breast cancer imaging, bone fractures imaging, detecting foreign objects in soft-tissues, and small animal imaging [18-21]. These prototypes were specifically designed to combine the advantages of using ultrasound as a non-ionized energy source with projection geometry similar to a standard radiographic imaging system. Furthermore, an analytic method was developed to model and quantitatively reduce the multiple scattering effects from the acquired C-scan ultrasound images.

Projection ultrasound systems had limited clinical use in the past. However, with the developments in this research, particularly in the advanced sensor array and archiving our research objectives, we have made the new C-scan imaging potentially useful in the field of medical ultrasound.

1.2 The Objectives, State of Problems, and Strategies

1.2.1 Specific Objectives

The ultimate goal of this research was to develop a diagnostic-capable imaging system in a projection geometry utilizing ultrasound as well as the state-of-the-art piezoelectric coated two-dimensional (2-D) CMOS sensor. The system should provide more information of image characteristics to facilitate detecting, identifying, and localizing abnormalities in tissues than conventional ultrasound reflective systems. Moreover, the ultrasound imaging system will have the potential to be competitive to other imaging modalities in image quality, cost, and the potential to generate three-dimensional ultrasound images.

There are four specific objectives of this research project:

Objective 1: Quantitatively evaluate the PE-CMOS ultrasound sensors

The PE-CMOS sensor array is the most important element of the projection ultrasound prototypes. It differs from existing ultrasound probes in that conventional probes integrate both functions of the transmitting and receiving the ultrasound signals in a single unit. As a result, images generated by the prototype have different image characteristics than conventional B-scan ultrasound. Thus, standard ultrasound phantoms designed for reflection systems were not suitable for evaluating our system. For C-scan imaging, ultrasound phantoms had to be redesigned and manufactured. The evaluation studies included basic image performances such as spatial resolution, dynamic range, contrast resolution, and tissue detectbility detectability as well as other important ultrasound physical characteristics in medical uses.

Objective 2: Model the forward ultrasound scattering so that primary ultrasound beam can be restored for signal quantification purposes

The proposed ultrasound imaging prototypes were configured as projection geometries (C-scan mode, refer to Section 2.3.3). It thus had different noise and scattering characteristics than seen with conventional ultrasound devices. C-scan ultrasound images were acquired when the acoustic energy transmitted through the

imaging target was detected. In this C-scan system, the transmitted signal was focused by a compound acoustic lens system onto the sensor array. In conventional B-scan ultrasound, the focusing operates by the concave design of the transducer or the excitation delay of each element on a linear transducer. With lens focusing in C-scan geometry, a portion of the multi-directional scattering energy is detected along with the primary through-transmission energy. The scattering energy is therefore considered as one of the factors which causes blurry ultrasound images in the C-scan geometry. Based on the extension of the concept of Twersky's *multiple scattering theory*, a new analytic method of modeling the ultrasound forward scattering distribution (FSD) was developed.

Objective 3: Develop ultrasound computerized tomography with a planar source involving scattering effects

Computerized tomography is an imaging technique to visualize the internal structure reconstructed from a set of profiles obtained around the target. For example, the X-ray Computerized Axial Tomography (also known as CAT scan) is a commonly used diagnostic method to generate a 2-D image from 1-D profiles taken around an axis of rotation. A 3-D volume image is then integrated by these 2-D images of the target. With an x-ray cone beam scan method, however, a 3-D volume image can be reconstructed from 2-D profiles directly. In this research, the ultrasound CT techniques were investigated and initial studies were performed to evaluate the potential ability of generating 3-D ultrasound image using the proposed C-scan imaging prototypes. Ultrasound cross-sectional images of targets were reconstructed by the projection ultrasound images obtained around 180 degree with planar beams. Based on 2-D cross-sectional images, 3-D ultrasound images of the targets could then be constructed. Moreover, with the development of new scattering-corrective processing, details in the 3-D model could be clearly observed.

Objective 4: Explore potential medical applications

In this research project, potential medical utilizations of C-scan ultrasound were investigated and conducted. In order to explore possible applications, two C-scan ultrasound prototypes using the I-400 PE-CMOS sensor array were fabricated: (1) C-scan ultrasound mammography prototype (dry), and (2) multipurpose C-scan ultrasound imaging prototype #2 (water bath). The C-scan ultrasound mammography prototype has a similar configuration as the X-ray mammography machine and contains two paddles to compress the breast for imaging. C-scan prototype #2 has a compact design with the rotation ability to obtain ultrasound images around the target. These C-scan imaging prototypes are potentially suitable for imaging breast, infant, parts of the human extremities, as well as tissue specimens.

1.2.2 Statement of the Problems and Strategies

The proposed ultrasound C-scan imaging prototypes has a unique design of projection geometry, uses a plane wave transducer as the source and a 2-D sensor as the receiver, and has an acoustic lens system to focus the transmitted ultrasound energy onto the sensor. Most of the previous theoretical approaches developed for the conventional ultrasound pulse-echo (reflection) system could not be (directly) applied to this C-scan ultrasound imaging system. This resulted in a series of physical problems in the images which had to be analyzed and corresponding solutions had to be developed. Those problems can be categorized into two scientific/technical issues and a medical application issue.

- **Technical issue in modeling the ultrasound scattering effect.**

With the projection geometric configuration, ultrasound attenuation and scattering effects are the major influences on the quality of ultrasound image. Attenuation can be calculated by the basic acoustic properties of the target but the multi-directional scattering energy is difficult to be distinguished from the detected ultrasound energy.

Attenuation influences the brightness of the image while scattering may be one of the major causes of unsharpness on the image. Our proposed C-scan prototypes employed planar 2-D sensor-array with acoustic lens systems to focus the through-transmission energy. Scattering effect, which exhibits in C-scan ultrasound with 2-D detector, is much higher than that in the conventional B-scan with linear probe.

Under this circumstance, reduction of the scattering effect is an important task in this research. We employed a certain type of apparatus to confine the through-transmission energy in order to analyze and model the multi-scattering components within the received data. In addition, I developed an analytical method to model the forward scattering (refer to Chapter 3).

- **Technical issue in performing the planar projection ultrasound CT and accurate image reconstruction**

Computerized tomography is a mature technology in the field of medical imaging. It is performed by employing tomographic reconstruction from scanned profiles around the target. The preliminary ultrasound CT study performed by prototype #1 (refer to Chapter 4) indicated that an extremely accurate system configuration is required to generate high resolution CT images, especially the pixel width of the sensor array is 85 microns. Due to the influences in the combination of accurate configuration requirement, planar source with 2-D sensor array and the acoustics lens system, artifacts and shadowing effects are however found when performing the initial study using the C-scan prototype #1.

In order to reduce artifacts and shadowing effects of the CT image, a shadow compensation method using a re-projection technique was applied to enhance the initial ultrasound CT results. In addition, a more accurate system configuration was redesigned and fabricated for the second C-scan prototype with a new generation of PE-CMOS sensor array. Based on the integration with a computer-controlled high torque stepping

motor and a new compact lens system, the C-scan prototype #2 executed a series of initial phantom investigations for the ultrasound CT (refer to Chapter 4).

- **Exploring medical applications for the C-scan ultrasound**

Due to the lack of effective sensor, projection ultrasound used to be considered as less applicable in medical applications than conventional B-scan systems. However, recent developments in advanced acoustic research and sensor technology, the new PE-CMOS sensor array was introduced to the proposed C-scan ultrasound prototypes. The C-scan ultrasound provides acoustic attenuation information in the projective image characteristics instead of reflective signals. Thus, the plan of the investigations must be carefully designed to discover its potential uses in medicine.

Based on supports obtained from my mentors, Drs. Matthew T. Freedman, S-C Benedict Lo, and Yue Wang, we had designed and performed initial breast imaging investigations; breast specimen examinations; *in vivo*, *in vitro* and phantom studies using the C-scan prototypes. Moreover, comparative investigations between C-scan prototypes and other imaging modalities including B-scan ultrasound, conventional radiography, computed radiography, and MRI were conducted in the research. This is intended to investigate whether there are specific advantages of C-scan ultrasound over other existing image modalities.

1.3 Organization of Dissertation

The fundamentals and developments of ultrasound imaging are going to be addressed in Chapter 2. The concept of projection ultrasound and two imaging prototypes will be discussed. Introductions of the preliminary phantom, *in vitro*, and *in vivo* evaluations performed by these prototypes are presented; image characteristics including image uniformity, spatial resolution, contrast, dynamic range, and modulation transfer function are discussed.

Scattering phenomena of the conditions in single and multiple scatters will be addressed in Chapter 3. Base on the projection geometry, scattering effect is considered to be one of the major causes for blurry C-scan images. An analytical method is then developed to determine the forward scattering distribution in C-scan geometry. Investigations and verifications are studied using a soft tissue mimicking phantom and an annular aperture. Image restoration in obtaining scatter-corrected C-scan image will be performed.

Chapter 4 addresses the fundamentals and experiments of ultrasound CT technology. The computerized axial tomography, as known as CAT scan, is the most common application with the use of radiography. However, radiation is a concern that limits the number of times of the examination that a patient can receive in a certain period. The proposed C-scan prototypes have the same geometry configuration as radiographic devices. Therefore, we want to investigate and analyze the possibility in performing CT scan by employing C-scan prototypes. Preliminary phantom studies and 3-D ultrasound images are discussed in Chapter 4.

Chapter 5 addresses the investigations that we performed to explore potential medical applications for C-scan ultrasound. Comparative studies against other imaging modalities such as conventional B-scan ultrasound, radiography, computed radiography and MRI are illustrated. Additionally, several potential studies in biopsy, breast tissue examination, and C-scan ultrasound mammography are also included.

Chapter 6 summarizes the original contributions of the dissertation and presents conclusions for the conducted researches in developing the C-scan ultrasound imaging system.

Chapter 2

Projection Ultrasound Imaging: Developments and Analyses

In order to utilize ultrasound as the source of an imaging system in projection geometry, major phenomena occur when waves propagate through an object. These phenomena include reflection and refraction on the boundaries between media, attenuation (absorption and scatter) within the object, and diffraction (interference between waves) along the propagation path. Base on the piezoelectric materials, ultrasound sensors have been developed and incorporated into medical imaging systems. The concepts of three common imaging modes, i.e. amplitude scan, brightness scan, and constant-depth scan, will be discussed as well.

During this research, we have developed and fabricated C-scan imaging prototypes with newly developed two-dimensional piezoelectric-based sensors. Quantitative and systematic tests and analyses of the imaging characteristics produced by these prototypes have been investigated. A series of phantom, *in vitro*, and *in vivo* evaluations were performed to obtain image characteristics including image uniformity,

spatial resolution, contrast resolution, dynamic range, and modulation transfer function. These parameters have produced highly valuable yet first-hand data about the unique properties of the C-scan systems.

2.1 Fundamentals of Ultrasound

2.1.1 Ultrasound

Acoustic (sound) wave is defined as vibrations of molecules of a medium that is capable for the propagation of sound wave. The vibrations of the medium are characterized by local pressure change, or the distance that the molecules are moving. When a sound wave is propagated through a medium, a series of areas of compression and rarefactions of molecules transmit acoustic energy (see Figure 2-1). The molecules or particles themselves do not travel from the source of the vibration to the receiver of the sound wave.

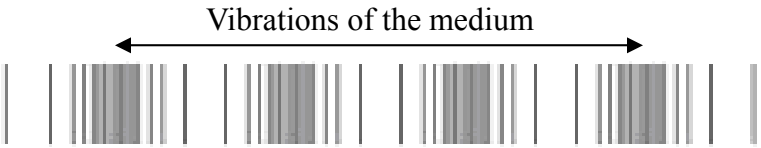

Figure 2-1. Diagram of sound waves.

The rate at which molecules vibrate in the medium equals the frequency of the sound wave, and is measured in hertz (cycles/second). As the frequency increases to about 20 kHz, the sound is no longer audible. Above this frequency, the vibration is known as ultrasound.

2.1.2 Reflection and Refraction (Transmission)

Wherever an ultrasound beam is incident upon an interface formed by two mediums having different acoustic impedances, some of the energy in the beam will be reflected and the remainder will be transmitted. The amplitude of the reflected wave depends on the difference between the acoustic impedances of the two media that form

the interface.

For non-perpendicular beam incidence on an interface, the reflected beam does not travel back toward the source, but instead travels off at an angle θ_r, which is equal to the incident angle θ_i, only in the opposite direction. The direction of the refracted (transmitted) beam is governed by Snell's Law[22].

It is determined by the speed of sound on the incident beam side of the interface, c_1; to the speed of sound on transmitted beam side of the interface, c_2; and to the incident beam direction , θ_i, according to the following relationship:

$$\frac{\sin\theta_t}{\sin\theta_i} = \frac{c_2}{c_1} \qquad (2.1)$$

Figure 2-2 shows the relationship of the incident, reflected, and refracted (transmitted) beams at the interface between two media.

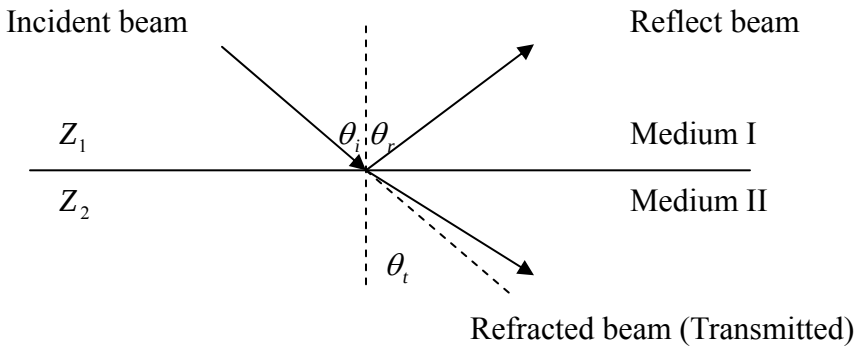

Figure 2-2. Reflection and refraction for non-perpendicular beam incidence.

The ratio of the reflected intensity I_r to the incident intensity I_i is called the intensity reflection coefficient (IRC), and is given by R; the ratio of the refracted intensity I_t to the incident intensity I_i is called the intensity transmission coefficient (ITC), and is given by T. These ratios depend on the difference in acoustic impedance at the interface, according to the expression[23, 24]:

$$R = \frac{I_r}{I_i} = \left(\frac{Z_1 \cos\theta_t - Z_2 \cos\theta_r}{Z_1 \cos\theta_t + Z_2 \cos\theta_r}\right)^2 \qquad (2.2)$$

and $$T = (1 - R) = \frac{I_t}{I_i} = \frac{4 Z_2 Z_1 \cos\theta_t \cos\theta_r}{(Z_1 \cos\theta_t + Z_2 \cos\theta_r)^2} \qquad (2.3)$$

where Z_1 is the acoustic impedance of medium I, Z_2 is acoustic impedance of medium II, T is the intensity transmission coefficient, and R is the intensity reflection coefficient.

For a normal incidence ($\theta_i = 0$), the reflected beam and transmitted beam are also perpendicular to the interface (no refraction). The reflection and transmission coefficients become:

$$R = \left(\frac{Z_1 - Z_2}{Z_1 + Z_2}\right)^2 \quad , \quad T = (1 - R) = \frac{4 Z_1 Z_2}{(Z_1 + Z_2)^2} \qquad (2.4)$$

The amount of energy in the reflected beam depends upon the difference in impedances between the two media. The greater the difference is, the greater the reflected energy. On the other hand, the transmitted energy would be more if the difference is smaller.

2.1.3 Attenuation

Attenuation is the reduction of an ultrasound wave's intensity during its passage through a medium. In general, there are two main attenuation mechanisms of absorption and scattering.

Ultrasound is lost from the beam by absorption in which the energy of the ultrasound is converted into heat. The loss due to absorption increases with frequency. Absorption results from relaxation mechanisms which may be described as follows: All substances contain a certain amount of potential energy. This can be mechanical energy when the substance is under compression or tension; chemical energy, where the

chemical bonding of molecules to form particular substances can alter with the absorption or release of energy; or structural energy concerned with the particular configuration of molecules, which again can be changed with the absorption or release of energy.

Scattering is another way that an ultrasound wave can lose energy as it passes through tissue. Ultrasound energy can be redirected in all directions within the tissue. Therefore, the ultrasound detector may not be able to receive all of the transmitted or reflected energy in the same direction as the propagating ultrasound wave.

When an ultrasound plane wave (or a non-diverging beam) passes through a uniform sample with no boundaries at which reflection and refraction can take place, then the ultrasound attenuation can occur only by absorption and scattering. Thus the ultrasound attenuation process may be quantified for a medium. The equation describing the change of intensity with depth is:

$$I(z) = I_0 \exp(-\alpha z) \qquad (2.5)$$

where $I(z)$ is the intensity at depth z, I_0 is the intensity at depth zero, and α is the attenuation coefficient of the medium. The frequency dependence of the attenuation coefficient is[25, 26]:

$$\alpha = \alpha_0 f^n \qquad (2.6)$$

where f is the ultrasound frequency (in MHz) and α_0 is the attenuation coefficient at 1MHz. The factor n is close to 1 for most tissues in the frequency range of 1MHz to 10MHz[27]. The unit of attenuation coefficient is usually expressed by $dB \cdot cm^{-1} \cdot MHz^{-1}$. The dB is calculated as an intensity ratio, as follows:

$$dB = 10 \log_{10}(\frac{I}{I_0}) \qquad (2.7)$$

The typical attenuation coefficients of human tissues are shown in Table 2-1.

Table I. Typical attenuation of human tissues at 1 MHz dB cm^{-1} [22, 28].

Tissue	Density (g/m^3)	Attenuation
Fat	~0.92	0.5-0.8
Muscle	1.04~1.06	0.9-1.8
Liver	1.05~1.07	0.6-0.9
Blood	~1.06	0.2

2.1.4 Scattering

When the ultrasound wave is incident upon particles with a size smaller than or comparable with a wavelength, ultrasound scattering occurs. Waves that are scattered tend to travel in all directions (see Figure 2-3). In medical ultrasound, the scattering phenomenon produces much of the diagnostic information seen in ultrasound imaging by creating the grey scale texture in images. Changes in scattering result in changes in the brightness of the image, and therefore are useful in delineating both normal and abnormal structures.

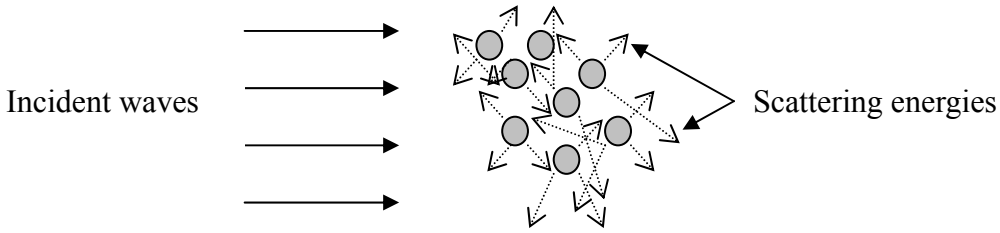

Figure 2-3. Wave Scattering from a distribution of small objects.

According to the size of the single scattering particle and the wavelength of incident wave (λ), the scattering factor *x* can be defined as

$$x = \frac{2\pi \cdot d}{\lambda} \qquad (2.8)$$

where the *d* is the characteristic dimension of the particle. The scattering phenomenon can be categorized by the following:

(1) when $x << 1$, Rayleigh scattering

(2) when $x \approx 1$, Mie scattering

(3) when $x >> 1$, Geometric scattering

Rayleigh scattering indicates that when the particle is much smaller than the wavelength of the incident wave, scattered energy will be sprayed in all directions and does not depend on the geometry of the particle [28, 29]; Mie scattering describes that due to the larger size of the particle, the scattering distribution may have more concentrated scattering angle[30, 31]; Geometric scattering states that with the particle's size factor much larger than the incident wavelength, the scattering distribution is highly dependent on the geometry of the particle[32]. Graphical illustrations are shown in Figure 2-4.

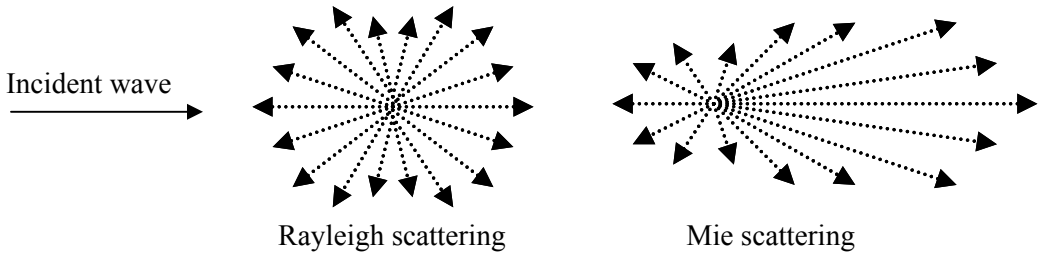

Figure 2-4. Illustrations of Rayleigh scattering and Mie scattering with an incident wave.

Since the scattered waves spread in all directions, the scattering ultrasound energy detected from a volume containing small scatterers is not highly dependent on the orientation of individual scatterer but depends on the number of scatterers per unit volume, the size of the particle, acoustic impedance changes at the particle's interface, and the frequency of the incident waves. Further discussions of the scattering effects for the proposed ultrasound imaging prototype are presented in chapter 3.

2.1.5 Diffraction

When a continuous plane wave encounters an obstacle, e.g. an aperture, the wavefronts of the emitting waves that propagate through the aperture will become more convex, leading to beam divergence, and they will resemble spherical surfaces centered

on the aperture (see Figure 2-5.). The point at which the beam starts to diverge and the degree of divergence are dependent on the ratio of the aperture dimensions to the wavelength of the sound. The superposition or interference of the bending waves may cause a series of maxima and minima intensities on the detector plane. However, when the wave encounters obstructing objects with complex structures, the diffraction phenomena can result in complicated patterns of varying intensity.

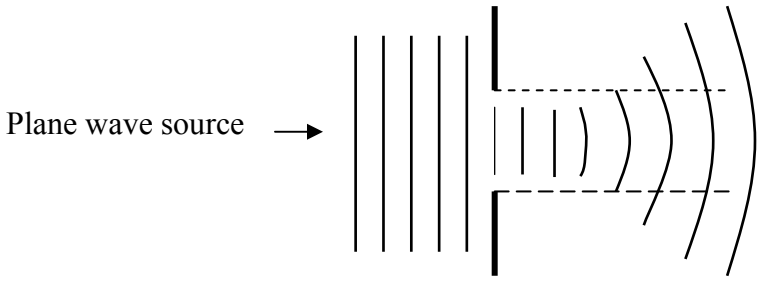

Figure 2-5. The wavefronts and beam shape from an aperture insolated by plane waves.

2.2 Piezoelectric Material in Ultrasound Imaging

Certain substances change their dimensions when an electric field is applied across them, and they develop electric charges on their surfaces when deformed. This type of material is called piezoelectric material[33]. An ultrasound transducer can be constructed by depositing metallic electrodes on a thin plate of piezoelectric material. If the plate is compressed by an ultrasound wave, then a potential difference will be detected across the electrodes, and if the plate is stretched, then the potential difference will reverse in sign. Moreover, it is also reversible if an electric voltage is applied to the plate with one polarity, the plate will change its shape by a small amount (up to a 4% change in volume). Therefore, the piezoelectric material is capable of generating ultrasound waves (as a transducer) or detecting ultrasound (as a receiver). Illustrations of the piezoelectric effect are diagramed in Figure 2-6.

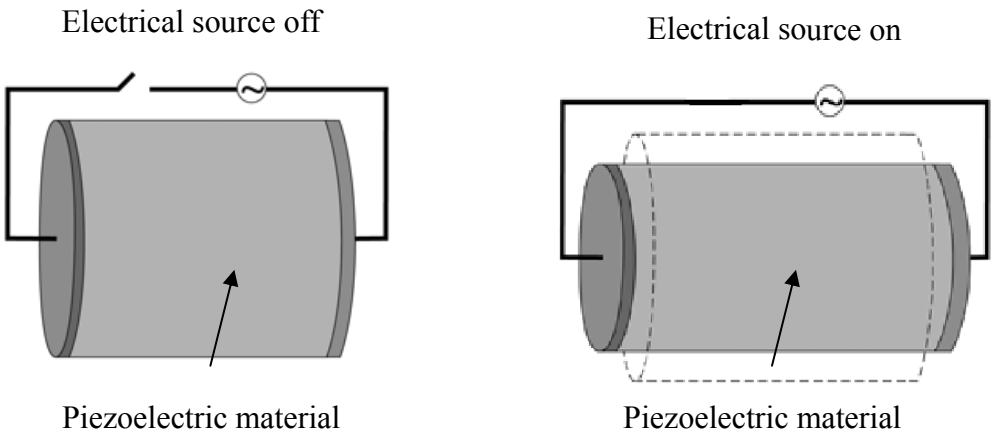

Figure 2-6. Piezoelectric effects of the reversible relation between a mechanical pressure and an electrical voltage: an applied mechanical stress will generate a voltage and an applied voltage will change the shape of the material.

Several man-made ceramic materials create the piezoelectric effects in their crystal structures, such like barium titanate ($BaTiO_3$), lead titanate ($PbTiO_3$), lead zirconate titanate ($Pb[Zr_xTi_{1-x}]O_3$ $0<x<1$, as known as PZT), potassium niobate ($KNbO_3$), lithium niobate ($LiNbO_3$), lithium tantalate ($LiTaO_3$), sodium tungstate (Na_2WO_3), etc[34]. There is a different type of material, polymer, which shows piezoelectricity by attracting and distracting the long-chain molecule structures when an electric field is applied. The piezoelectric materials now most commonly used in medical ultrasound imaging are the ceramic-based lead zirconate titanate, known as PZT, and the polymer-based polyvinylidene fluoride, PVDF[35, 36].

2.3 Medical Ultrasound Imaging

Ultrasound imaging, also called ultrasound scanning or sonography, is a method of obtaining images from inside the human body using high-frequency sound waves. The reflected or transmitted sound wave are recorded and displayed as a real-time visual image. There are three commonly used acquisition modes in ultrasound imaging: A-scan, B-scan, and C-scan (reflection and projection configurations)[36-38]. The frequency of medical ultrasound imaging usually ranges from 1MHz to 15 MHz.

2.3.1 A-scan (Amplitude Scan)

The A-scan, or amplitude scan, is the simplest pulse-echo instrument, displaying received and reflected echo amplitude as a graph against time (see Figure 2-7). In pulse-echo ultrasound, the time it takes to transmit and reflect the pulse is used to infer reflector distances, so the A-scan display also measures echo amplitude versus distance. The instrument is usually calibrated at a pulse propagation speed of 1540 m/s for determining reflector depth from the transit time. A-scan ultrasound is used to judge the depth of an organ, or otherwise to assess an organ's dimensions, and has been used extensively in midline echoencephalography and ophthalmologic scanning. In some instruments, particularly those used in ophthalmology, A-scan may be the only echo display format provided. It enables precise transducer-to-reflector distance measurements, and it reveals the relative echogenic or scatter level of structures within the transducer beam. Figure 2-8 illustrates a sample of ultrasound A-scan display.

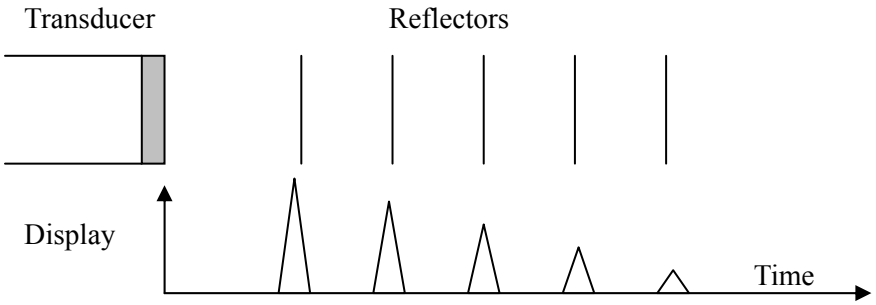

Figure 2-7. Diagram of ultrasound A-scan system.

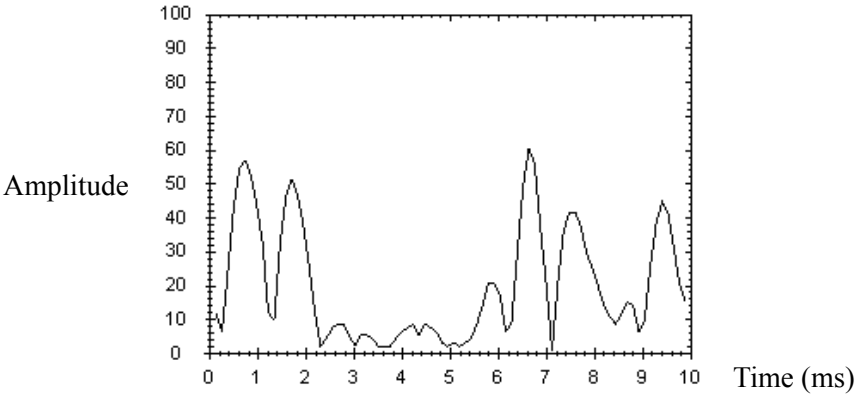

Figure 2-8. A sample A-scan display with several reflectors (generated by ACOUSTOCAM^{TM} system, Imperium Inc.).

2.3.2 B-scan (Brightness Scan)

Using the information generated by the A-scan instrument regarding the position of the reflectors along the ultrasound beam, the B-scan, or brightness scan, displays the echo signals and converts them to intensity modulated dots on the viewing screen (see Figure 2-9) The distance between a dot position and the start of the trace represents the distance form the transducer to the reflector. In the brightness modulation display, the grey scale corresponds to the brightness of the B-scan display according to the amplitude of the individual echo signals. In B-scan ultrasound, the greater the amplitude of the echo is, the brighter the displayed dot will show. Usually the B-scan ultrasound image is a "White object on a black background" format. This configuration is commonly used in all types of pulse-echo ultrasound imaging. Figure 2-10 shows a sample B-scan mouse image.

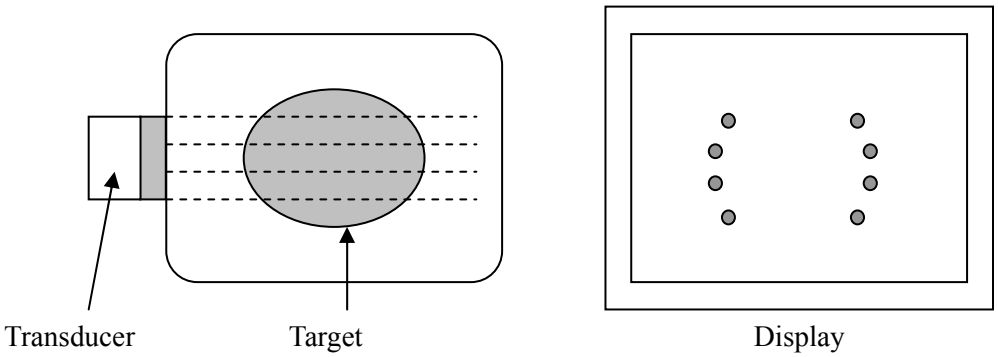

Figure 2-9. Diagram of ultrasound B-Scan system.

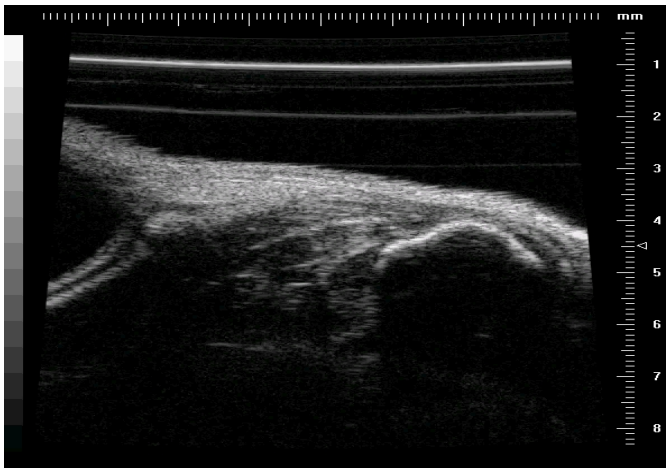

Figure 2-10. A sample image of a mouse abdomen using a high resolution B-mode ultrasound system (scanned by Ms. Anita Sarcone at Georgetown University Hospital).

B-scan ultrasound transducer (or called probe) has a variety of the basic configurations[39, 40] such as linear array, convex array, and phase array (see Figure 2-11). Linear array acquires rectangular ultrasound image by exciting a set of elements on the array to situate over the imaging region. The beam is moved over the imaging region and reflects back to the array for display. Commonly, a linear array can be quite large in order to cover a sufficient region of interest (ROI). For a convex array, a larger area can be scanned with a smaller array. The method of focusing and beam sweeping during transmit and receive is the same as for the linear array, and a substantial number of elements on the array (usually 128 or 256) is employed. However, linear and convex arrays are often too large to image the heart when probing between the ribs. A phase array, which is basically a linear array with electric phase control units, operates by delaying the excitation of the individual elements on the array, so an initially concave beam shape can be emitted to cover a bigger imaging region. Therefore, a phase array is an appropriate solution for its smaller array size and a larger field of view.

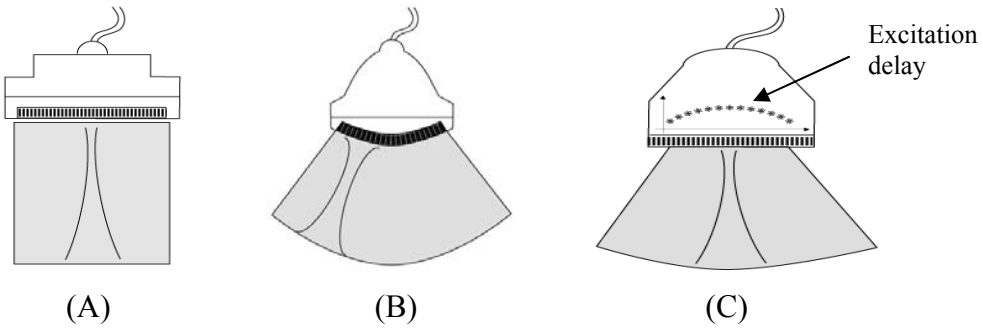

Figure 2-11. Typical types of B-scan arrays: (A) linear array, (B) convex array and (C) phase array.

2.3.3 C-Scan (Constant-depth Scan)

In general, C-scan ultrasound images are acquired by collecting information at a constant depth of an imaging target perpendicular to the direction of ultrasound wave propagation. Each transmitted beam is sampled by a fixed time to obtain image at a constant depth. When a C-scan system is set in projection geometry with a planer transducer and a separate receiver, ultrasound images are obtained by placing the receiving component across from a transducer within a water-bath or equivalent environment. This type of ultrasound imaging does not rely upon the detection of the reflected echoes from the interface. The ultrasound beam is transmitted from one side of the target through to the receiving detector on the opposite side. The received ultrasound energy is converted into an intensity-modulated signal for signal processing. Figure 2-12 shows the diagram of the basic components needed for a C-Scan imaging system and Figure 2-13 illustrates a finger C-scan image sample.

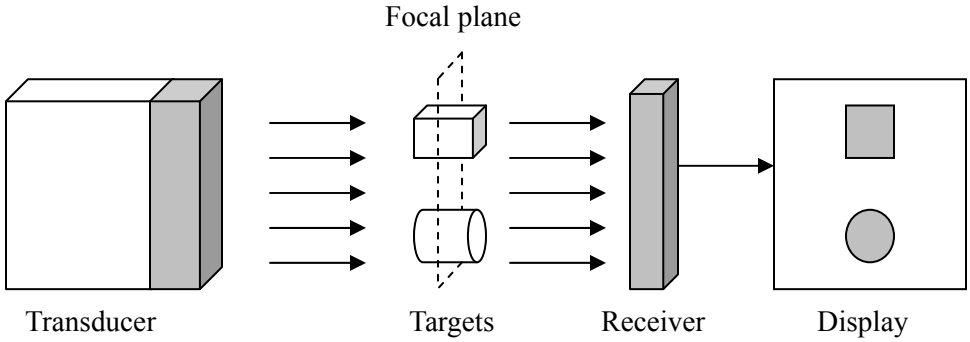

Figure 2-12. Basic configuration of a C-Scan system in projection geometry.

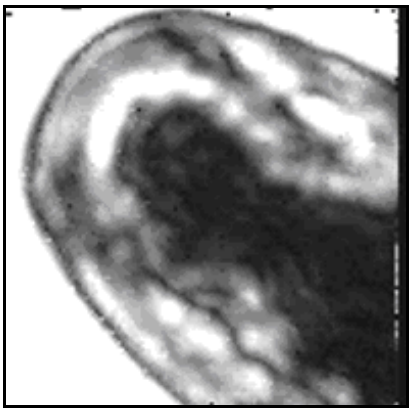

Figure 2-13. A C-scan image of a human finger in projection mode (acquired by C-scan prototype #2 operated at 5MHz).

2.4 Developments of Projection Ultrasound Imaging Prototypes

2.4.1 The First Generation Two-Dimensional Sensor Array I-100

The key component of the first projection ultrasound imaging system is the first generation ultrasound micro-array, model I-100, manufactured by Imperium. The design of the sensor array is unique and novel, and has never been used previously for a medical imaging system. The sensor array is composed of 128×128 pixel elements (16,384) in a 1cm × 1cm area with 100 microns spaced center-to-center. The sketch and a picture of the sensor array are exhibited in Figure 2-14(A) and 2-14(B) respectively. This array incorporates piezoelectric material, PVDF, which is deposited onto a silicon readout multiplexer through complementary metal oxide semiconductor (CMOS) processing, and a transducer array which is made by spin-coating a pre-selected, read-out integrated circuit (ROIC) array with PVDF copolymer approximately 10 microns thick. The ultrasound energy which strikes the piezoelectric layer creates voltages which are interpreted by the multiplexer for subsequent imaging processing and real-time video display. This sensor array is capable of responding in a wide range of ultrasound frequencies from 1MHz to 10MHz.

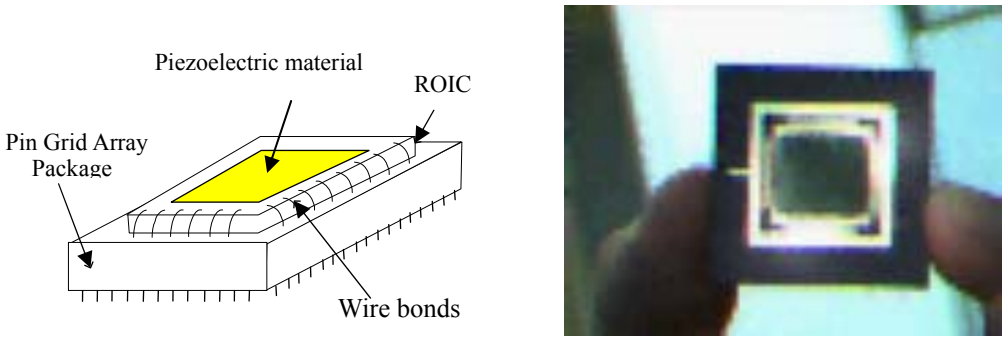

Figure 2-14. (A) Schematic of the I-100 sensor array. (B) Picture of the 128 x 128 assembled array.

2.4.2 The Fourth Generation Two-Dimensional Sensor Array I-400

After considerable efforts to develop the new technology in depositing the piezoelectric material onto the array, a fourth generation sensor array was produced in 2004. A more evenly distributed layer (~6 microns) of the piezoelectric material, PVDF, was coated onto the CMOS based array. The sensitivity of the 4th PE-CMOS array was significantly improved to detect at frequencies ranged from 3KHz to 25MHz (see Figure 2-15). Uniform coating of the PVDF prevents inactive or uneven reaction in detecting elements on the array. The sensor array consists of 128 × 128 elements and each element is 85 μm². The schematic of the fourth generation sensor array and its picture are shown in Figure 2-16 (A) and (B) respectively.

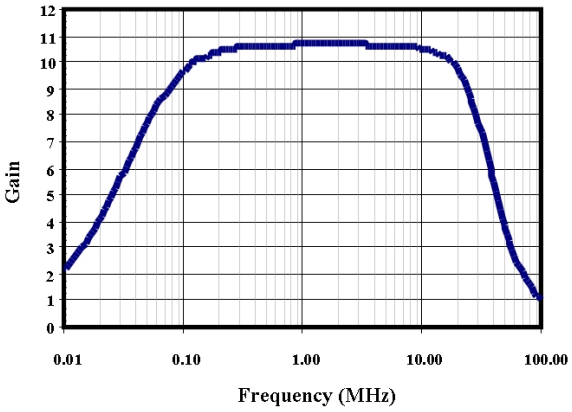

Figure 2-15. Frequency responsive ranges of I-400 sensor array.

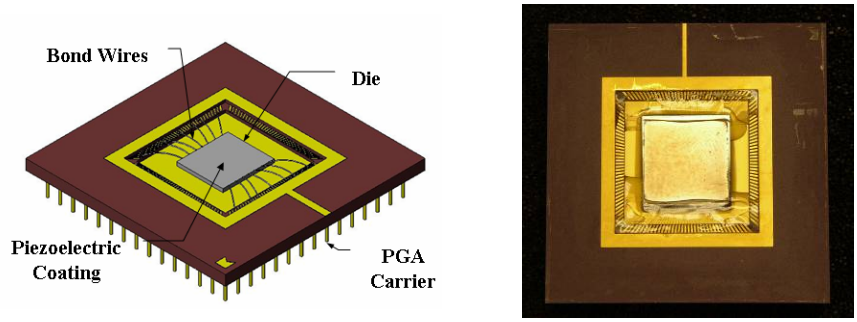

(A) (B)

Figure 2-16. (A) Schematic of the I-400 sensor array. (B) Picture of the I-400 sensor array.

2.4.3 Acoustic Lens Design (*Information extracted from Imperium Acustocom*)

In order to focus the incident ultrasound energy and project the entire field of view over the surface of the PE-CMOS sensor array, a compound acoustic lens system must be employed. Two types of lens systems are specially designed and fabricated for the I-100 and I-400 sensor arrays by Ultra-Acoustics, Inc., Woodstock, GA. The lens system designed for the I-400 array has less elements and shorter physical lengths between lenses for better compact design capability.

Optical Path Difference (OPD) curves are employed to design the acoustic lens systems. The OPD curves plot the acoustic path differences for rays which launch from the same field point and arrive at the focal plane of the sensor array, as illustrated in the ray tracing diagrams in Figure 2-17 (A) and (B). The original lens system requires a longer distance between lenses and thus limits the design of physical sizes for the first generation C-scan prototype. Figure 2-17(C) illustrates a ray tracing diagram of the new compact lens system while a parallel ultrasound beam is used. In the design for the I-400 sensor array, both lenses are made of Styraclear with a refractive index of 0.63 and have the identical size of 7.0cm in diameter. The fixed distance between the front flat lens surface and the sensor array is 8.6cm. To change the focus, the rear lens can be moved forward/ backward with the sensor array fixed at the same place.

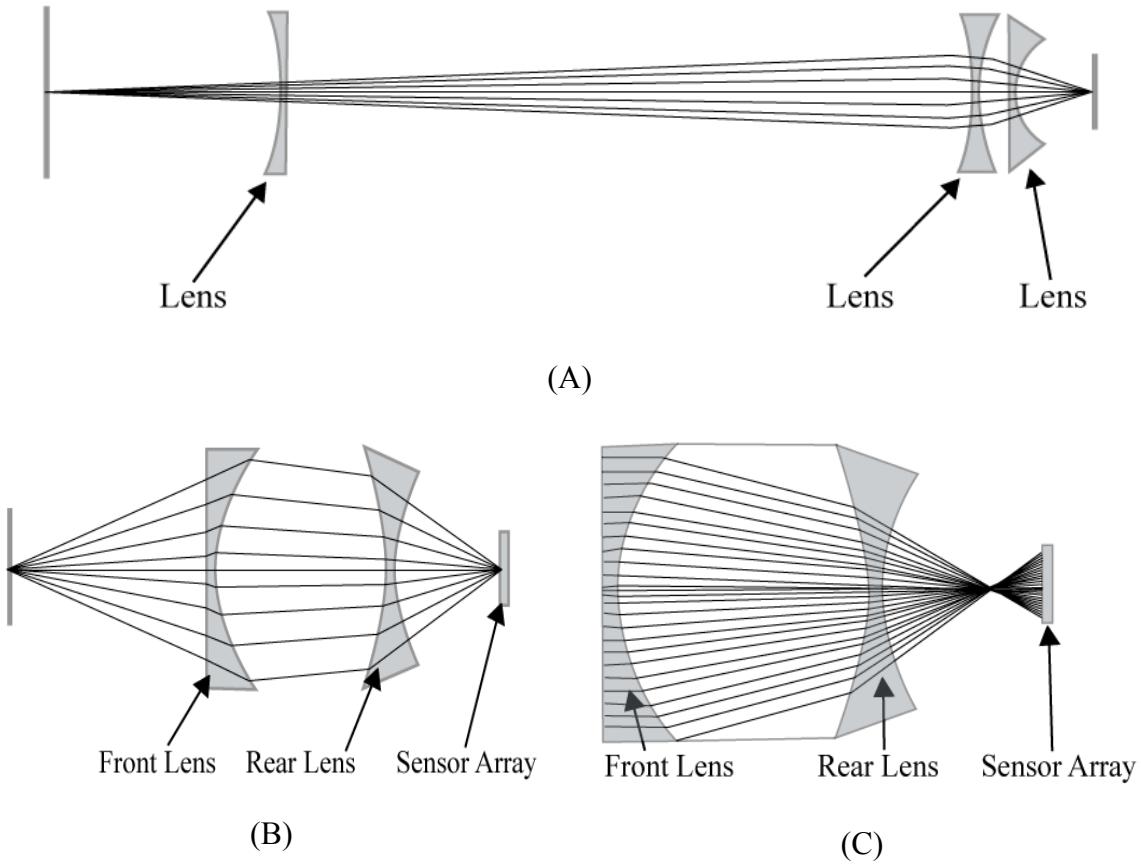

Figure 2-17. Ray tracing plots for (A) the compound acoustic lens originally designed for I-100 array and (B) the newly compact design for I-400 array with reduced lens elements. (C) Plots of the compact lens system while a parallel ultrasound beam is used.

2.4.4 Concept of C-scan Ultrasound Imaging

The concept of the C-scan (projection scan) imaging system is diagramed in Figure 2-18. The transducer generates unfocused ultrasound plane waves onto the target which is placed in a water tank between the transducer and the sensor array. The ultrasound energy is attenuated and scattered inside the target while the compound acoustic lens collects the transmitted energy and focuses it onto the sensor array. The received energy which strikes the piezoelectric material is converted to an analog voltage and then digitized and processed by the video electronics for real-time display on a monitor.

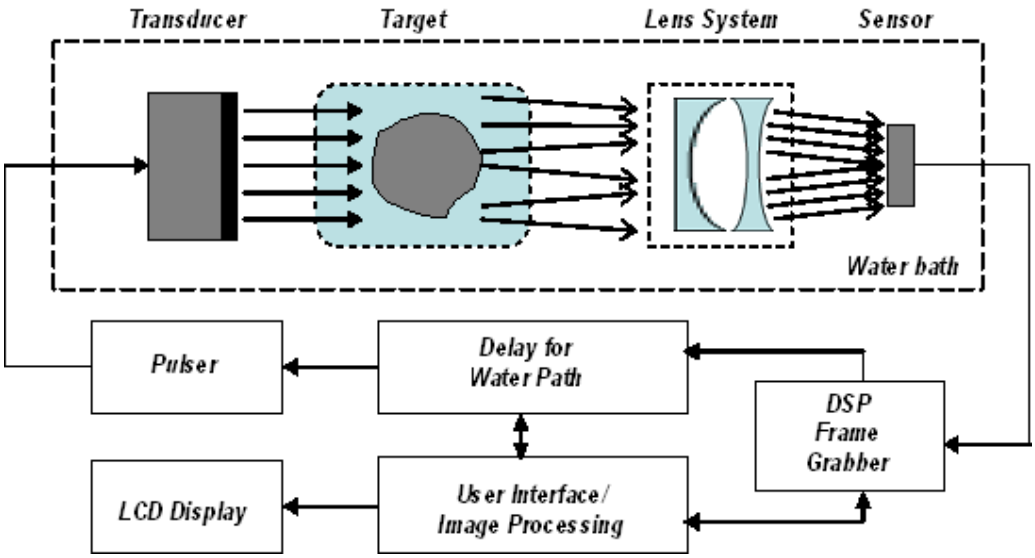

Figure 2-18. Projection ultrasound imaging system and image acquisition.

2.4.5 The First C-scan Prototype with I-100 PE-CMOS Array

To examine the potential clinical use of the I-100 sensor array in medical ultrasound imaging, a projection imaging prototype (C-scan prototype #1) was developed using the first generation PE-CMOS sensor array during 2001 to 2004. The first C-scan ultrasound imaging system consists of a 5MHz plane wave transducer, a compound acoustic lens system made of three lens elements, a detecting unit with the first generation I-100 sensor array, and a water tank sized at $50cm \times 50cm \times 25cm$ ($L \times W \times H$). A picture of the laboratory system configuration is shown in Figure 2-19.

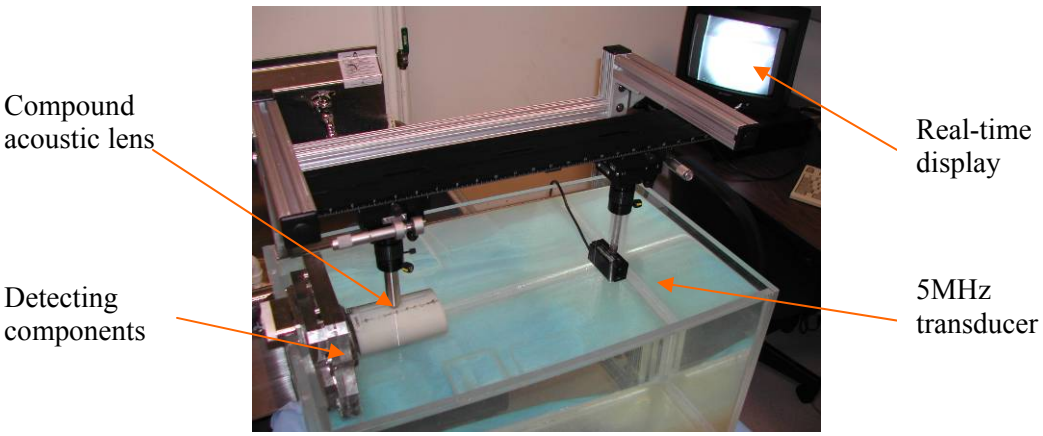

Figure 2-19. Laboratory system configuration of the C-scan prototype #1.

2.4.6 The Second C-scan Prototype with I-400 PE-CMOS Array

The second generation C-scan prototype (C-scan prototype #2) was investigated and fabricated with a compact design which included more accurate transducer-to-receiver alignment, a reduced two piece acoustic lens system, a smaller size of the water container ($20cm \times 30cm \times 20cm$, $L \times W \times H$), and a rotating base on the main frame of the prototype. The water tank, if removed from the main structure, also becomes a portable imaging device. This prototype is capable of producing 360 degree projection ultrasound images for the ultrasound CT study by integrating a micro stepping motor underneath the water container. The plane wave transducer is located at the bottom of the water tank; the detecting unit with an I-400 sensor array is directly mounted on one side of the water tank; and the imaging target is hung on the top of the bridge between the transducer and receiving unit. The design and a picture of the C-scan prototype #2 are shown in Figure 2-20 (A) and (B) respectively.

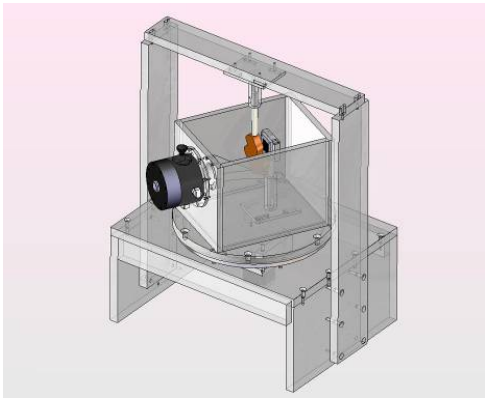

(A)

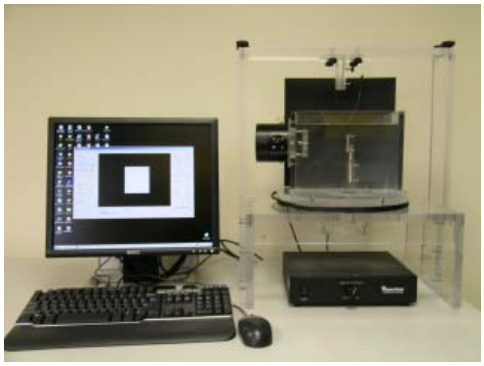

(B)

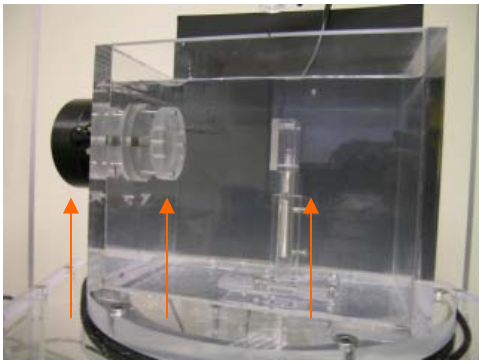

(C)

Figure 2-20. (A) The system design and (B) a picture of the completely C-scan prototype #2. (C) A closer view of the components (left to right): the detecting unit, lens system, and transducer.

2.5 Preliminary Evaluations of C-scan Prototypes

2.5.1 Uniformity

In order to evaluate the image uniformity of the C-scan prototype #1, initial tests of generating background images were completed using the I-100 sensor array. The testing process was carried out by imaging only water in the container at room temperature without any other targets and by varying the power level of the transducer. A series of 2-D images were acquired digitally and each background image represented the acoustic intensity distribution at the sensor array by a certain power level. A point detector kernel (5 pixels by 5 pixels) was employed to identify the locations of the inactive or unevenly reactive pixels in the background images by calculating the mean and variance values within the kernel. The outlier's location of the inactive pixel (black dots in the image) and the uneven reactive pixel (intensity lower or higher than average value) were cross-validated using all images generated at different power levels. A bilinear method was then applied to calculate the compensation value of those suspect locations by averaging their surrounding pixels. This measurement was consequently utilized in calibrating the ultrasound images obtained by the C-Scan imaging prototype #1. Figure 2-21 (A) through (D) demonstrates the preliminary calibration of ultrasound images taken by the c-scan prototype #1.

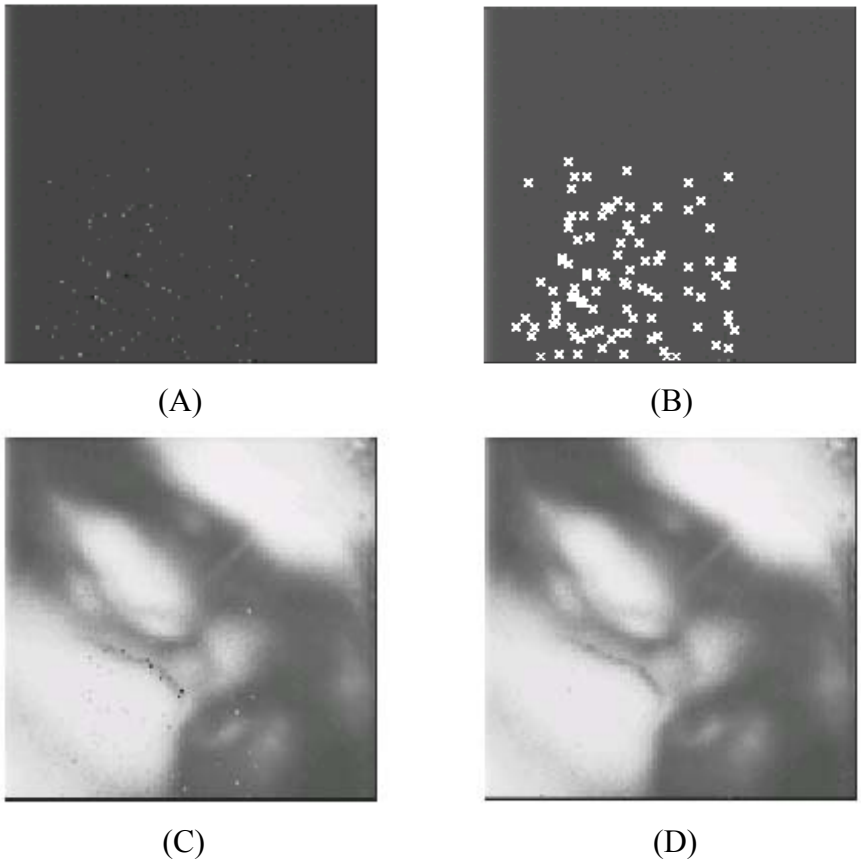

Figure 2-21. (A) Inactive pixels. (B) Marked inactive pixels. (C) Original image. (D) Processed image.

With the improved piezoelectric coating technology, the ultrasound images generated by the C-scan prototype #2 did not have many inactive pixels in the principal viewing area. As a result, the point detecting kernel and the bilinear average method were integrated to be a part of the pre-processing calibration function of the I-400 sensor array in C-scan prototype #2 to achieve uniform display.

2.5.2 Spatial Resolution

The ability of the projection system to resolve separate objects was also tested. A custom-made line-bar phantom was manufactured by Computerized Imaging Reference Systems, Inc., (CIRS, in Norfolk, VA), with seven 250-micron stainless steel wires

arranged in a fan pattern. This resolution phantom was filled by Zerdine™, a solid, elastic, water-based polymer with known acoustic speed and attenuation coefficient similar to soft tissue. Figure 2-22 (A) and (B) illustrates the schematic design of this phantom.

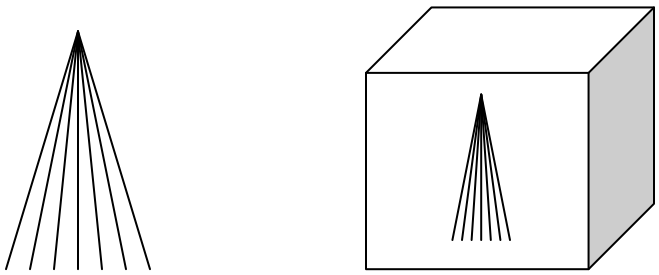

(A) (B)

Figure 2-22. (A) Fan shape pattern with seven wires at 250 microns. (B) Diagram of the spatial resolution phantom. Wires were embedded in a background of Zerdine™.

Ultrasound images of the phantom were obtained by C-scan prototype #1 and #2 separately at the frequency of 5MHz. The horizontal intensity plots of two marked lines obtained by the two sensor arrays, which represented ~350 microns and ~500 microns spacing between each wire, are shown in Figure 2-23. The intensity distributions across the fan pattern were further analyzed and the results indicated that the spatial resolution of prototype #2 was higher than that of prototype #1 and C-scan images acquired by the prototype #2 appeared to have better contrast with less noise.

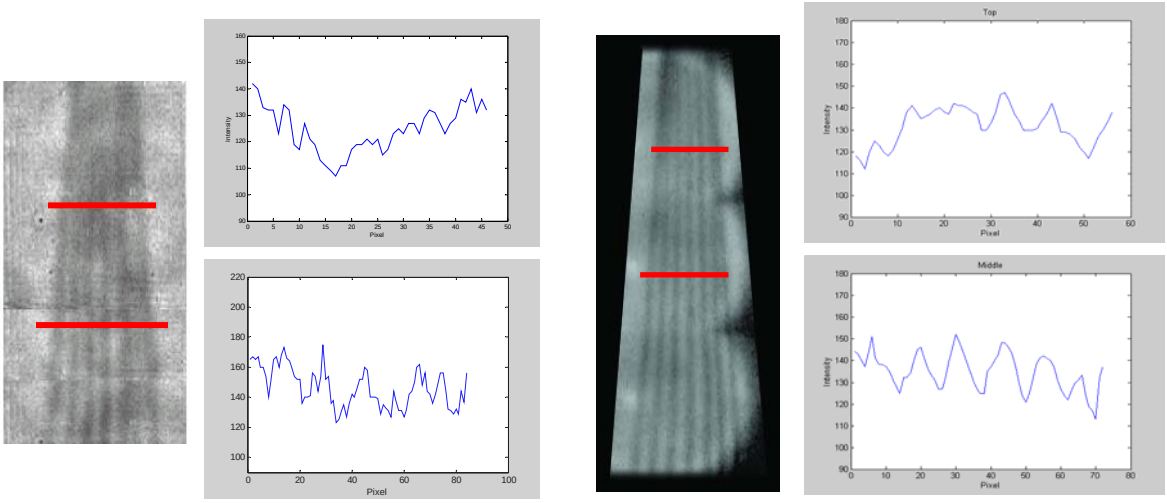

(A) (B)

Figure 2-23. Ultrasound images of the phantom and the horizontal intensity plots of the marked lines, which represented ~350 microns and ~500 microns wire-to-wire spacing, obtained by (A) prototype #1 and (B) prototype #2 separately.

2.5.3 Dynamic Range

CIRS constructed a special step-wedge phantom which was utilized in evaluating the dynamic range of the sensor arrays in the C-scan prototypes. The phantom was comprised of thirteen rectangular blocks at different length as shown in Figure 2-24. The wedge phantom was manufactured from a material with ultrasound attenuation at 0.66 $dB \cdot cm^{-1} \cdot MHz^{-1}$, and edge steps were embedded in a background material with ultrasound attenuation at 0.06 $dB \cdot cm^{-1} \cdot MHz^{-1}$.

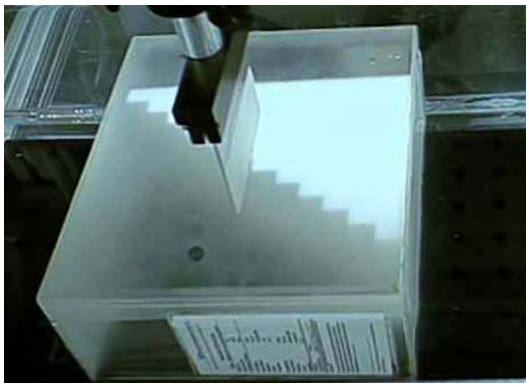

Figure 2-24. Dynamic range phantom.

In order to evaluate the dynamic range of the imaging system, a total of fourteen images were acquired, of which thirteen images were from the dynamic range phantom blocks and one was obtained without the phantom. Each block of the step-wedge phantom was placed at the focal plane position where the lens was focused in the imaging system. All fourteen images were captured by both the C-scan prototypes using I-100 and I-400 sensor arrays. Their respective mean and standard deviation values were measured. In order to examine the precise attenuation effect of the measured intensity, the total attenuation along the imaging path, including the water, the phantom, and the acoustic lens, was carefully calculated. The attenuation was then calculated as follows:

$$\alpha = 10 \cdot \log_{10}(\frac{I_0 - I_b}{I - I_b}) \qquad (2.11)$$

where I was the measured intensity, I_0 was the full intensity emitted from the transducer, and I_b was the measured intensity without any ultrasound signal (i.e. dark current in the sensor array). The water in the tank had an attenuation coefficient of 0.0022 $dB \cdot cm^{-1} \cdot MHz^{-1}$ at 20ºC. The acoustic lens system had a 0.0234 $dB \cdot cm^{-1} \cdot MHz^{-1}$ attenuation coefficient. The C-scan ultrasound images of each detailed attenuation step are shown in Figure 2-25 and their step intensity distributions are plotted in Figure 2-26.

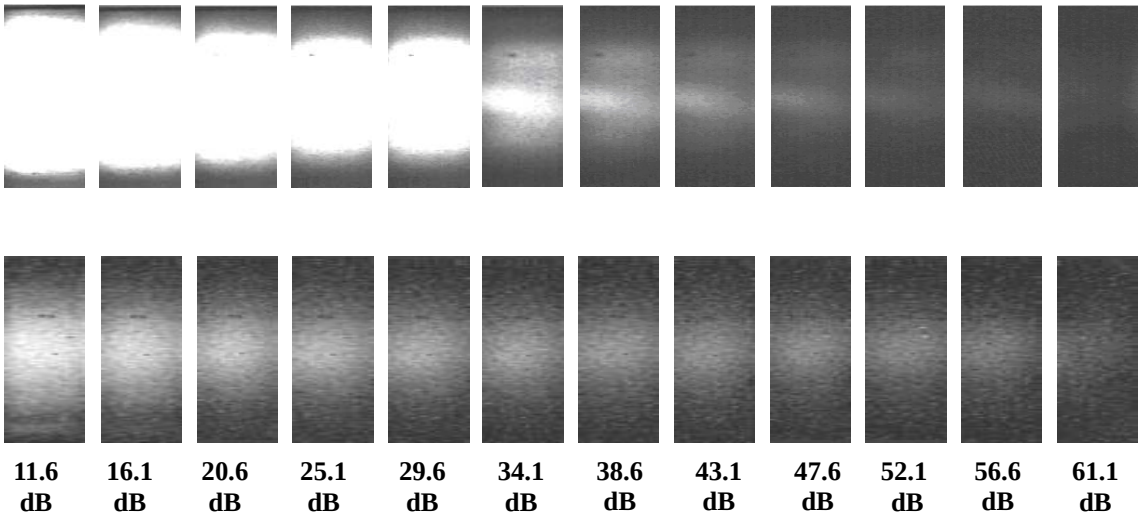

Figure 2-25. C-scan images of each attenuation step. Note that the images of last two steps were not displayed because their attenuations were too high.

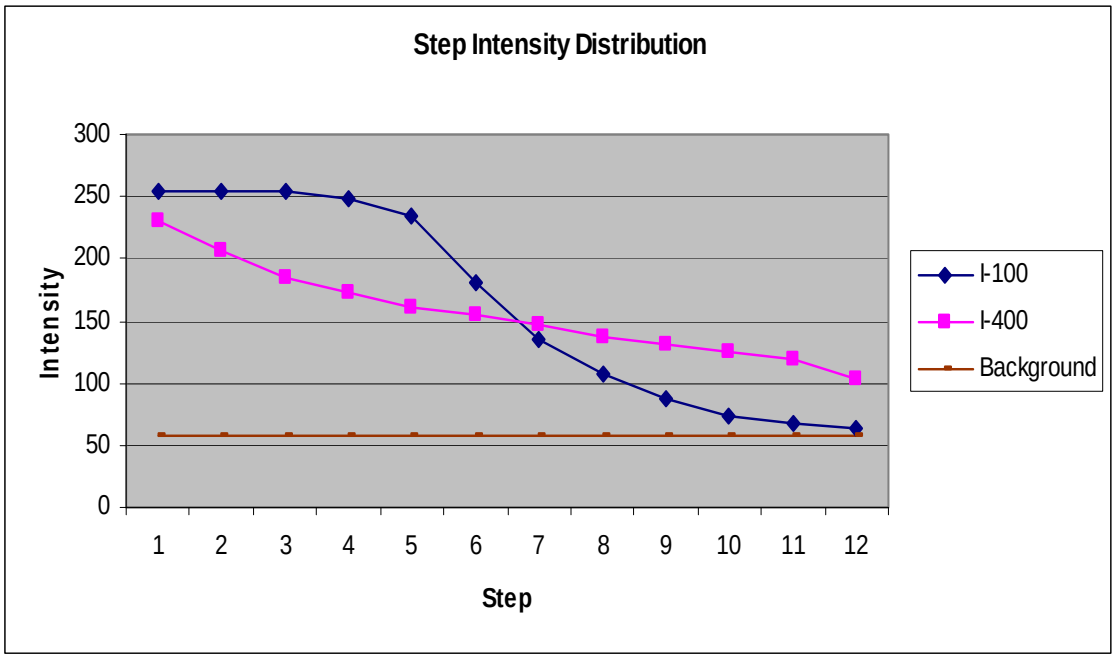

Figure 2-26. Step intensity distributions of C-scan prototypes using I-100 and I-400 sensor arrays.

2.5.4 Modulation Transfer Function

The Modulation Transfer Function (MTF) is a measurement of the imaging system's ability to transfer contrast from the target to the imaging plane at a specific resolution. The MTF reveals how well the varying brightness at a given frequency will be reproduced by an imaging system. It is also called Signal Frequency Response (SFR). This concept is derived from standard conventions that relate the degree of modulation of an output signal to a function of the signal frequency.

The modulation for any signal is defined by the two variables of that signal, the maximum intensity value $I_{\max}$ and minimum intensity value $I_{\min}$. Modulation is formulated as the quotient of their differences to their sums[41, 42], as follows:

$$Modulation = \frac{I_{\max} - I_{\min}}{I_{\max} + I_{\min}} \qquad (2.12)$$

And the MTF is calculated using:

$$MTF = \frac{M_o}{M_i} \qquad (2.13)$$

where M_i is the input modulation and M_o is the output modulation. These modulation quantities can be determined after imaging. The ratio of M_o / M_i is then plotted for each known frequency to form a MTF curve. The MTF curve carries essential information regarding a number of properties including spatial frequency and contrast. Based on an imaging system's MTF curve, the minimal structure or maximum spatial frequency which can be successfully imaged is determined.

The MTF curve can be obtained by applying the Fourier Transform to the point spread function (PSF) and the PSF can be obtained by applying the derivative of the edge spread function (ESF). The relationship of ESF, PSF and MTF is[43]:

$$PSF(x) = \frac{d(ESF)}{dx} \qquad (2.14)$$

$$MTF(u) = FT\{PSF(x)\} \qquad (2.15)$$

To determine the ESF using a two-dimensional sensor array, a thick material with high attenuation was used to block a uniform phantom. The edge ultrasound images of C-scan prototype #1 and #2 were then obtained, as shown in Figure 2-27 (A) and (B) respectively. The grey region represents the attenuated ultrasound signals passing through the phantom, and the dark region represents the image that is blocked by the thick object. The intensity profile along the horizontal direction of an edge ultrasound image was plotted as an ESF. The PSF curves were then calculated by Equation 2.14 and plotted in Figure 2-27 (C) and (D) illustrates the MTP curves for I-100 and I-400 sensor arrays.

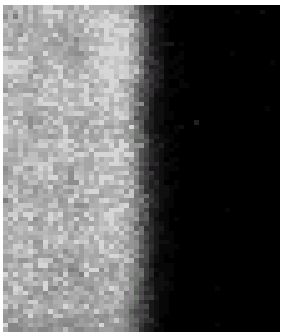

(A) Edge image taken by I-100

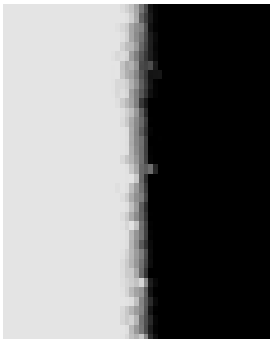

(B) Edge image taken by I-400

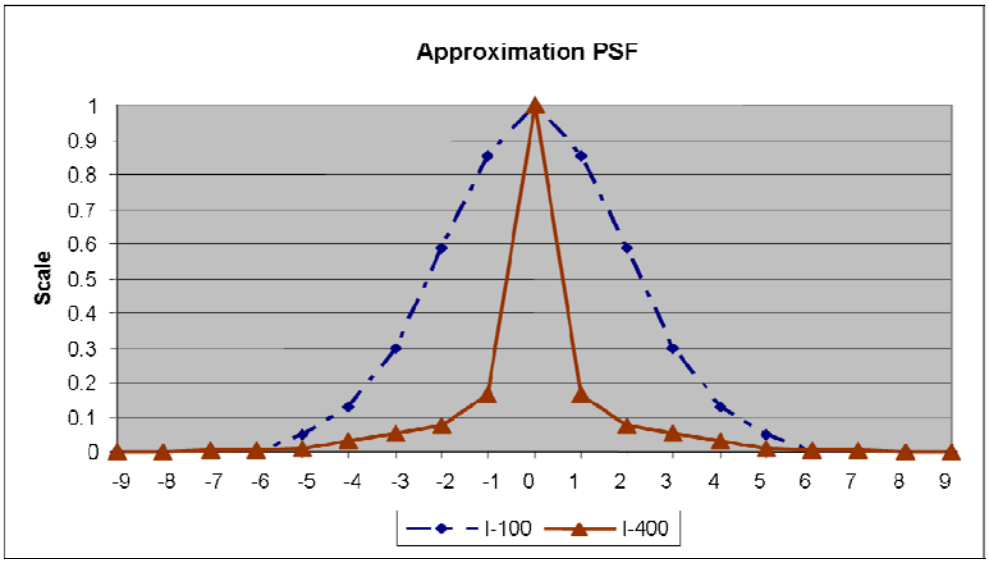

(C) The approximations of PSF curves.

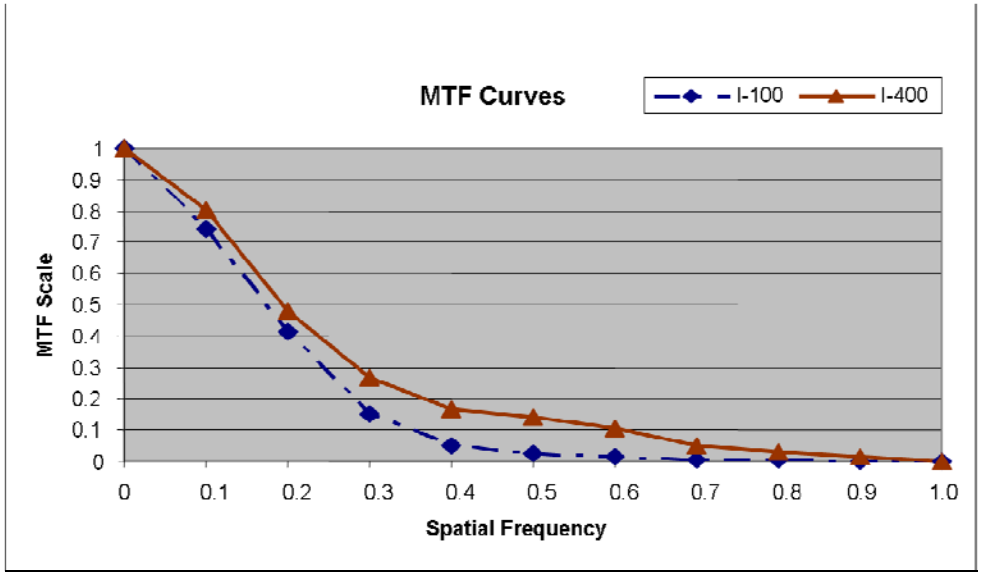

(D) The MTF curves.

Figure 2-27. (A)(B) Edge ultrasound images taken by I-100 and I-400 sensor arrays respectively. (C) Plots of the normalized PSF and (D) the MTF curves of two sensor arrays.

2.6 Breast Phantom Study and *in vitro* Study

To evaluate if the C-scan prototypes hold promise for use in medical and clinical environments, ultrasound images of breast phantoms and real tissue samples were obtained. C-scan prototypes was used to determine if it can detect clinically significant features such as spiculations of masses, cysts and tumor mimicking tissues, clustered microcalcifications, and fibro structure.

2.6.1 Cyst and Tumor Phantom

A breast phantom, which was custom made by CIRS and consisted of a set of spheres in a background material (Zerdine™), was employed in the phantom studies to simulate breast tissue. The ultrasound attenuation coefficient of the background material was 0.22 $dB \cdot cm^{-1} \cdot MHz^{-1}$. The sphere set was comprised of four spheres with different ultrasound attenuation coefficients: 0.06, 0.15, 0.5, and 0.8 $dB \cdot cm^{-1} \cdot MHz^{-1}$. The spheres in the phantom measured ~500 microns (see Figure 2-28). The spheres with attenuations of 0.06 and 0.15 $dB \cdot cm^{-1} \cdot MHz^{-1}$ mimicked cysts while the spheres with attenuation of 0.5 and 0.8 $dB \cdot cm^{-1} \cdot MHz^{-1}$ mimicked tumors. Sample ultrasound images of the phantom were captured using C-scan prototype #1 with I-100 array and #2 with I-400 array at a frequency of 5MHz as exhibited in Figure 2-29. Equipped with the newly designed acoustic lens system, the sphere images were taken individually for the I-400 array.

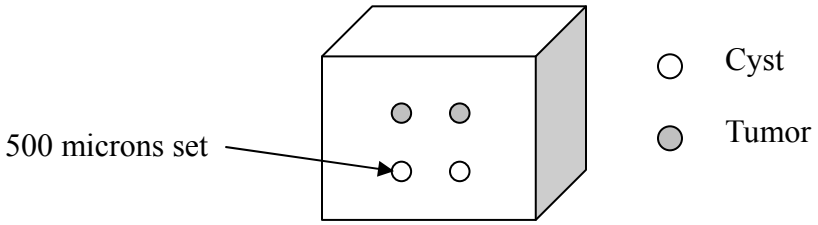

Figure 2-28. Design of the cysts and tumor phantom.

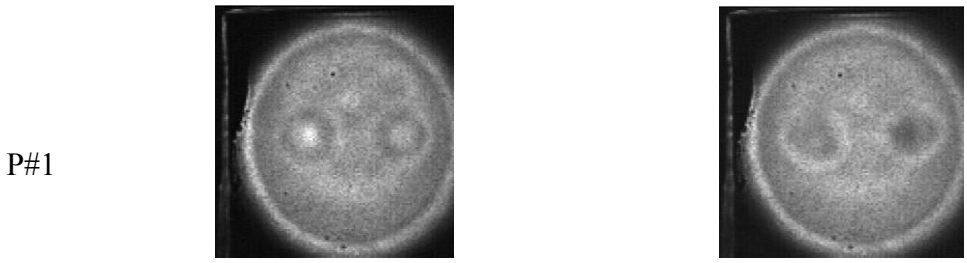

(A) Image of two simulated cysts (B) Images of two simulated tumors

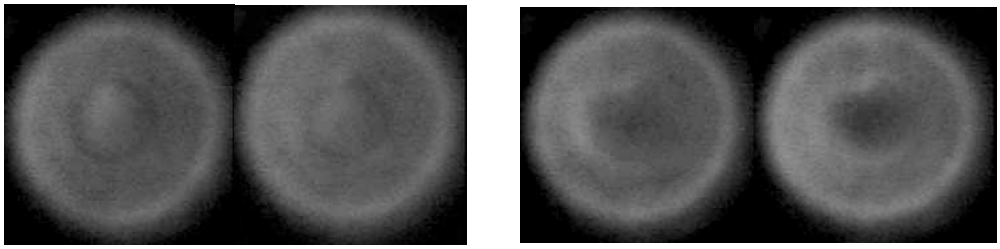

(C) Image of two simulated cysts (D) Images of two simulated tumors

Figure 2-29. Ultrasound images of 5mm cysts and tumors obtained by I-100 and I-400 sensor arrays. (A)(C) Cysts mimicking spheres with 0.06 $dB \cdot cm^{-1} \cdot MHz^{-1}$ on the left and 0.15 $dB \cdot cm^{-1} \cdot MHz^{-1}$ on the right. (B)(D) Tumor mimicking spheres with 0.5 $dB \cdot cm^{-1} \cdot MHz^{-1}$ on the left and 0.8 $dB \cdot cm^{-1} \cdot MHz^{-1}$ on the right.

In addition, a CIRS Model 52 Breast Phantom which contained large cysts and masses (5-10mm) and several destructed structures within it, was used to evaluate the detectbility of the I-400 sensor array in C-scan prototype #2 using a 7.5MHz transducer. The phantom had been used by residents for training for sometime. Figure 2-30 displays several simulated mass and cyst images of the breast phantom including some destructed structures which are clearly observable in these images.

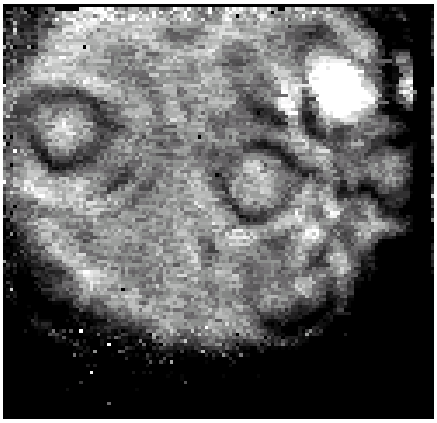

Several cysts

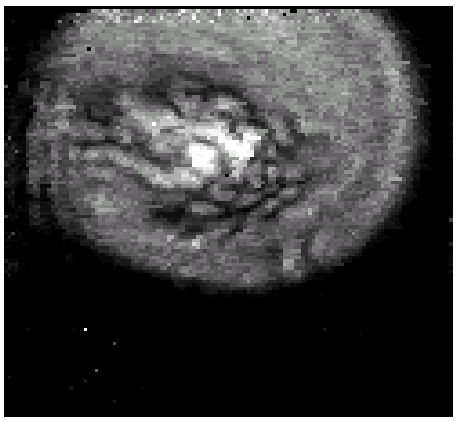

Destructed structure

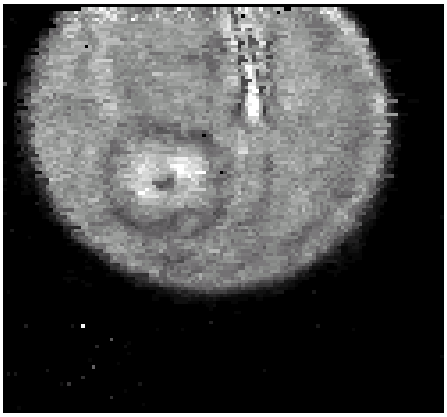

Cyst and structure

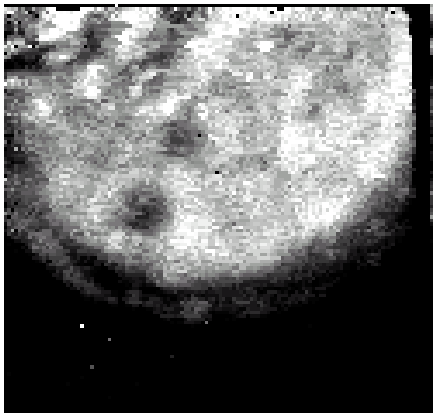

Two masses

Figure 2-30. A series of C-scan images taken from a CIRS Model 52 breast phantom by the C-scan prototype#2 operating at 7.5 MHz. The destructed structures in the breast phantom are also observable.

2.6.2 Microcalcification Phantom

To further evaluate the detectability of C-scan prototypes, a microcalcification phantom with two sets of microcalcifications embedded in a base of Zerdine™ was custom made by CIRS. One set contained five elements ranging in sizes from 710 to 850 microns; the other set contained five elements ranging in sizes from 420 to 450 microns. Figure 2-31 illustrates the design of the microcalcification phantom.

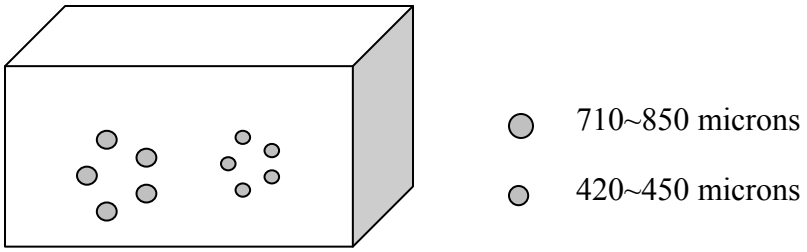

Figure 2-31. Design of the microcalcification phantom.

For the purpose of analyzing the performances of C-scan prototypes, two phantoms with different contrast settings of -3dB and -4dB were specifically produced by request. Same sizes of microcalcification spheres were embedded in both phantoms however the phantom imaged by the I-400 array had lower contrast (-3dB) between the spheres and the background material Zerdine™. C-scan images of microcalcification phantoms which were captured by prototype #1 and #2 separately using a 5MHz transducer are shown in Figure 2-32.

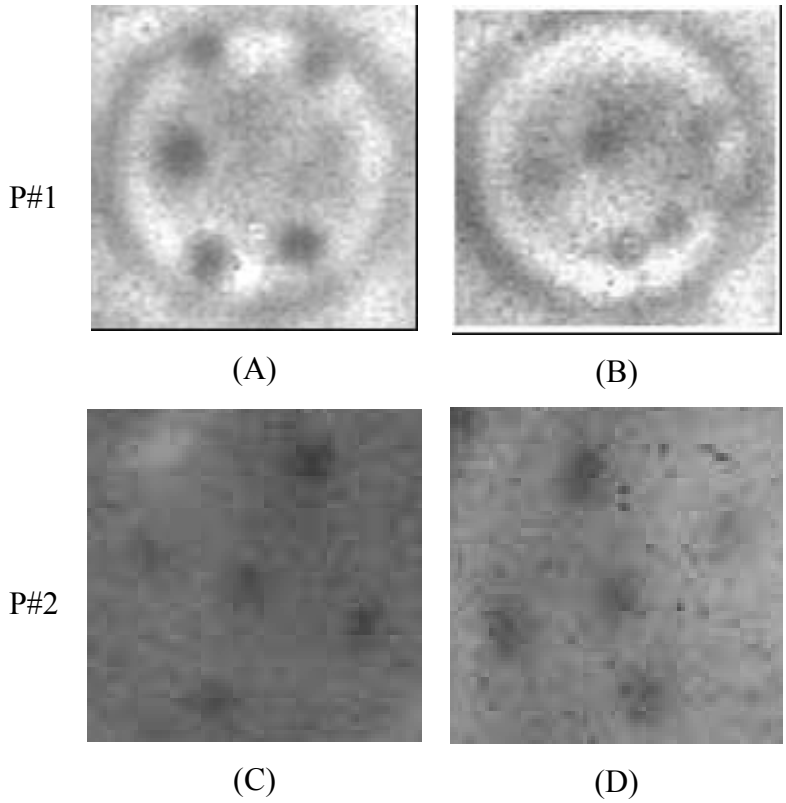

Figure 2-32. Ultrasound images of the microcalcification phantoms. (A)(C) 0.7-0.85mm clustered calcifications (B)(D) 0.42-0.45mm clustered calcifications. Note: The phantom employed in (C) and (D) had lower contrast (-3dB) between objects and background.

2.6.3 Human Objects

Ultrasound images of a human finger were acquired at ultrasound frequencies of 5 MHz using the C-Scan prototype #2 with I-400 sensor array. During the imaging process, the system maintained the same geometry setup including a fixed focus position. A human finger was placed at the focal location and ultrasound images were captured. In Figure 2-33, images (A), (B), and (C)) exhibit several finger images taken using a 5MHz transducer; (D), (E)and (F) exhibit the corresponding finger images produced by a 7.5 MHz transducer displaying more finger structure detail as compare to the images obtained with a 5MHz transducer.

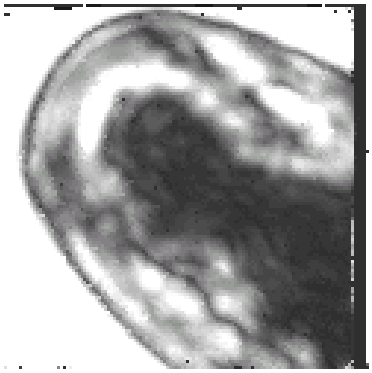

(A) Finger image.

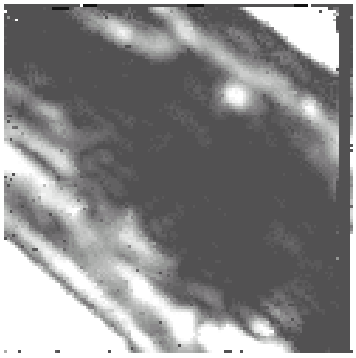

(B) 2cm below image (A).

(C) 4cm bellow image (A)

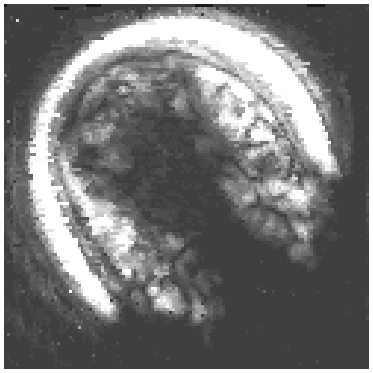

(D) Finger image.

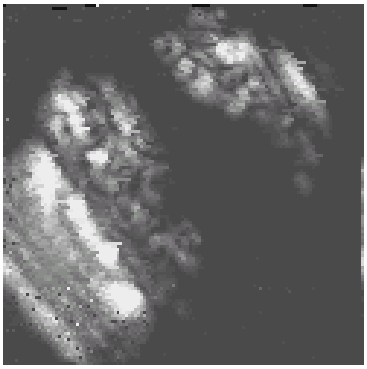

(E) 2cm below image (D).

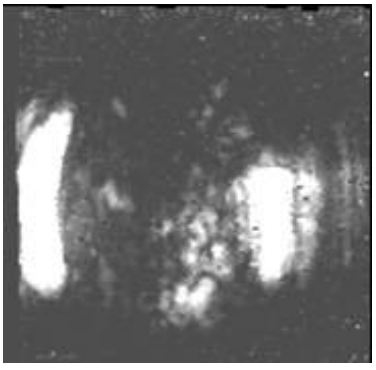

(F) 2cm below image (E).

Figure 2-33. Finger images obtained by C-scan prototype #2: (A) Finger image taken by a 5MHz transducer. (B) Area 2cm below the top of a finger by 5MHz transducer. (C) Area 4cm below the top of a finger by 5MHz transducer. (D) Finger image taken by 7.5MHz transducer. (E) Area 2cm below the top of a finger by 7.5MHz transducer. (F) Area 4cm below the top of a finger by 7.5MHz transducer.

It is apparent that the higher the ultrasound frequency, the greater the spatial resolution obtainable from soft-tissues for the reason that the shorter wavelengths in a higher frequency enables enhanced differentiation of finer structures which are closely related in the imaging target. Lower frequency images, however, provide greater depth of penetration with lower resolution than those obtained at a higher frequency.

2.7 Summary

In this Chapter, we introduced and illustrated the developments of two C-scan imaging prototypes which were equipped with the I-100 and I-400 PE-CMOS sensors. By merging knowledge gained in the advanced acoustic science with sensor technology, C-scan ultrasound prototypes has been developed to produce ultrasound images without speckle effects, which are commonly seen in conventional B-scan devices. The concept of C-scan ultrasound is similar to standard radiography devices equipped with the non-ionizing ultrasound source. Moreover, C-scan images produced by the newly developed prototypes have real-time fluoroscopic presentations and capable to record video clips at 30 frames per second.

Custom phantoms were designed and fabricated to evaluate the basic performance of C-scan prototypes. Comparative *in vitro* evaluations on characteristics of obtained C-scan images demonstrated improvements from the prototypes #1 to prototype #2 in sensitivity, dynamic range, contrast, and spatial resolution. According to the preliminary *in vivo* investigations on imaging human objects, the 4th generation I-400 sensor revealed detail structures at frequencies of 5MHz and 7.5 MHz. Depending on the properties of the imaging target, i.e. thickness or attenuation, it is possible to switch transducers in the

frequency ranged between 3KHz to 25MHz. The flexibility of choosing transducers operating at different frequencies gives the C-scan ultrasound the potential to support broader medical applications. Further investigations will be addressed in Chapters 4 and 5.

Chapter 3

Modeling Ultrasound Forward Scattering: Characteristic and Measurement

In general, human soft tissues may contain both relatively homogeneous and heterogeneous characteristics, which are often associated with a different physical parameter such as attenuation (absorption and scattering) in medical imaging. For conventional B-scan ultrasound with a linear transducer, the ultrasound scattering effect is concerned with a variation of 5-10% of the total attenuation in soft tissues[45, 46]. Therefore, scattering effects are not considered as the major influence of B-scan ultrasound image quality. Typically, B-scan system often suffers artifacts from speckles, many researchers have attempted to develop various image enhancement methods for reducing speckle and/or noise for practical or research purposes using deconvolution[47-49], neural network[50], and Bayesian statistics approach[51], etc. Typically in B-scan ultrasound, restoration methods often employ the point spread function (PSF) of the image followed by a deconvolution. It has been shown that the deconvolution method is essential to the enhancement of B-scan ultrasound image quality.

However, different from conventional ultrasound pulse-echo pathway, the geometry of the proposed C-scan (projection) ultrasound imaging system is similar to a standard radiographic system. The detected ultrasound signal is a through-transmitted intensity, which consist of the residual of the attenuated intensity along the primary propagating direction and the multidirectional scattering intensities. Therefore, the forward scattering energy component is considered to be one of the main causes of blurry artifacts in a C-scan image.

In this chapter, we introduce the mathematical reviews of scattering phenomena in single scatterer and multiple scatterers in a homogeneous medium separately. Based on Twersky's multiple scattering theory (refer to Section 3.2 and Appendix A), which states the scattering energy can be largely modeled with the assumption of scatterers randomly distributed in a homogeneous medium, we have developed an effective method to quantify the detected C-scan ultrasound signal attributed to the primary ultrasound beams and the associated scattering effects.

3.1 Mathematical Review of Scattering

3.1.1 Single Scatterer in Homogeneous Medium

With the equilibrium properties of density ρ_0 and compressibility κ_0 (see Figure 3-1), the evolution of acoustic pressure p at the traveling speed u for acoustic waves spreading through a homogeneous medium is determined by the following acoustic wave equation[52, 53]:

$$\nabla^2 p - \frac{1}{u^2}\frac{\partial^2 p}{\partial t^2} = 0 \qquad (3.1)$$

where $u^2 = (\rho_0 \kappa_0)^{-1}$ and $\nabla^2 = \frac{\partial}{\partial x^2} + \frac{\partial}{\partial y^2} + \frac{\partial}{\partial z^2}$,which is the three-dimensional (3-D) Laplace operator.

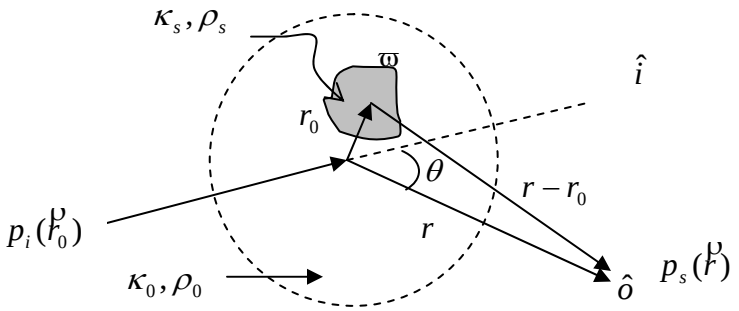

Figure 3-1. The scattering geometry for a single scatterer in a homogeneous medium.

The inhomogeneous perturbation of the scattering is presented in the following equation when a scatterer is embedded within a homogeneous medium,

$$\nabla \cdot (\frac{1}{\rho_s} \nabla p) - \kappa_s \frac{\partial^2 p}{\partial t^2} = 0 \qquad (3.2)$$

where the quantities ρ_s and κ_s are the density and compressibility of the scattering source, respectively. If there exists a change in the boundary or a variation in density, the $\frac{1}{\rho_s}$ as indicated above is inside the divergence operation.

Furthermore, by recasting Equation 3.2 as a perturbation to the homogeneous wave equation 3.1, the scattered pressure field is computed as follows:

$$\nabla^2 p - \frac{1}{u^2} \frac{\partial^2 p}{\partial t^2} = \gamma_\kappa(r) \frac{1}{u^2} \frac{\partial^2 p}{\partial t^2} + \nabla \cdot (\gamma_\rho(r) \nabla p) \qquad (3.3)$$

where $\gamma_\kappa(r) = \frac{\kappa_s(r) - \kappa_0}{\kappa_0}$ and $\gamma_\rho(r) = \frac{\rho_s(r) - \rho_0}{\rho_s(r)}$.

In this instance, $\gamma_\kappa(r) \frac{1}{u^2} \frac{\partial^2 p}{\partial t^2}$ represents the scattering effects of variations in compressibility while $\nabla \cdot (\gamma_\rho(r) \nabla p)$ represents the effects of variations in medium density.

3.1.2 The Helmholtz Equation and Green's Function Approach

In order to obtain a time-independent form of the partial differential wave equation, the Equation 3.1, at the particular frequency of $f = \frac{\omega}{2\pi}$, the Helmholtz Equation[54, 55] , written as a formation of $p(r,t) = p_{\omega}(r)\exp(-i\omega t)$ with respect to *r* and *t*, may be applied.

The inhomogeneous Helmholtz equation is presented as follows:

$$\nabla^2 p_{\omega} + k^2 p_{\omega} = -f(r) \qquad (3.4)$$

where $k = \frac{\omega^2}{u^2}$ is the wave number, $f(r)$ is the scattering perturbation and

$$f(r) = k^2 \gamma_{\kappa}(r) p_{\omega}(r) - \nabla \cdot (\gamma_{\rho}(r) \nabla p_{\omega}(r)) \qquad (3.5)$$

As a solution to the inhomogeneous differential equation which satisfies equation 3.4, a well known Green's function resolves the following[55, 56]:

$$\nabla^2 G_{\omega}(r \mid r_0) + k^2 G_{\omega}(r \mid r_0) = -\delta(r - r_0) \qquad (3.6)$$

In this instance, the free space Green's function $G(r \mid r_0)$ depicts the observed pressure field at the detector's location *r* stemming from a point source of scattering located at r_0. For a point source at r_0 which emits out into an unbounded medium, $\delta(r - r_0)$ is the Dirac delta function for three dimensions in regards to the observer's coordinate system.

Spherical pressure waves are created by simple harmonic scattering sources as follows:

$$G_\omega(r \mid r_0) = \frac{1}{4\pi \mid r - r_0 \mid} e^{ik|r-r_0|} \qquad (3.7)$$

Equations 3.4 and 3.6 are consolidated as follows to obtain the integral expression for p_ω:

$$G_\omega(r \mid r_0)\nabla^2 p_\omega(r_0) - p_\omega(r_0)\nabla^2 G_\omega(r \mid r_0) = p_\omega(r_0)\delta(r - r_0) - f_\omega(r_0)G_\omega(r \mid r_0) \qquad (3.8)$$

where r and r_0 in G_ω and δ are interchangeable. If integrating over the volume elements dv_0 located at r_0 of a volume V containing the scattering sources, the following solution is reached:

$$p_\omega(r) = \int_V [G_\omega(r \mid r_0)\nabla^2 p_\omega(r_0) - p_\omega(r_0)\nabla^2 G_\omega(r \mid r_0)]dv_0 + \int_V f_\omega(r_0)G_\omega(r \mid r_0)dv_0 \qquad (3.9)$$

When applying the Gauss's theorem[57, 58] which states $\int_V \nabla \cdot F dv = \int_S F \cdot \hat{n} ds$, the first integral in Equation 3.8 may be written as an integral over the surface S enclosing the scattering volume. Alternatively, since

$$G\nabla^2 p - p\nabla^2 G = \nabla \cdot (G\nabla p - p\nabla G) \qquad (3.10)$$

then

$$p_\omega(r) = \int_S [G_\omega(r \mid r_0)\nabla p_\omega(r_0) - p_\omega(r_0)\nabla G_\omega(r \mid r_0)] \cdot \hat{n} ds + \int_V f_\omega(r_0)G_\omega(r \mid r_0)dv_0 \qquad (3.11)$$

where $\hat{n}$ is the unit vector normal to the surface pointing away from the scattering volume.

Based on the assumption that it is a continuous medium without boundary, the surface integral can be simplified. The scattering contribution of the surface integral becomes insignificant when the radius of the continuous medium approaches infinity while the incident pressure field p_i remains constant and, by Huygen's principle [23],

integrates to p_i for any observation point r within the volume bounded by the surface.

Consequently, Equation 3.11 is re-written as follows:

$$p_\omega(r) = p_i(r) + \int_V f_\omega(r_0) G_\omega(r \mid r_0) dv_0$$

$$= p_i(r) + \int_v [k^2 \gamma_\kappa(r_0) p_\omega(r_0) - \nabla_0 \cdot (\gamma_\rho(r_0) \nabla_0 p_\omega(r_0))] G_\omega(r \mid r_0) dv_0 \qquad (3.12)$$

The scattering filed $p_s(r)$ is presented in the second term in Equation 3.12. The total pressure field observed is the sum of the incident and scattered fields.

When applying the product rule for differentiation to Equation 3.12 and by expanding the second term in the integral expression for p_s using the product rule for differentiation and find that

$$\int_v G_\omega \nabla_0 \cdot [\gamma_\rho \nabla_0 p_\omega] dv_0 = \int_v \nabla_0 \cdot [G_\omega \gamma_\rho \nabla_0 p_\omega] dv_0 - \int_V \gamma_\rho \nabla_0 p_\omega \cdot \nabla_0 G_\omega dv_0 \qquad (3.13)$$

In this instance, a surface integral over the component of the integrand normal to the surface replaces the first integral on the right of equation 3.13 as a result of applying the Gauss's theorem. As the surface is outside the scattering inhomogeneities, $\gamma_\rho = 0$, and this integral is also zero, substituting Equation 3.13 into Equation 3.12 results in the following expression for the scattered pressure:

$$p_s(r) = \int_V [k^2 \gamma_\kappa(r_0) p_\omega(r_0) G_\omega(r \mid r_0) + \gamma_\rho(r_0) \nabla_0 p_\omega(r_0) \cdot \nabla_0 G_\omega(r \mid r_0)] dv_0 \qquad (3.14)$$

If, when compared to the size of the volume occupied by the scatters (e.g., $r >> r_0$ as illustrated in Figure 3-1), the observation distance is large, the Green's function in Equation 3.14 and its gradient are approximated by the following expressions:

$$G_\omega(r \mid r_0) \approx \frac{1}{4\pi r} e^{ikr} e^{-iK_s r_0} \tag{3.15}$$

$$\nabla_0 G_\omega(r \mid r_0) \approx -ik^2 \frac{\hat{o}}{k} G_\omega(r \mid r_0) \tag{3.16}$$

The scattering pressure field in equation 3.14 is consequently re-written as follows:

$$p_s(\vec{r}) = \frac{k^2 e^{ikr}}{4\pi r} \int_V [\gamma_\kappa(\vec{r}_0) p_\omega(\vec{r}_0) - i\gamma_\rho(\vec{r}_0)(\frac{\hat{o}}{k} \cdot \nabla' p_\omega(\vec{r}_0)] \exp(-ik_s \hat{o} \cdot \vec{r}_0) dv_0 \tag{3.17}$$

where $k^2 = \frac{\omega^2}{c^2} = \omega^2 \kappa_0 \rho_0$, and $k_s = k\hat{o}$ is the wave number vector in the direction of the detector. In addition, the scattered wave that travels to the detector is spherical wave, $\frac{e^{ikr}}{r}$.

3.1.3 Incident Plane Waves and Born Approximation

As presented in Equation 3.17, the total pressure must be determined prior to the scattered field. Initially the incident pressure is assumed to be a plane wave with pressure file, P, and as a result, the incident pressure field is resolved by $p_i(r) = Pe^{ikr}$ and $\nabla p_i = ik_i p_i$, where $k_i = k\hat{i}$ is the wave number vector in the direction of propagation of the incident field. Subsequently, it is assumed that the scattered wave amplitude is much smaller than the incident pressure, $p_s(\vec{r}_0) << p_i$ (Born approximation), therefore the total pressure field p_ω can be replaced by the field incident pressure, p_i.

By combing the incident plane assumption and the Born approximation with Equation 3.17, it can be concluded that

$$p_s(\vec{r}) = \frac{k^2 e^{ikr}}{4\pi r}\int_V [\gamma_\kappa(\vec{r}_0)\, p(\vec{r}_0) - i\gamma_\rho(\vec{r}_0)(\frac{\hat{o}}{k}\cdot\nabla' p(\vec{r}_0)]\exp(-ik_s\hat{o}\cdot\vec{r}_0)dv_0$$

$$\approx \frac{p_i k^2 e^{ikr}}{4\pi r}\int_V [\gamma_\kappa(\vec{r}_0) + \gamma_\rho(\vec{r}_0)(\hat{i}\cdot\hat{o})]\exp(-iK\cdot\vec{r}_0)dv_0$$

$$= \frac{p_i k^2 e^{ikr}}{4\pi r}\int_V [\gamma_\kappa(\vec{r}_0) + \gamma_\rho(\vec{r}_0)\cos\Theta]\exp(-iK\cdot\vec{r}_0)dv_0 \qquad (3.18)$$

where K is the scattering vector of magnitude,

$$K = k_s - k_i = k(\hat{o} - \hat{i}) = k[|\hat{o}|^2 + |\hat{i}|^2 - 2(\hat{i}\cdot\hat{o})]^{\frac{1}{2}} = 2k(\frac{1-\cos\Theta}{2})^{\frac{1}{2}} = 2k\sin(\frac{\Theta}{2}) \qquad (3.19)$$

and Θ is the scattering angle determined by the direction of the incident field and the observer in the coordinate system illustrated by Figure 3-1. Additionally, it should be noted that $\cos\Theta = (\hat{i}\cdot\hat{o})$.

Equation 3.18 describes the scattered pressure field which results from the interaction between plane waves and a small well-defined region of scattering inhomogeneities positioned inside an unbound medium. The scattered pressure field is a function of the distance r, compressibility factor γ_κ and the density factor γ_ρ when the incident pressure field and the angle between the observer and incident wave are both identified. In this case, if the angle Θ between the incident plane waves and the detector is zero degree (i.e. transmission), the scattering pressure is resolved as follows:

$$p_s(r) = \frac{p_i k^2 e^{ikr}}{4\pi r}\int_V (\gamma_\kappa + \gamma_\rho)dv_0 \qquad (3.20)$$

3.2 Twersky's Multiple Scattering Model

Historically, there have been extensive studies conducted on the subject of multiple scattering of waves. Early researchers, for instance Ryde[59], Foldy[60], Lax[61], Twersky[62], Ishimaru[63, 64] and Wang[65], have developed several general approaches to the challenge of resolving wave propagation in randomly distributed particles. Amongst the researchers, it was Twersky who expanded the multiple scattering processes based on consistent sets of integral equations to describe the total intensity outside a slab of object containing a large number of random particles, which are not necessary to be identical in shape and size, with a normally incident plane wave. The detail of mathematical derivations is described in Appendix A.

Twersky provided the following underlying solution which computes the total average intensity when a plane wave is incident upon a slab of object containing a large number of random scatters (see Figure 3-2):

$$T = \exp(-\rho(\sigma_a + \sigma_s)d) + \int_{\Omega_r} d\Omega_s \sec\theta \left|p_s\right|^2 \times \frac{\exp(-\rho\sigma_a d) - \exp(-\rho(\sigma_a + \sigma_s)d\sec\theta)}{(\sigma_a + \sigma_s)\sec\theta - \sigma_a} \tag{3.29}$$

where d is the thickness of the object; ρ is the density of the scatter distribution (number per unit volume); σ_a the absorption cross section; σ_s the scattering cross section respectively; θ the angle between the direction of the incident plane wave and the scattering direction; Ω_s the effective scattering angle and Ω_r is the solid angle of the receiver; and $\left|p_s\right|^2$ the unit scatter amplitude of a single scatterer (refer to Equation 3.17).

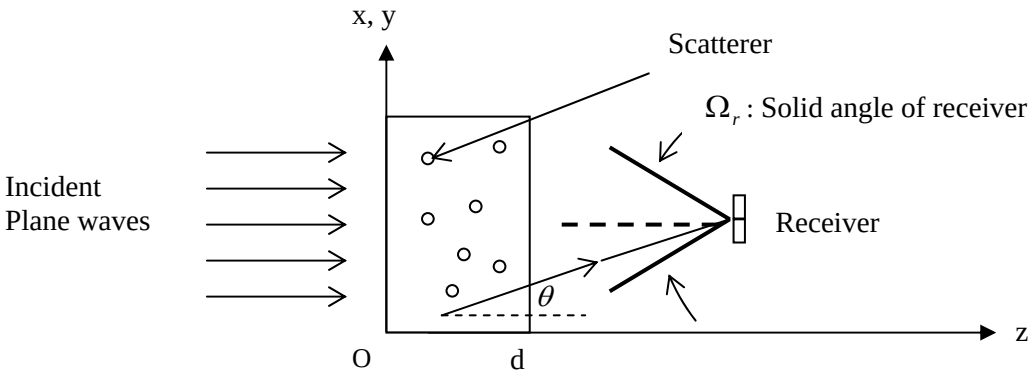

Figure 3-2. Plane waves being incident upon a slab of object with thickness d.

In Twersky's solution of Equation 3.29, the first term $\exp(-\rho(\sigma_a+\sigma_s)d)$ is equivalent to the general attenuation equation with the attenuation coefficients α which is the sum of absorption coefficient α_a (equals to $\rho\sigma_a$) and scattering coefficient α_s (equals to $\rho\sigma_s$), while $\int_{\Omega_r} d\Omega_s \sec\theta |p_s|^2 \times \frac{\exp(-\rho\sigma_a d)-\exp(-\rho(\sigma_a+\sigma_s)d\sec\theta)}{(\sigma_a+\sigma_s)\sec\theta-\sigma_a}$ represents the contribution of the multiple scattering. Consequently, *T* can be considered the sum of these two effects:

$$T = T_{att} + T_s \qquad (3.30)$$

where

$$T_{att} = \frac{I_{att}}{I_0} = \exp[-\rho(\alpha_a+\alpha_s)d] = \exp(-\alpha d) \qquad (3.31)$$

$$\text{and } T_s = \frac{I_s}{I_0} = \int_{\Omega_r} \Omega_s \sec\theta |p_s|^2 \times \frac{\exp(-\rho\sigma_a d)-\exp(-\rho(\sigma_a+\sigma_s)d\sec\theta)}{(\sigma_a+\sigma_s)\sec\theta-\sigma_a} \qquad (3.32)$$

By the definition of the total scattering cross section, $\sigma_s = \int_{4\pi} \Omega_s |p_s|^2$, an effective scattering ratio, q, is written as

$$q = \frac{\int_{\Omega_r} d\Omega_s \left| p_s \right|^2}{\int_{4\pi} d\Omega_s \left| p_s \right|^2} \tag{3.33}$$

As a result, the scattering term can be addressed as:

$$T_s = q\sigma_s \sec\theta \times \frac{\exp(-\rho\sigma_a d) - \exp(-\rho(\sigma_a + \sigma_s)d \cdot \sec\theta)}{\sec\theta \cdot \sigma_s + (\sec\theta - 1) \cdot \sigma_a} \tag{3.34}$$

The detected energy is therefore the result of ultrasound attenuation due to both absorption and scattering effects along the wave propagating direction, and multiple scattering effects elsewhere. In accordance with the solution above, the average intensity detected can be projected by its ultrasound absorption and scattering cross sections, detecting angle, object thickness and the density of the scatters (number per unit volume). However, the distribution of the average total intensity cannot be determined from the solution, and its estimation thus requires an analytical approach.

3.3 Modeling Ultrasound Forward Scattering Distribution

3.3.1 Concept of Modeling Forward Scattering in C-scan Ultrasound

Ultrasound attenuation is a major physical phenomenon which occurs when an ultrasound wave propagates through an object[54]. Typically, ultrasound attenuation includes the effects of both absorption and scattering[66]. Although in general, absorption and scattering occur simultaneously, these two phenomena are usually treated differently in global analysis. In C-scan ultrasound images, attenuation affects the overall display brightness nonetheless scattering effect is one of the principal reasons which causes the image blur. In order to obtain accurate ultrasound images from C-scan geometry using the PE-CMOS sensor array, investigation and modeling of the ultrasound scattering effect become critical.

Due to the configuration of the C-scan imaging system, the multidirectional scattering energy is partially focused by acoustic lens system in a limited detecting angle

and is contributed to the sensor array. Hence general attenuation equation (refer to Equation 3.31), cannot completely describe the intensity received in the C-scan ultrasound system. Therefore, Twersky's theory described in previous section is introduced to the C-scan geometry.

During the process when an ultrasound wave passes through an object, major physical phenomena include: transmission, reflection, absorption, refraction, scattering, diffraction, etc. Assuming that the imaging object, made by a relatively uniform material, has a normal incident plane wave, the ultrasound energy is primarily converted to different formats when absorption within the object, multidirectional scattering, the transmission and reflection occurs at the boundaries. In the C-scan imaging geometry, total detected intensity is mainly contributed by the decayed ultrasound intensity with respect to the increase of object thickness along the incident ultrasound propagation path, and the multi-directional scattering intensity revealed within a limited receiving angle (see Figure 3-3).

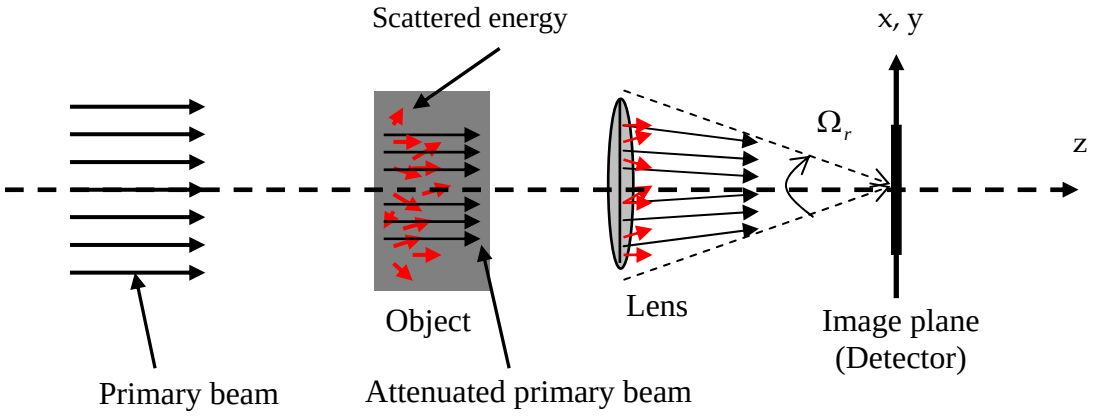

Figure 3-3. The ultrasound primary beam, attenuated energy and scattering energy in C-scan geometry.

When an ultrasound wave of intensity I_0 propagates through a uniform object with attenuation α, thickness d and travels in the z direction, the intensity relationship between the incident wave and detecting energy can be written as:

$$I_{\text{Detected}}(x,y,z) \approx I_{\text{Att\_primary}}(x,y,z) + \int_{V}\int_{\Omega_r} f_{\text{Scatter}}(x,y,z)\cdot dV \cdot d\Omega_r \qquad (3.35)$$

where I_{Detected} is the receiving intensity at the sensor, $I_{\text{Att\_primary}}$ is the residual of the attenuated primary beam whose quantity equals to $I_{\text{Att\_primary}} = I_0 \exp(\alpha d)$, f_{Scatter} is the detected scattering energy within the maximum detecting angle Ω_r, and V represents the effective volume containing multi-directional scattering energy within the object. Assuming the scattering function is circular symmetry, the second term in equation 3.35 can be considered as a convolution process, which is associated with the primary beams and scattering intensities in the detected C-scan image.

The distribution of f_{Scatter} will be further determined in the following analytical analyses.

3.4 Analytical Approach for Modeling Ultrasound Intensity Distribution

A common approach to compute the approximate point spread distribution of an imaging system is to obtain a straight-line edge image[44] (refer to Sections 2.5.4 and 3.7.2). In real practices, it is difficult to physically align an edge in straightly horizontal or vertical orientation. The inclined orientation could cause inaccuracy of the scattering evaluation. Therefore, an annular aperture has been proposed in this research for its technically feasible and easier to be implemented for modeling the forward energy distribution of the C-scan ultrasound.

3.4.1 Breast Mimicking Phantom and Annular Aperture

Under the assumption of multiple scattering, the randomness of the interaction tends to be averaged out by the large amount of scattering events; therefore, the final scattering distribution appears to be a deterministic quantity. Thus, we have developed an analytical approach that uses an annular aperture, which is attached to the surface of the

imaging target, to confine the effective areas of incident ultrasound plane waves. The study used three slabs of Zerdine™ soft-tissue mimicking phantoms, made by CIRS, with thicknesses of 12mm, 23mm and 31mm. The attenuation coefficient of Zerdine™ is 0.5 $dB \cdot cm^{-1} \cdot MHz^{-1}$ (0.116 $Neper \cdot cm^{-1} \cdot MHz^{-1}$), the density of the material is 1.03 g/cm^3, and the speed of sound in this material is 1,540 m/s.

Figure 3-4. Picture of the three soft-tissue mimicking phantoms made of Zerdine™ with thicknesses of 12mm, 23mm and 31mm.

The annular aperture employed in this investigation was made of Styrofoam, which is highly attenuating because of its contained gas. A series of annular apertures were fabricated in order to study the relationship between the size of opening gap and diffraction patterns. If the ring gap is larger, it will increase the time of computation; if smaller, the diffraction effect will rise and cause inaccurate estimation. The selected annular aperture has an inner radius of 7.1mm, outer radius of 8.6mm and the width of the ring opening gap, which allows ultrasound energy to pass, is 1.5mm (approximately five times of wavelength of 5MHz ultrasound in water). The decision was made to have better balance between the computational time and the accurate estimation. Pictures of the annular apertures and sample C-scan images obtained without phantom (water only) are illustrated in Figure 3-5.

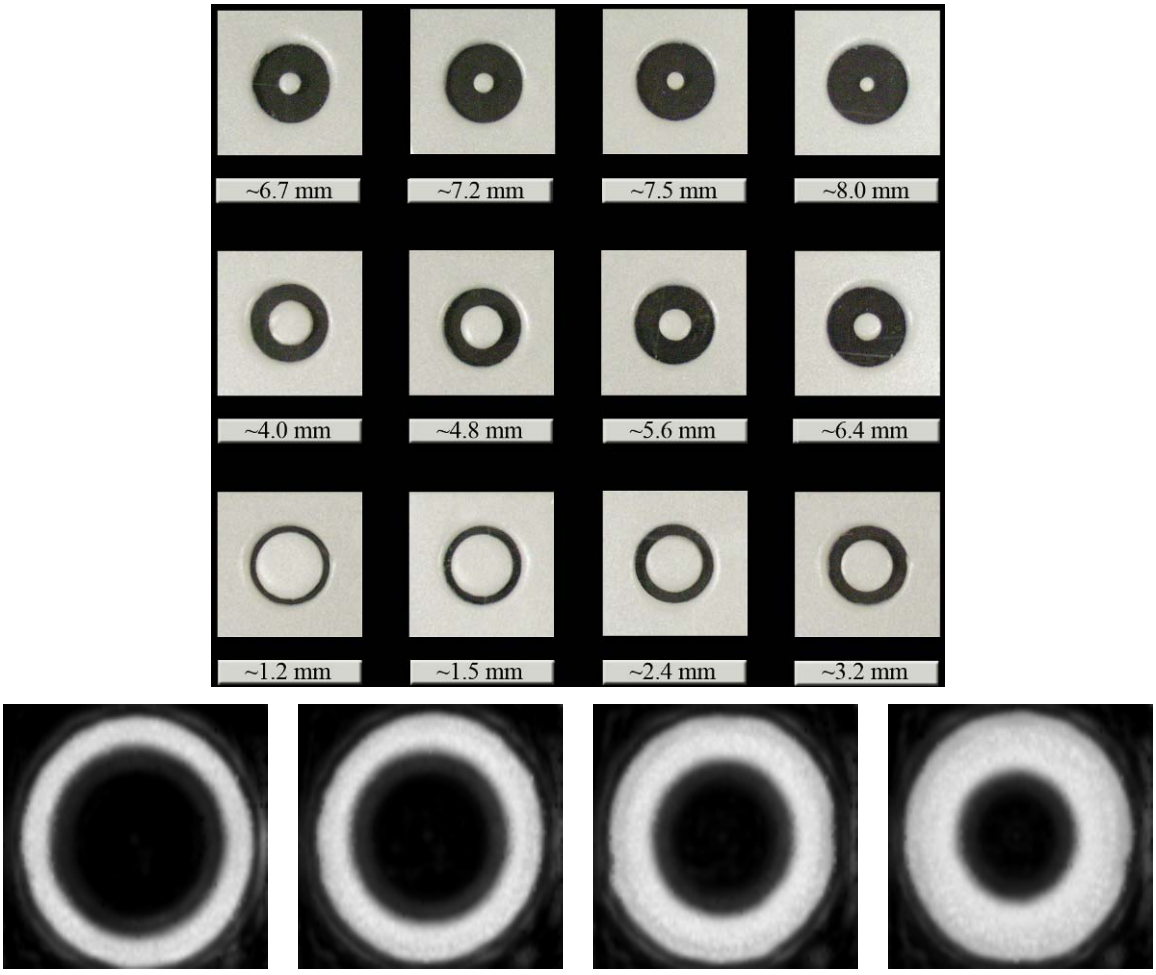

gap: ~1.2mm gap: ~1.5mm gap: ~2.4mm gap: ~3.2mm

Figure 3-5. Upper: Photograph of a series of annular apertures with different sizes of opening gaps. Lower: Sample C-scan images of several apertures obtained without target (water only).

3.4.2 Design of the Measurement

In order to model the average ultrasound forward scattering effect, an annular aperture was attached to the surface of the imaging target in order to confine the effective areas of incident ultrasound plane waves and ultrasound image were subsequently acquired using the C-scan prototype #2 at a frequency of 5MHz with the configuration shown in Figure 3-6(A). Figure 3-6(B) displays the residual of attenuated primary ultrasound beams and the scattered energy coming out from the annular aperture.

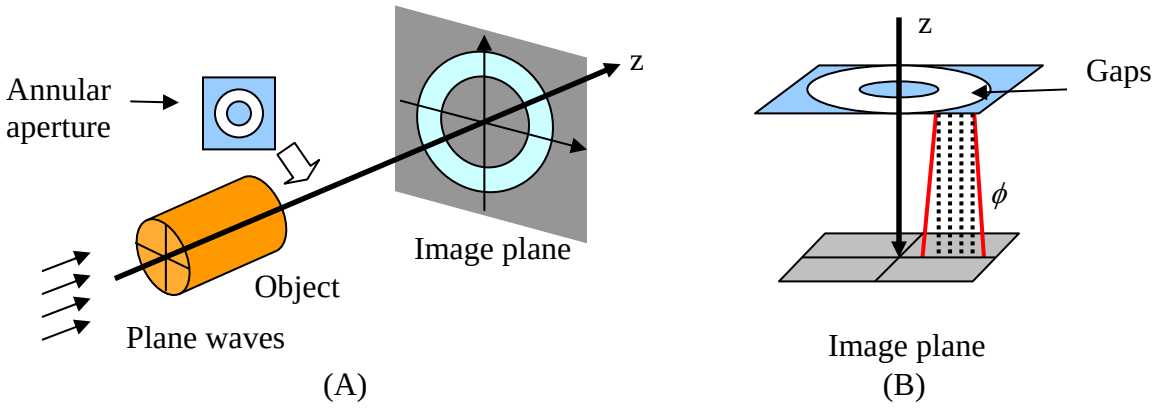

Figure 3-6. (A) Diagram of the experiment configuration. (B) The residual of the attenuated primary beams and the scattered energy coming out from the annular aperture.

Since the incident ultrasound beam is a plane wave which propagates through a uniform material, an analytical approach to determine the scatter distribution from the ultrasound images of the annular aperture was formulated. Taking into consideration that the detected ultrasound energy is comprised of the residual of the attenuated ultrasound primary energy and the multi-scattered energy through the gap areas of the aperture (see Figure 3-7), the detected ultrasound energy can be expressed as:

$$I_{\text{Detected}}(d,p,r,L) \approx I_{\text{Att\_primary}}(d,p,r,L) + \int_{r\in R}\oint_{\theta_a} S_{\text{Scatter}}(d,p,r,L)\cdot r dr \cdot d\theta_a \qquad (3.36)$$

where d is the thickness of the soft-tissue phantom, p is the pixel number at the detector, r and R are the inner and outer radii of the annular aperture respectively, L is the distance between the annular aperture and the detector, θ_a is the circular angle of the annular aperture, $I_{detected}$ is the intensity that detected by the sensor array, $I_{Att\_primary}$ is the residual of the attenuated primary intensity, and $S_{scatter}$ denotes the function of the scattering energy distribution. The ultrasound scattering angle ϕ can be determined by the locations of p, r and distance L between the annular aperture and the detector.

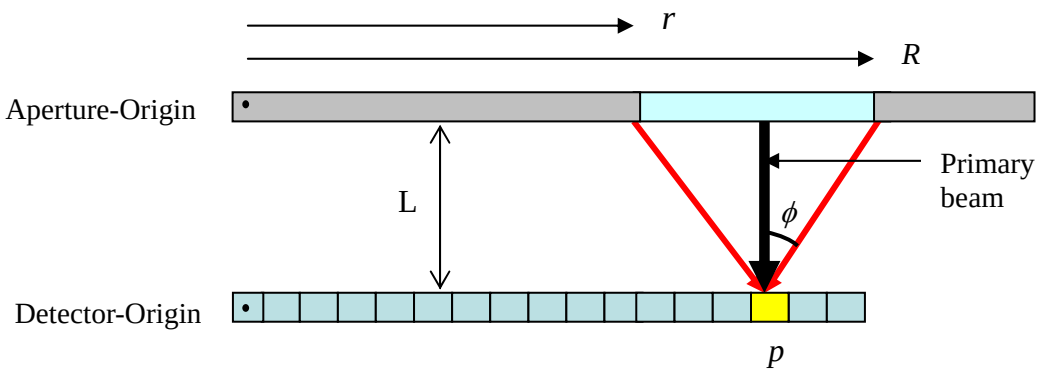

Figure 3-7. The ultrasound primary beam and scattering energy propagated through an annular aperture to the detector array.

3.4.3 Solution for the Forward Scattering Distributions (Arc Scattering Model)

The ring ultrasound images of the phantoms were further analyzed by calculating the average radius intensity over 360 degree. An arc scattering model was established to estimate the scattering distribution according to the distance between the scattering source and the detecting pixel (see Figure 3-8).

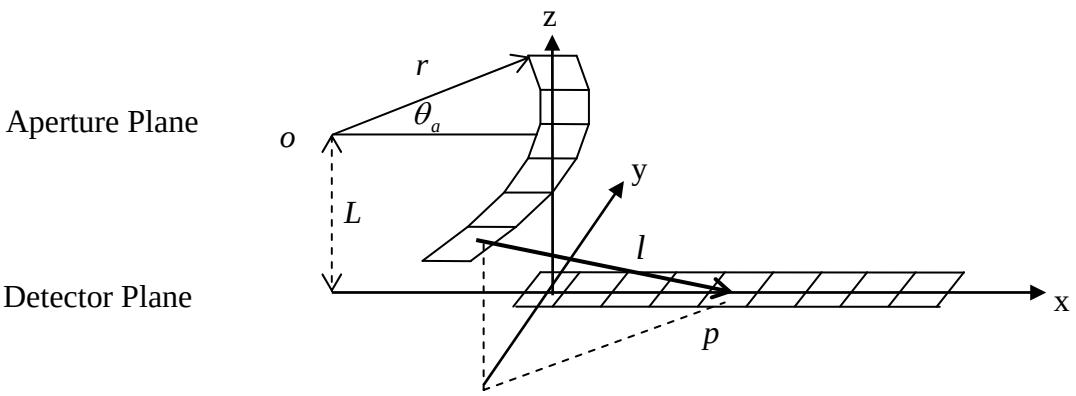

Figure 3-8. An illustration of the arc scattering model. The upper plane is the scattering surface of the phantom and the lower plane is the detecting array. r is the inner radius of the annular aperture; L the distance between the two planes; and l the distance from the arc scattering location to the detecting pixel.

Ideally, the scattering source is a complete ring of the aperture ($\theta_a = 2\pi$) and a detecting pixel, p, receives scattering energy from all elements on the opening gaps of the annular aperture. For the computational purpose, Equation 3.36 can be approximated by a discrete format as follows:

$$I_{\text{Detected}}(d, p, r, L) \approx I_{\text{Att\_primary}}(d, p, r, L) + \sum_{r \to R} \sum_{2\pi} S_{\text{Scatter}}(d, p, r, L) \cdot r\Delta r \cdot \Delta\theta \qquad (3.37)$$

where $I_{\text{Att\_primary}}(d, p, r, L)$ exists only when p is located under the direct beam (opening gap) of the aperture.

3.4.4 Algebraic Reconstruction Techniques (ART) Estimation

Distances between the scattering source along the opening gap of the annular aperture and the specific receiving location p were calculated based on the ring scattering model (refer to Section 3.4.3). A linear interpolation method was applied to decompose each calculated distance (l) into length weighting factors with corresponding energy factors. For instance, if the distance is 10.7 pixels away from the detecting pixel p, the detected energy can be represented by the combination of two weighting factors of 0.7 at s11, which is the energy coefficient (per square pixel) of the 11th pixel away from the origin, and 0.3 at s10. Consequently, for a fixed object thickness d and distance L, the total detecting energy from the annular aperture to a detector pixel p can be written as:

$$I_{\text{Detected}}(p) = \underline{I_{Att\_primary}(p)} + \sum_{i=0}^{p} \sum_{j=0}^{N} C(i, j) S(j) \qquad (3.38)$$

$$I_{\text{Detected}}(p) = \underline{c_{p,0} s_0} + c_{p,1} s_1 + c_{p,2} s_2 + \Lambda\ c_{p,N} s_N \quad ; \qquad (3.39)$$

and $\begin{cases} c_{p,0} = 0 & , when \quad p \text{ is in the geometrical shadow (blocked).} \\ c_{p,0} = 1 & , when \quad p \text{ is under the direct beam (opening gaps).} \end{cases}$

where $I_{\text{Detected}}(p)$ is the total received intensity at pixel p, $\{c_{i,j}\}$ is the calculated length factors using the arc scattering model, $\{s_j\}$ is the corresponding energy coefficients, s_0

equals to the $I_{\text{Att\_primary}}(p)$, which is the residual of attenuated primary intensity under the ring opening gaps of the annular aperture, and N represents a preset threshold of the maximum effective scattering length ($s_N \approx 0$) in pixels. A series of linear equations with respect to Equation 3.39 for all receiving pixels was established.

$$\begin{aligned} I_{\text{Detected}}(1) &= \underline{c_{1,0}s_0} + c_{1,1}s_1 + c_{1,2}s_2 + \Lambda\ c_{1,N}s_N \\ I_{\text{Detected}}(2) &= \underline{c_{2,0}s_0} + c_{2,1}s_1 + c_{2,2}s_2 + \Lambda\ c_{2,N}s_N \\ &\text{M} \\ I_{\text{Detected}}(p) &= \underline{c_{p,0}s_0} + c_{p,1}s_1 + c_{p,2}s_2 + \Lambda\ c_{p,N}s_N \end{aligned} \qquad (3.40)$$

Due to the noise contained in the measurement data, the conventional direct matrix inversion method may not be applicable to find the solution of equation (3.40). Therefore, the algebraic reconstruction techniques (ART) method[67], which is less sensitive to noise components, was performed to compute the average forward scattering coefficients.

$$\vec{S}^{(i)} = \vec{S}^{(i-1)} - \frac{(\vec{S}^{(i-1)} \cdot \vec{C}_i - \vec{I}_i)}{\vec{C}_i \cdot \vec{C}_i} \vec{C}_i \qquad (3.41)$$

where $\vec{S}^{(i)}$ represents the *i*th computed solution set of the scattering coefficients, $\vec{I}_{(i)}$ is the detected intensity and $\vec{C}_{(i)}$ is the *i*th row coefficients of the linear equations in $\vec{C}$.

If the scattering distribution decreases with the distance from the origin, the relationship of the scattering coefficients can be presented by $s_0 > s_1 \Lambda > s_N \geq 0$. Based on this assumption, a solution set of $\vec{S}^{(0)} = s_0, s_1, \Lambda, s_N$ ($s_N \approx 0$) was selected as the initial input for the ART method. For each phantom, an approximation set of the scattering coefficients was then obtained.

3.5 Imaging Restoration

Image deconvolution techniques have been developed by many researchers to reduce speckle and/or noise of conventional B-scan ultrasound images for practical or research purposes[47-49]. In general, the PSF describes the impulse response of an imaging system to a point source. The relationship between the detected image, original image and the PSF can be represented by

$$image(x, y) = original(x, y) \otimes PSF(x, y) \qquad (3.40)$$

where $\otimes$ denotes convolution.

In equation 3.35, we assume that the detected ultrasound intensity in C-scan geometry is comprised of the residual of attenuated primary intensity and multiple scattering intensities. Therefore, a C-scan ultrasound image can be approximated by a convolution process of the original image without scattering effects and the scattering function. The ultrasound forward scattering distribution (FSD) can be used to restore the original intensity attributed to the primary beam without the influence of scattering. The relationships between the detected image, de-scatter image (image without scattering effects) and the scattering distribution function are specified as:

$$image(x, y) = de - scatter(x, y) \otimes f_{scatter}(x, y) \qquad (3.41)$$

After applying the 2-D Fourier Transform, Equation 3.40 can be rewritten as:

$$FT\{image(x, y)\} = FT\{de - scatter(x, y)\} \cdot FT\{f_{scatter}(x, y)\} \qquad (3.42)$$

The image restoration process can be accomplished by applying the 2-D image deconvolution method as stated in the following equation:

$$de - scatter(x, y) = IFT\{\frac{\text{Image}(u, v)}{F_{scatter}(u, v)}\} \qquad (3.43)$$

where *IFT* denotes the 2-D inverse Fourier Transform. $\text{Image}(u, v)$ and $F_{scatter}(u, v)$ are the 2-D Fourier Transform of $\text{image}(x, y)$ and $f_{scatter}(x, y)$. Note that this image restoration process is employed to reduce the forward scattering effects contained in the detected C-scan image.

3.6 Analyses of Images and Scattering Distributions

3.6.1 Analyses of Ultrasound Ring Images

The size of each ultrasound ring image was 200 x 200 pixels. In order to find the average radius distribution of each ring, an averaging process over the 360 degree of the annular image was applied. Figures 3-9 (A) to (F) illustrate the ultrasound ring images and their average intensity distributions along the radius. Due to the differences in object thicknesses and focus lengths, each pixel in the 12mm, 23mm and 31mm ultrasound ring images represented 0.1246 mm, 0.1044 mm and 0.0979 mm respectively. The actual opening gaps of ring images were also determined for the usage of the arc scattering model. Several diffraction effects were visible particularly around the edge of the 12mm ring image illustrating in Figure 3-9 (A). Note that some diffraction effects were observable close to the edge of the ring images.

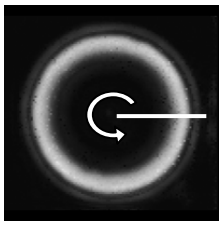

(A)

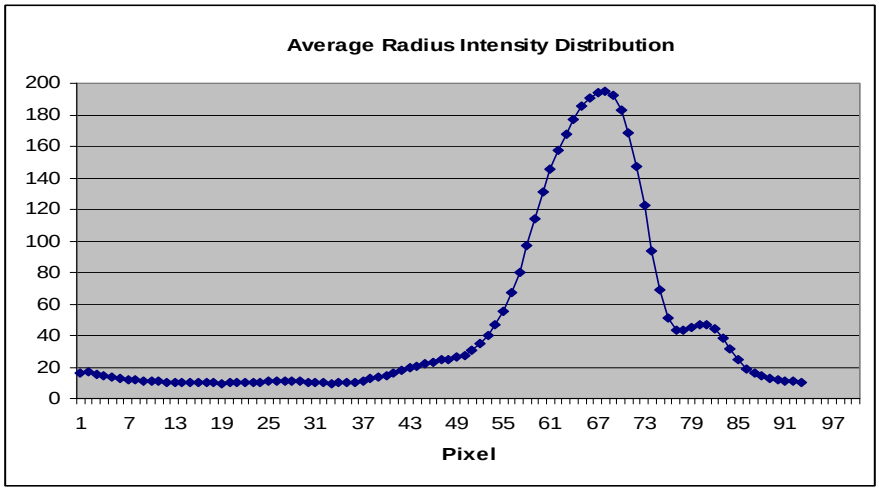
Average Radius Intensity Distribution
200
180
160
140
120
100
80
60
40
20
0
1 7 13 19 25 31 37 43 49 55 61 67 73 79 85 91 97
Pixel

(B)

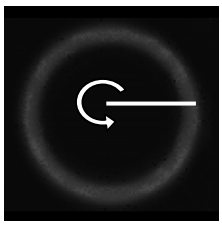

(C)

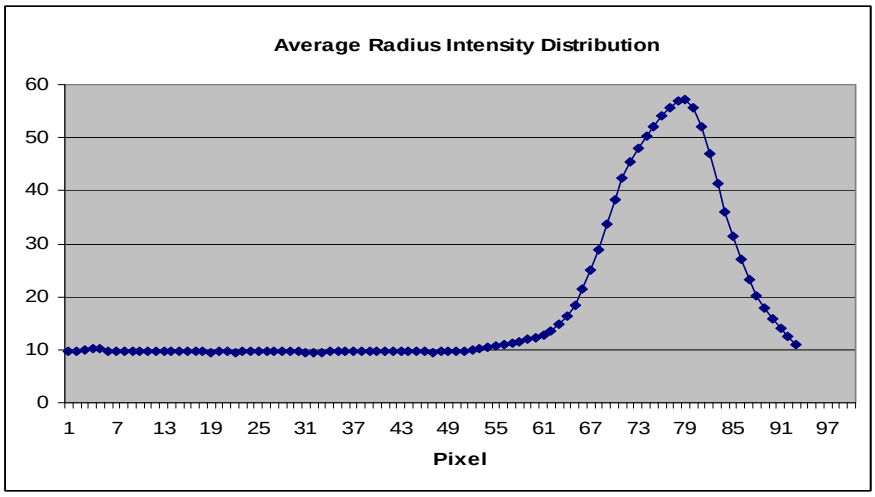
Average Radius Intensity Distribution
60
50
40
30
20
10
0
1 7 13 19 25 31 37 43 49 55 61 67 73 79 85 91 97
Pixel

(D)

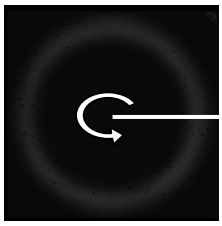

(E)

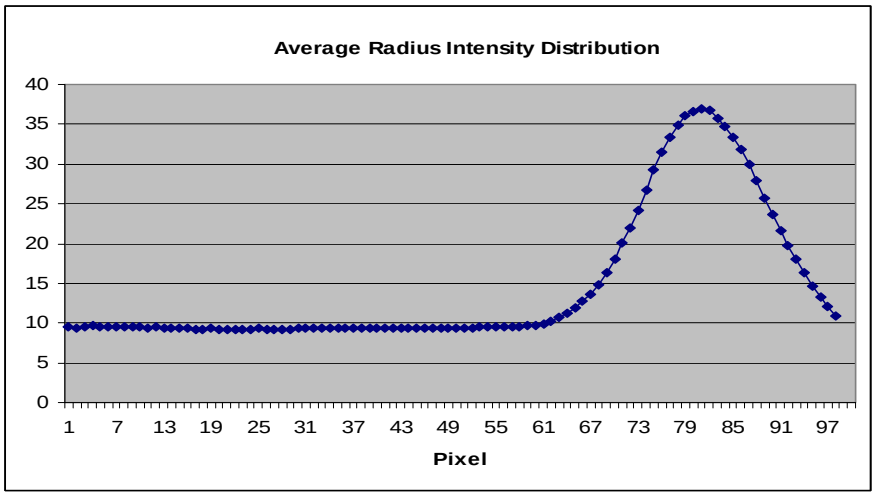
Average Radius Intensity Distribution
40
35
30
25
20
15
10
5
0
1 7 13 19 25 31 37 43 49 55 61 67 73 79 85 91 97
Pixel

(F)

Figure 3-9. (A)(C)(E) Ultrasound ring images of 12mm, 23mm, and 31mm soft-tissue phantoms respectively. Each image is at 200x200 pixels. (B)(D)(F) Plots of average radius intensity distribution.

3.6.2 Forward Scattering Distribution and Modulation Transfer Function (MTF)

For each ultrasound ring image of the test phantom, the FSD was computed by the ART method described in Section 3.3.4. Results of the computed FSDs and their normalized FSDs for three phantoms are plotted in Figure 3-10. Figure 3-11 displays the computed average radius intensity plots for the phantoms. Since the ART method estimates the coefficients with minimum errors, the results demonstrated that the measured intensity can be approximately matched with the computational method.

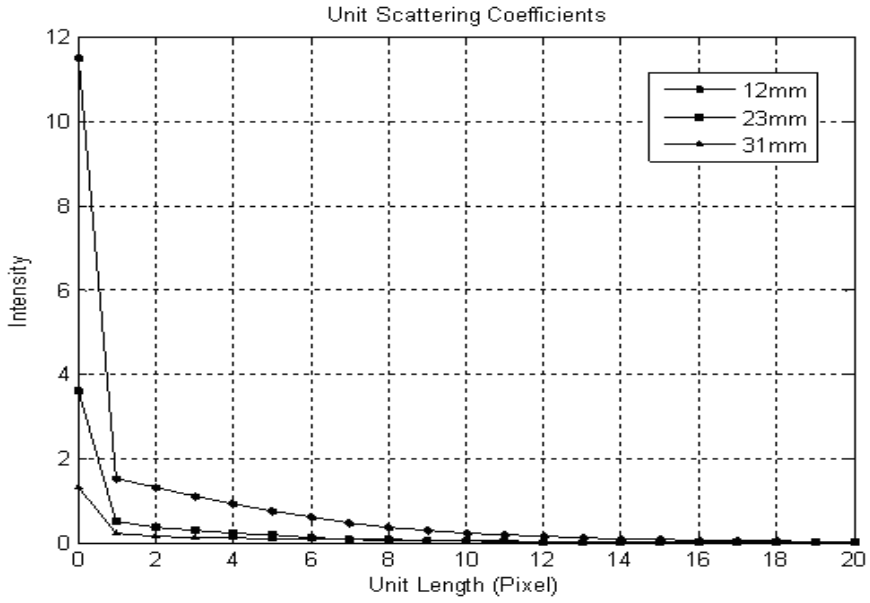

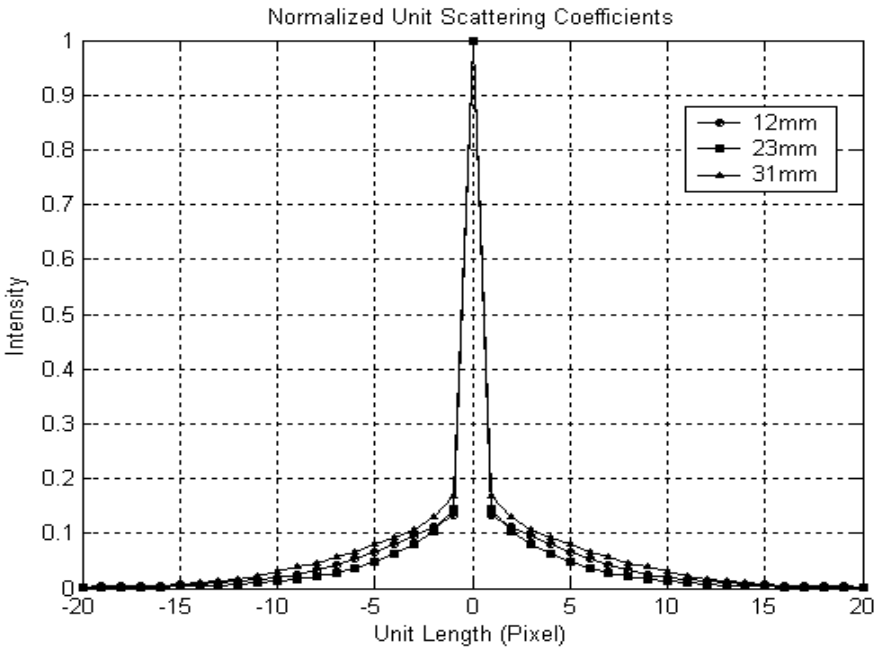

Figure 3-10. The computed FSD coefficients (top) and normalized unit scattering distributions (bottom) of phantoms with thicknesses of 12mm, 23mm and 31mm.

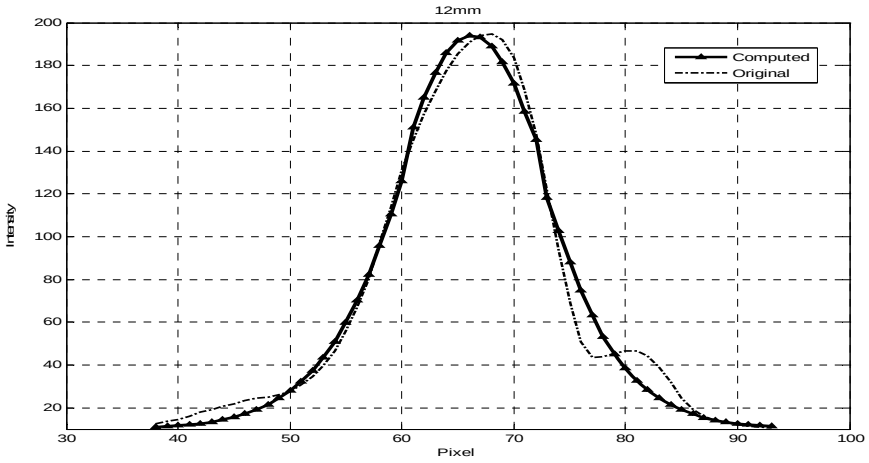

(A)

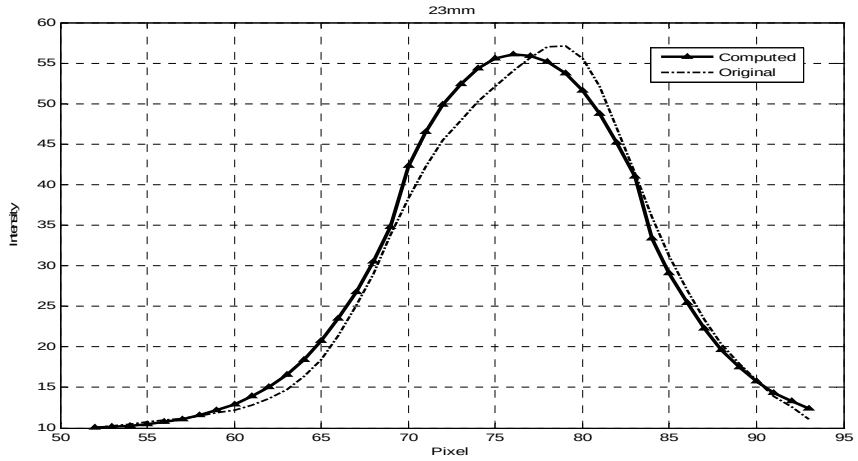

(B)

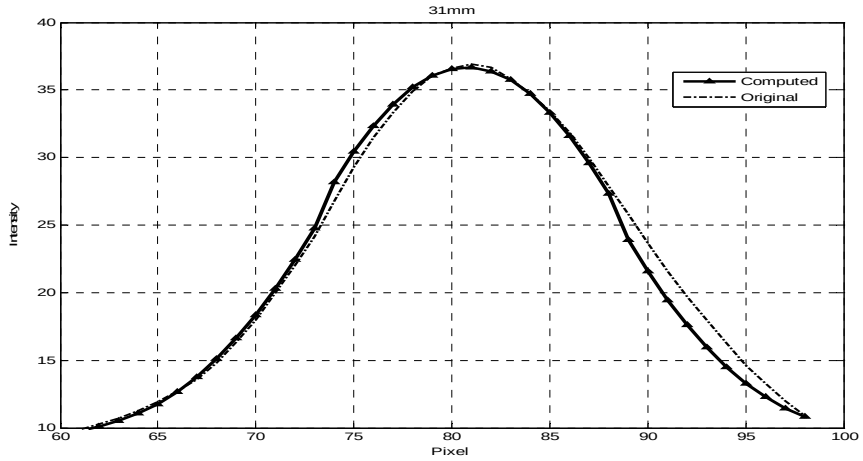

(C)

Figure 3-11. (A)(B)(C) The computed intensity plots vs. the original average radius intensity for 12mm, 23mm, and 31mm phantoms, respectively.

In addition, the *modulation transfer function* (MTF) curve, which is the Fourier Transform of PSF, can also be computed as shown in Figure 3-12. It is seen that the spatial resolution is ranged from 1.2 to 1.4 line pairs per millimeter (based on 10% of the MTF) for 12mm to 31mm thickness of soft-tissue phantoms when the C-scan prototype #2 is operated at 5MHz.

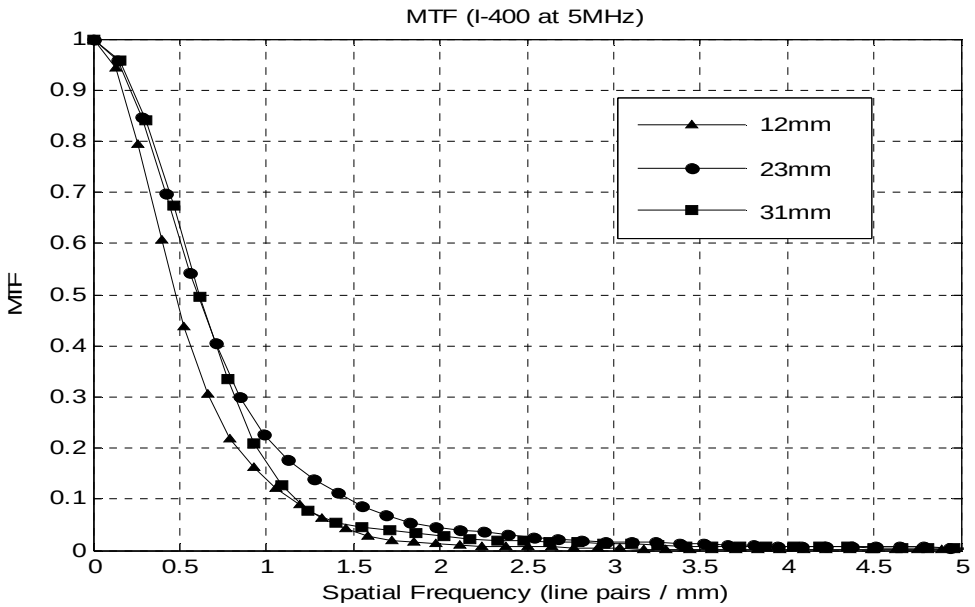

Figure 3-12. MTF curves for 12mm, 23mm and 31mm phantoms at 5MHz.

3.7 Validation of Computed Coefficients

3.7.1 Verification Using Twersky's General Scattering Model

In accordance with the solution above, the average intensity detected can be projected by its ultrasound absorption and scattering cross sections, detecting angle, object thickness and the density of the scatters (number per unit volume). According to the measurements of the physical configuration of the C-scan prototype #2, major quantities required in the Twersky's scattering model (refer to equation 3.29) were obtained. The intensity ratio plots of the total detecting intensity (I_d) over the original incident intensity (I_0) based on Twersky's model are illustrated in Figure 3-13. Since the attenuation coefficients of absorption (α_a) and scattering (α_s) were unknown, two curves were plotted representing the α_s which equaled to 10% and 30% of the total attenuation coefficient α. Note that the attenuation coefficient is the sum of the absorption and scattering coefficients ($\alpha = \alpha_s + \alpha_a$). Results indicated that the scattered energy measured by the C-scan prototype #2 (with 2-D array, I-400) for the three

phantoms were ranged by 10%~20% of the total attenuation. It is higher than 5%~10% in other soft tissue samples measured by B-scan ultrasound with a 1-D transducer[45, 46].

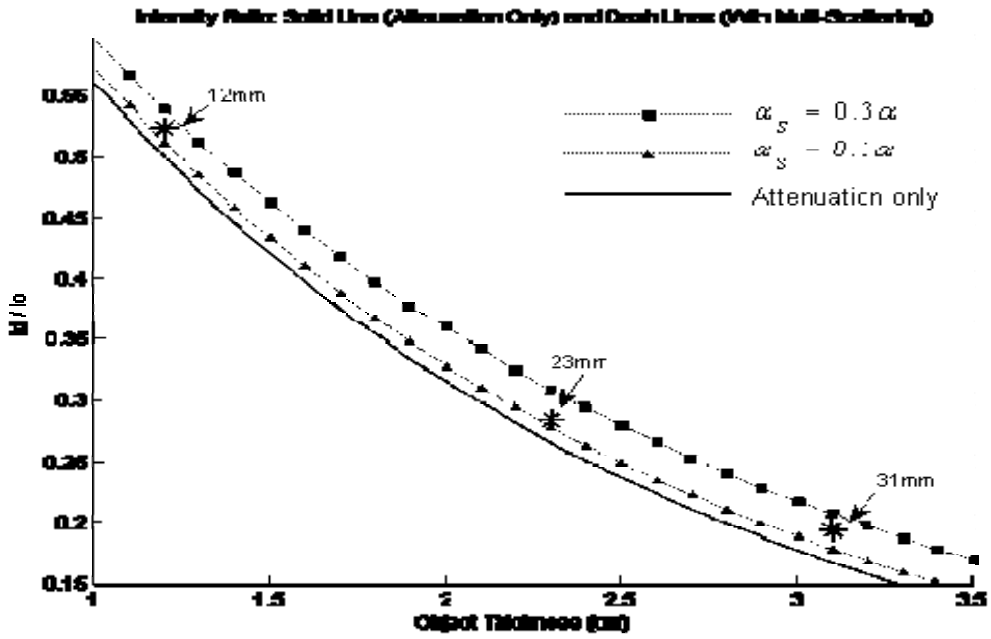

Figure 3-13. Plots of intensity ratio vs. object thickness. Dash curves represent the intensity ratio with different portions of scattering coefficients within the total attenuation. The solid line represents the intensity ratio of attenuation effects along the primary incident beam without considering multiple scattering effects. The star markers represent the intensity ratios of the three phantoms of thickness 12mm, 23mm and 31mm.

The average scattering energy ratio which refers to Equation 3.34 is also illustrated in Figure 3-14. The scattering energy ratio was ranged by 1.1%~1.3% of the incident intensity when the object's average thickness was around 1cm ~ 3cm.

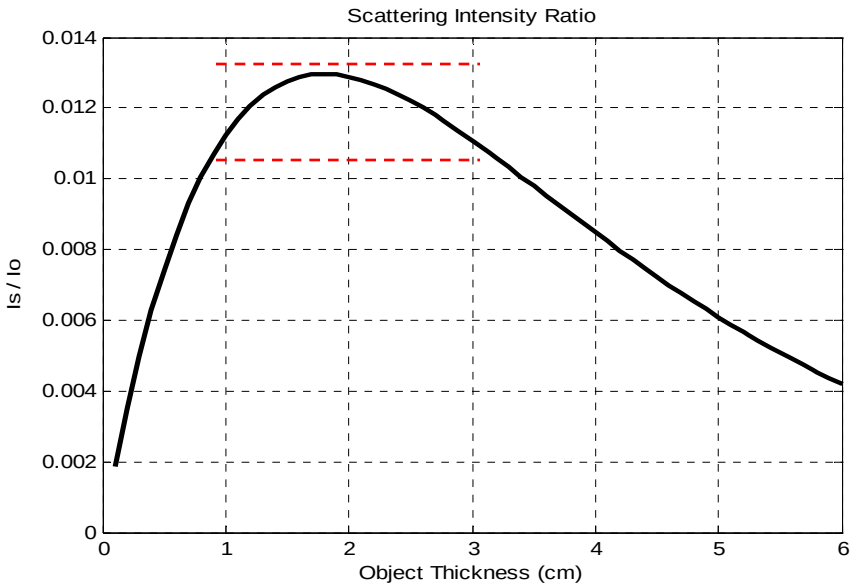

Figure 3-14. Plot of the average scattering intensity ratio vs. the object's thickness based on Twersky's model.

3.7.2 Verification Using Edge Scattering Model and Point Spread Function

To further validate the computed coefficients, the PSF of the ultrasound edge image and the computer simulated PSF using the computed FSDs were compared. For each of the three phantoms, the edge ultrasound image was acquired by the same setup using an edge collimator made from the same high attenuation material as in this experiment. Refer to section 2.5.4, the relationship between the ESF and its PSF were specified using

$$PSF(x) = \frac{d(ESF)}{dx} \qquad (2.14)$$

An edge scattering model was established similar to the arc scattering model mentioned in Section 3.4.3 (see Figure 3-14). The length factors {C} of the total edge scattering energy received by each detecting location were also calculated.

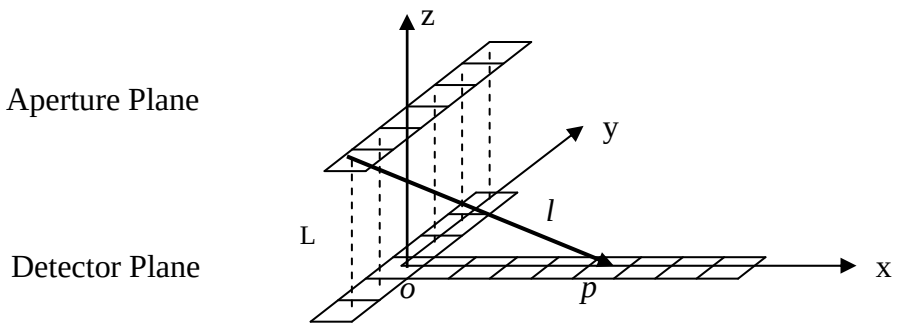

Figure 3-15. An illustration of the edge scattering model: The upper plane (z = L) is the scattering surface of the phantom and the lower plane (z = 0) is the detecting array. L is the distance between the two planes and *l* is the distance from the edge scattering location to the detecting pixel *p* .

The computed FSDs were then introduced to the edge scattering functions of the receiving pixels in order to calculate the FSD-based PSF. The edge-based PSFs were obtained by applying the derivative method (i.e., Equation 2.14) to the average horizontal line intensity of the edge ultrasound images. Edge ultrasound images of three phantoms and the comparative plots of the FSD-based PSFs and the edge-based PSFs are illustrated in Figure 3-16 (A) to (F). It can be clearly observed here that these PSF plots have very similar distributions.

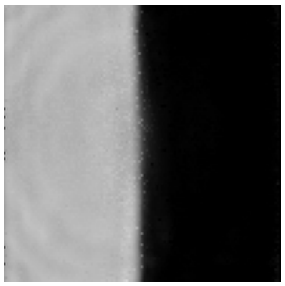

(A)

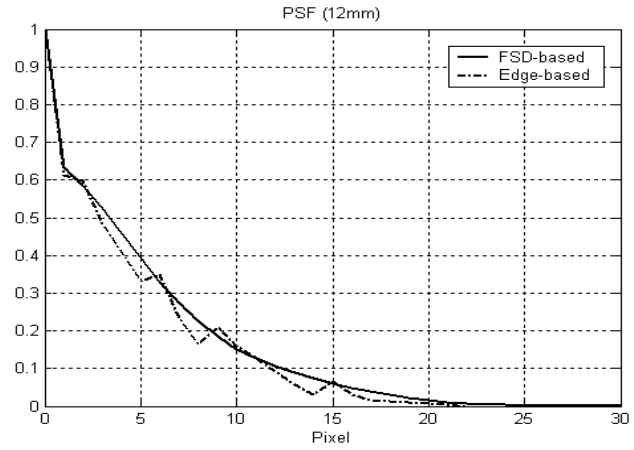

(B)

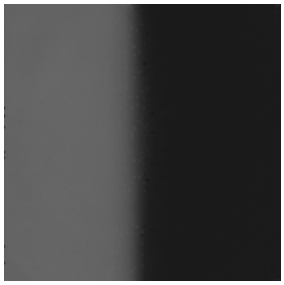

(C)

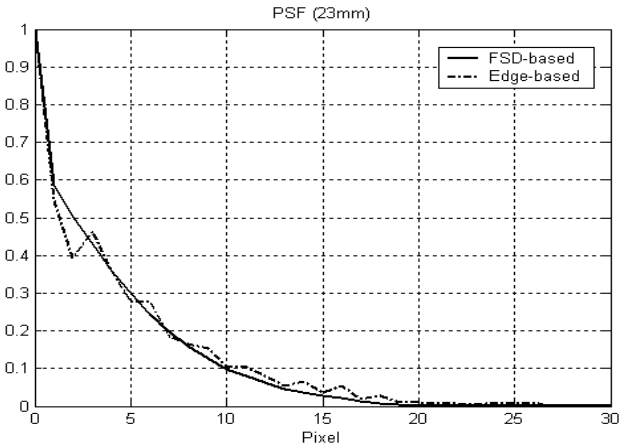

(D)

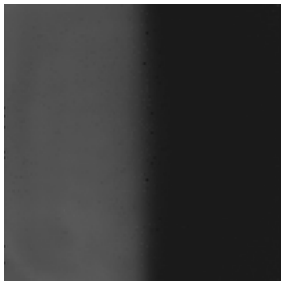

(E)

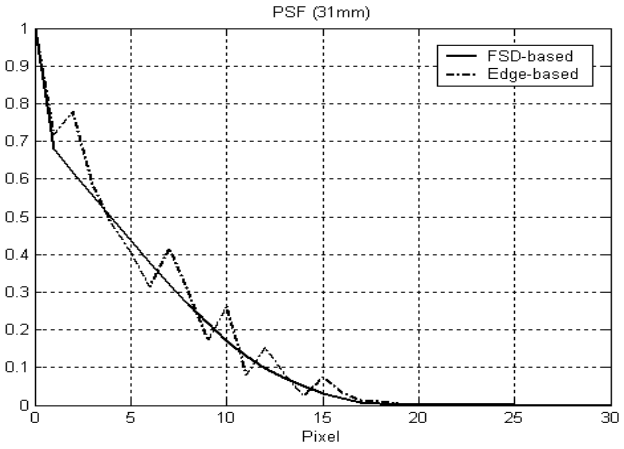

(F)

Figure 3-16. (A)(C)(E) Edge ultrasound images for the three phantoms with thicknesses of 12mm, 23mm and 31mm respectively. (B)(D)(F) Plots of the normalized edge-based PSFs (dash lines) and FSD-based PSFs (solid lines).

Figure 3-17 illustrates the intensity distributions of the FSD-based PSF and FSD coefficients for the 12mm phantom. The intensity plots show that the FSD is a small portion of the PSF in C-scan ultrasound. The major function of using FSD in the image restoration process is to enhance the blurry edges caused by forward scattering effects in C-scan images. The result indicates that by applying the computed PSF in the image restoration process may reveal more noise patterns due to its wider distribution.

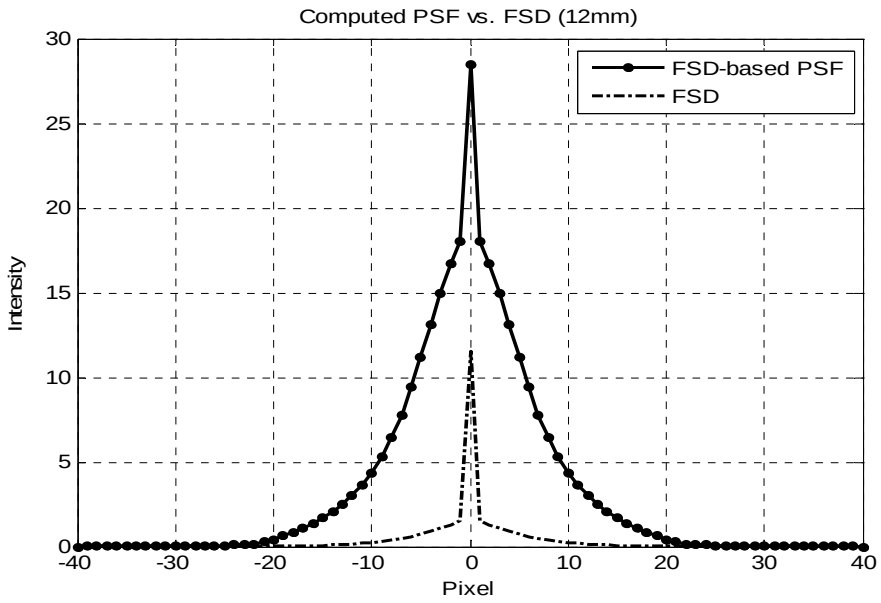

Figure 3-17. Plots of intensity distributions of FSD-based PSF and FSD for the 12mm phantom.

3.8 Ultrasound Image Restoration of Tissue Specimens

For the demonstration of reducing forward scattering effects in C-scan images, restorations of several images of a human fingertip in vivo, a breast tissue specimen, and a breast reduction tissue specimen were performed in this study. The thicknesses of these samples imaged by the C-scan prototype #2 ranged from 9 mm to 14 mm, thus, we selected the FSD of 12mm Zerdine for the image restoration. C-scan ultrasound images of these samples and their corresponding scattering-corrected images are shown in Figures 3-18 to 3-20. Note that a standard 3×3 median filter was applied to the restored images in order to suppress the induced noises.

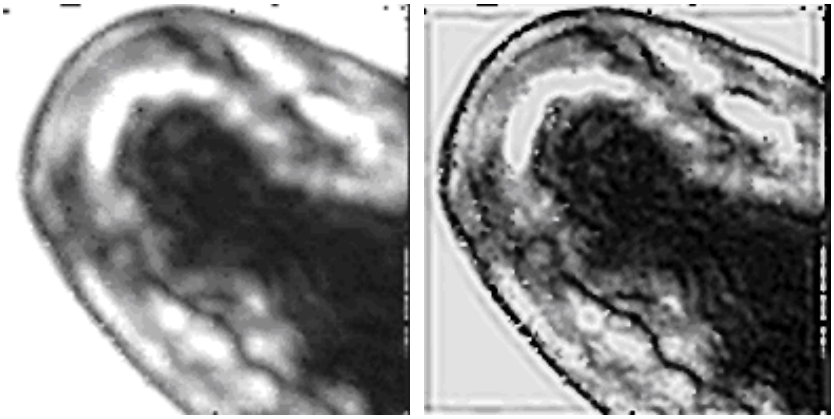

(A) (B)

Figure 3-18. (A) The ultrasound image of a human finger tip, which has approximate dimensions of 2.0cm × 1.7cm × 1.4cm, generated by the C-scan prototype #2 at 5MHz. (B) Its processed image with the 12mm scattering filter.

(A)

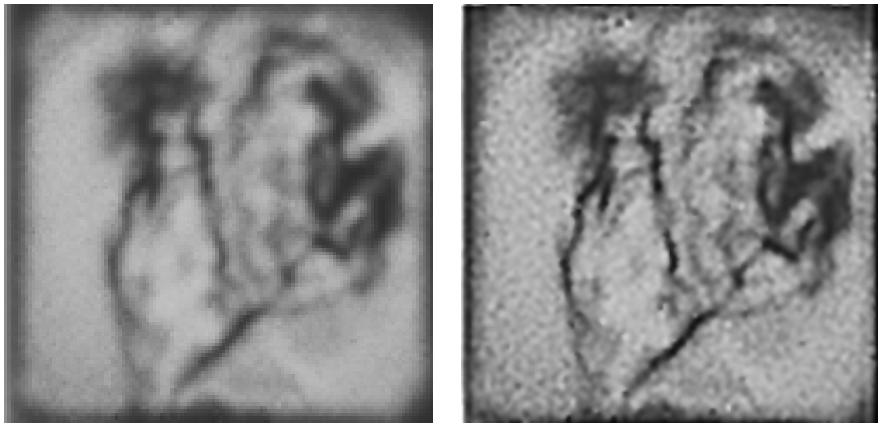

(B) (C)

Figure 3-19. (A) Photograph of a breast tissue specimen which has approximate dimensions of 2.5cm × 2.0cm × 1.1cm. (B) The ultrasound image of the specimen directly taken by the C-scan prototype #2. (C) Its processed image using the 12mm scattering filter.

(A)

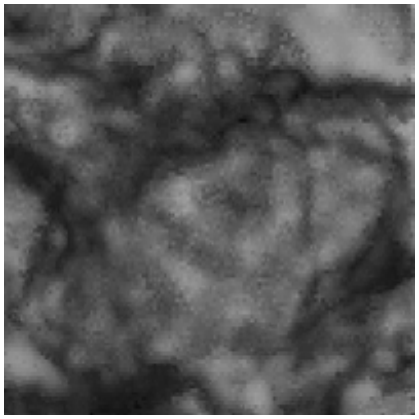

(B)

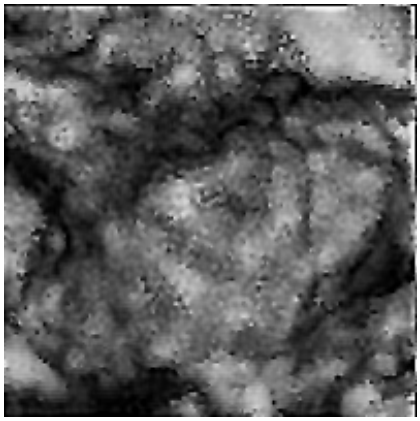

(C)

Figure 3-20. (A) Photograph of a breast reduction tissue specimens consisted of fat, fibrous tissue, mammary glandular tissue and blood vessel with approximate dimensions of 2.5cm × 2.0cm × 0.9cm. (B) The ultrasound image of the specimen directly taken by the C-scan prototype #2. (C) Its processed image using the 12mm scattering filter.

Figure 3-21 demonstrate the intensity comparison plots of the original C-scan image and the scatter-reduced images shown in Figure 3-18. It is illustrated that the blurry edge pattern can be enhanced by applying the image restoration process with the selected FSD.

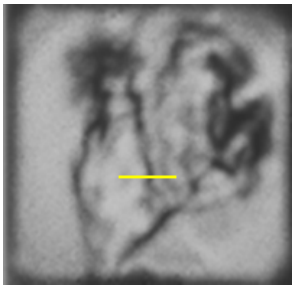

(A)

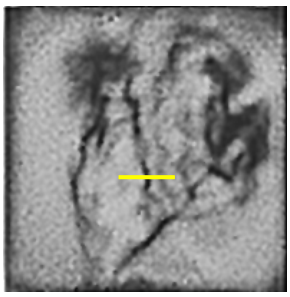

(B)

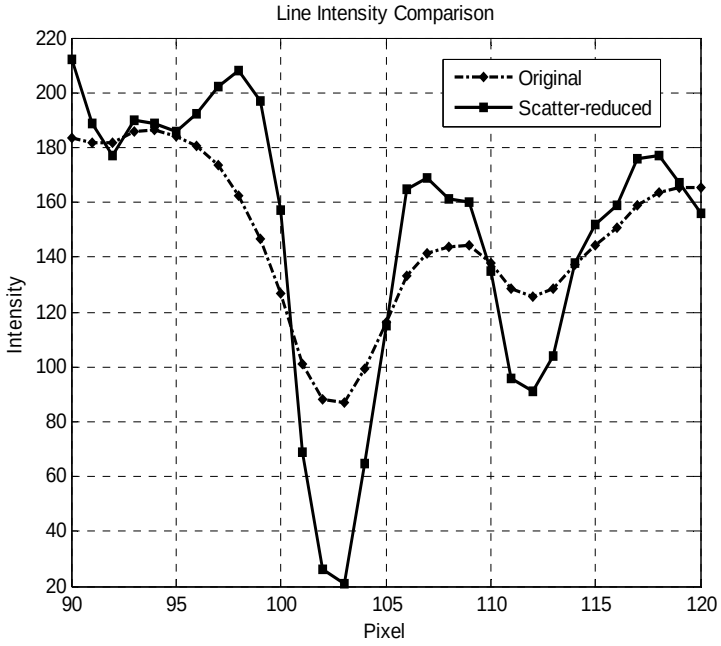

(C)

Figure 3-21. (A) The original C-scan image, (B) the scatter-reduced image, and (C) the horizontal intensities plots of the indicated edge patterns in the original image (dashed line) and the processed image (solid line).

3.9 Summary

In this chapter, we addressed and demonstrated an annular aperture-based analytical method of modeling the average forward scattering distribution of three soft tissue mimicking phantoms made of Zerdine™. By analyzing the annular C-scan images with the proposed method, the forward scattering distribution (FSD) of each phantom was computed. Although the attenuation components are significantly different with the three thicknesses of phantoms, we found that the normalized FSDs have similar distributions. This is due to the fact that the average forward scattering intensity ratio of the three soft-tissue phantoms is very close in Twersky's multiple scattering model (refer to Appendix A). It is shown that the average scattering energy ratio is ranged by 1.1%~1.3% of the incident intensity when the object's average thickness is around 1cm ~ 3cm.

According to Twersky's solution, the soft-tissue mimicking material (Zerdine™) has higher scattering effects, 10%~20%, among the total attenuated intensity in our C-scan configuration comparing to 5%~10% in other soft tissue specimens measured by B-scan ultrasound with one-dimensional linear probes. Therefore the scattering energy component is considered to be one of the main causes of blurry artifacts in a C-scan image. For the demonstrations of reducing scattering effects in C-scan images, examples of the image restoration process were performed by applying the approximate soft tissue FSDs according to the average thickness of several tissue specimens. The restored C-scan images showed sharper edges and more detail in each scattering-corrected image as compared to their unprocessed counterparts.

Chapter 4

Ultrasound Computerized Tomography

Computerized Tomography (CT) refers to the cross-sectional imaging of an object from either projection data or reflection data which are collected by illuminating the object from different directions. This technology has been utilized in many medical applications such as X-ray CT[68-70], single photon emission computed tomography (SPECT)[71-73], positron emission tomography (PET) [74-77], optical coherence tomography (OCT) [78-81], and magnetic resonance imaging (MRI) [82-84]. However, some of these applications require utilization of ionizing radiation source or injection of radioactive tracer isotope into the patient for the acquisition of image. The OCT technique has a limitation of penetrating approximately up to 0.5 ~ 1cm below the surface in biological tissue. MRI is a relatively new technology for visualizing the internal structure and function of the body without radiation. Nevertheless, the cost of having an MRI scan is relatively expensive as compare to x-ray and ultrasound.

Ultrasound CT has been applied to image the breast and other medical applications historically. General approaches of the ultrasound CT have been investigated by many researchers in either reflection[85-87] or transmission[88-91] geometry. For the

transmission geometry, conventional methods of the CT reconstruction for ultrasound includes: time-of-flight[92, 93] and attenuation[94] (analogous to the X-ray tomography approach) for different types of ultrasound imaging systems. The time-of-flight method estimates the distribution of speed-of-sound in the transmitted ultrasound energy; while the attenuation method reconstructs CT images based on the measured attenuation information. In this investigation, the imaging geometry of the proposed C-scan prototypes is similar to conventional X-ray devices and therefore we employed the attenuation-based method for CT reconstruction.

The C-scan ultrasound described in this research has the ability to generate real-time, speckle-free, and no geometric-distortion images. Based on the developments we made to the C-scan prototypes, the spatial resolution of C-scan images was increased from ~500 micron to ~350 micron for prototype #1 and #2, respectively (refer to Chapter 2). Thus, we believe that the proposed C-scan prototypes may have the potential to perform ultrasound computerized tomography and possibly 3-D ultrasound. General attenuation-based approaches of the ultrasound CT investigations will be briefly discussed in the following sections.

4.1 Computerized Tomography

4.1.1 Fundamentals of Computerized Tomography

In 1917, Radon was the first to discover the mathematical basis for CT. It was not until 1972, when G. N. Hounsfield and Allan McCormack [95] received a Nobel Prize for inventing the first CT scanner. Since then, many advances have been accomplished in scanner technology and the algorithms used for CT reconstruction [68, 96, 97] .

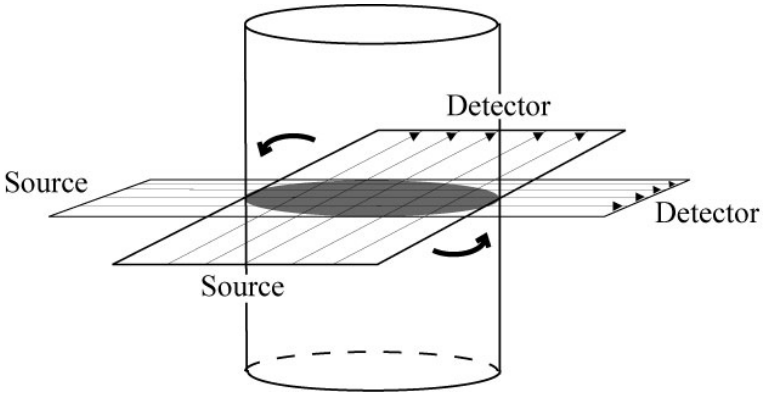

Figure 4-1. A simple parallel beam scanning system.

Fundamentally, tomography is an image which reconstructs an object from its projections. A series of rays, in either parallel, fan, or cone formation, pass through an object, and the attenuated signals of these rays are measured by placing an array of detectors on the receiving side in the scanning geometry as shown in Figure 4-1. The measurement in the bank of the detector is a profile of the scan. In order to collect a complete set of profiles (or sinograms), the object is usually scanned by rotating the angle from 0 to 180 degrees.

4.1.2 Projection and Fourier Slice Theorem

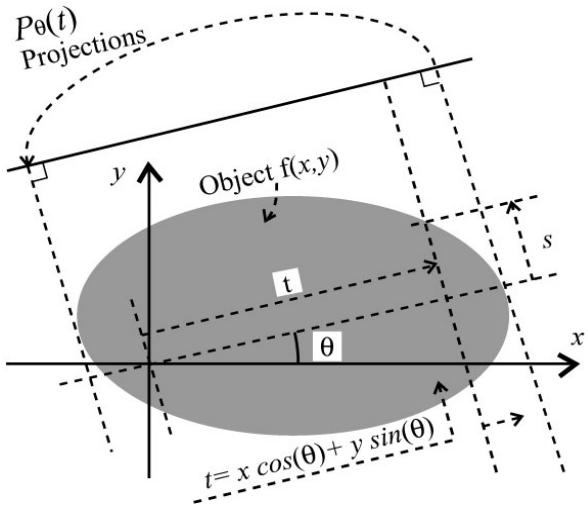

Figure 4-2. Formation of the projection.

In Figure 4-2, x, y represent coordinates inside the object and $f(x,y)$ represents the attenuation coefficient of the object. $t = x\cos(\theta) + y\sin(\theta)$ denotes the line which characterizes one beam traveling through the object and θ is the rotation angle of the projection. The projection which represents the projection of the object at distance t from the center is thus defined as follows:

$$P_\theta(t) = \int_{(\theta,t)line} f(x,y)ds \qquad (4.1)$$

where $t = x\cos(\theta) + y\sin(\theta)$ and $s = -x\sin(\theta) + y\cos(\theta)$. It has also been demonstrated that the above equation can be rewritten using a delta function as follows[96]:

$$P_\theta(t) = \int_{-\infty}^{\infty}\int_{-\infty}^{\infty} f(x,y)\delta(x\cos\theta + y\sin\theta - t)dxdy \qquad (4.2)$$

This function is known as the Radon transform [98, 99] of $f(x,y)$. The delta function in Equation 4.2 specifies that the integral must be along the line of $t = x\cos(\theta) + y\sin(\theta)$. A set of these functions for a constant angle equals the projections of the object at the cross-sections where the beams pass through. When the angle θ is held constantly throughout a projection, parallel projection data can be obtained.

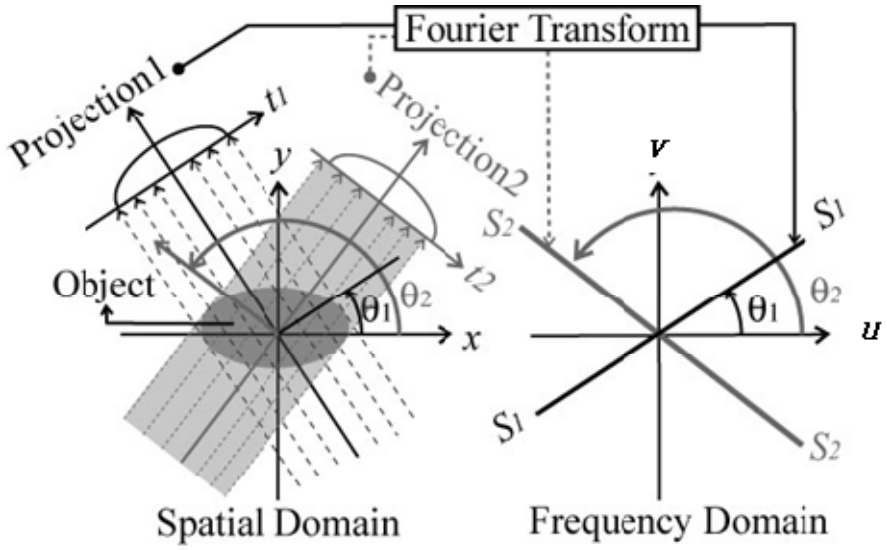

Figure 4-3. Diagram of the Fourier slice theorem.

As stated in the Fourier slice theorem [98, 100], one dimensional Fourier transform of a parallel projection of an object $f(x,y)$ taken at angle θ results in a slice of the 2-D Fourier transform $F(u,v)$, and angle θ with the u-axis (see Figure 4-3). It is also possible to theoretically recover the object by performing a 2-D inverse Fourier transform when an infinite number of projections of an object are obtained. The 2-D Fourier transform of an object $f(x,y)$ is:

$$F(u,v) = \int_{-\infty}^{\infty}\int_{-\infty}^{\infty} f(x,y)e^{-2j\pi(ux+vy)}dxdy \qquad (4.3)$$

where $u = \omega\cos\theta$ and $v = \omega\sin\theta$. And the Fourier transform of a projection at an angle θ is defined as:

$$\begin{aligned} S_\theta(\omega) &= \int_{-\infty}^{\infty} P_\theta(\omega)e^{-j2\pi\omega t}dt \\ &= \int_{-\infty}^{\infty}\int_{-\infty}^{\infty} f(x,y)e^{-j2\pi\omega(x\cos\theta+y\sin\theta)}dxdy \end{aligned} \qquad (4.4)$$

4.1.3 Filtered Back-projection (Frequency Domain)

Applied with the Fourier theory, the Filtered Back-projection (FBP) algorithm[101, 102] develops a closed form solution to locate the linear attenuation coefficient at various points at the cross-section of an object. According to the Fourier slice theorem, a straight line with an angle θ denotes a set of projection data in the frequency domain. The Fourier transform of each projection at all angles will be collected to establish a 2-D frequency space during the back-projection process. The back-projection of a projection profile in the frequency domain is defined by

$$f(x,y) = \int_{-\infty}^{\infty}\int_{-\infty}^{\infty} S_\theta(\omega)e^{j2\pi(ux+vy)}dudv \qquad (4.5)$$

where $S_\theta(\omega) = F(\omega\cos\theta, \omega\sin\theta) = F(u,v)$.

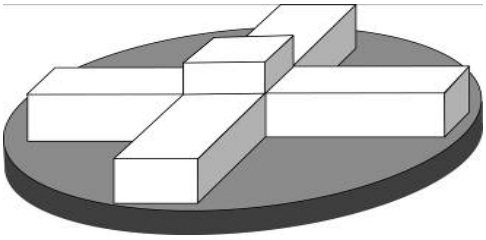

Figure 4-4. Center overlaps of the projections in 2-D frequency space.

The center of summation in the frequency domain is easily over-estimated by adding all projections as demonstrated in Figure 4-4. A weight function $K(u,v)$ must be applied in order to avoid this challenge. The FBP process is expressed by

$$f(x,y)=\int_0^{2\pi}\left[\int_{-\infty}^{\infty}\int_{-\infty}^{\infty}S_\theta(u,v)K(u,v)e^{j2\pi(uxos\theta+v\sin\theta)}dudv\right]d\theta \qquad (4.6)$$

where the term $\int_{-\infty}^{\infty}\int_{-\infty}^{\infty}S_\theta(u,v)K(u,v)e^{j2\pi(uxos\theta+v\sin\theta)}dudv$ indicates the process of filtering and the outer integral represent the back-projection process with respect to all the angles. Several principle filters used in standard FBP are presented in Figure 4-5.

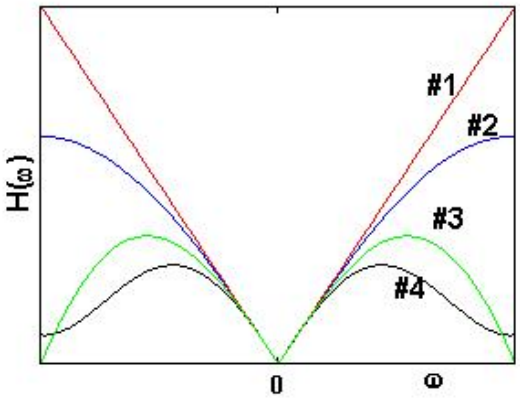

Figure 4-5. Magnitude response of back-projection filters: (1) Ram-Lak (ramp) filter, (2) Shepp-Logan filter, (3) Cosine filter, and (4) Hamming filter.

4.1.4 Filtered Back-projection (Spatial Domain)

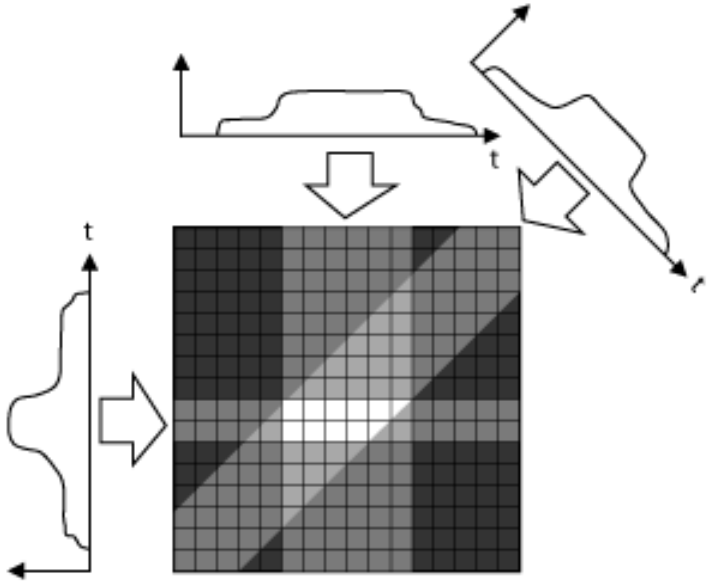

Figure 4-6. Diagram of back-projection in the spatial domain.

So as to back-project the projection profile, the same intensity value in the reconstructive map along the beam traveling direction for each detector line is inputted (see Figure 4-6). A linear interpolation method may be required depending on the rotation angles of the projections. The intensities in the center of the reconstructive map are usually very high yet the detail information may not be observable. Therefore, as the concept illustrated in Figure 4-4, a weight function (filter) is necessary to perform the back-projection in the spatial domain.

The inverse Radon Transform is applied to perform the filtered back-projection method directly in the spatial domain. Considering when $c_\theta(t)$ represents the filtered projection profile at the angle, θ, in the spatial domain, the $c_\theta(t)$ is written by

$$c_\theta(t) = \int_{-\infty}^{\infty}\int_{-\infty}^{\infty} S_\theta(u,v)K(u,v)e^{j2\pi(u\cos\theta+v\sin\theta)}dudv \qquad (4.7)$$

Therefore, the back-projection process is then expressed by

$$f(x,y) = \int_0^{2\pi} c_\theta (x\cos\theta + y\sin\theta) d\theta$$

$$= \sum_{all\ \theta} c_\theta (x\cos\theta + y\sin\theta) \qquad (4.8)$$

4.1.5 Ultrasound CT

Ultrasound CT reconstruction technique is similar to conventional X-ray tomography. In the C-scan configuration, a source emits energy upon the object and a line integral of the attenuation can be estimated by measuring the received intensities on the other side of the object [89, 103, 104]. When the sound beam propagates through a complex tissue structures, the interfaces encountered within the tissue are usually not perpendicular to the beam. However, since the refractive index variations in soft tissues are usually less than 5 %, the beam bending effects are usually not that serious[96].

There are several existing CT reconstruction methods developed for linear detector (e.g. parallel beam and fan beam) or planar detector (e.g. cone beam) [105-107]. However, in this research, the C-scan prototypes employ planar transducers and compact acoustic lens systems which are located at a short distance away from the transducers. The forward scattering effects detected in the C-scan is believed to be much higher than the effects for linear detectors. In practice, we assume that the propagation of primary ultrasound beams can be approximated by the parallel beam concept under this circumstance and the scattering effects is subjected to be reduced subsequently. Therefore, standard CT procedures are employed to reconstruct ultrasound cross-sectional images (see Figures 4-7A to D). The specific procedures are listed as follows:

1. Acquire C-scan images of the target in an 180° rotation.
2. Calculate the attenuation profile from the obtained image.
3. Extract linear attenuation information for all detector lines to obtain a sinogram.

4. Apply FBP to reconstruct one CT slice.

5. Repeat step 2 and 4 to cover slices.

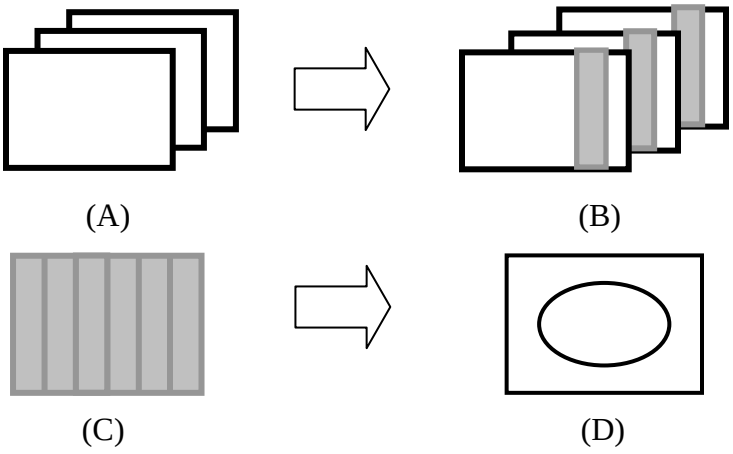

Figure 4-7. The flowchart of the ultrasound CT procedures: (A) Attenuation profiles calculated from C-scan images. (B) Extract linear information for one detector line from all images to form (C) a sinogram. (D) The reconstructed ultrasound CT result.

Base on the attenuation profiles, each vertical detector line of the sensor array is extracted to acquire a sinogram for the corresponding cross-sectional slice. A Sinogram is a visual representation of the attenuation information for reconstructing an ultrasound CT slice (see Figure 4-8). Since low noise is expected for a small test object, a standard filter will be applied (i.e., Ram-Lak filter) in the FBP processing[96]:

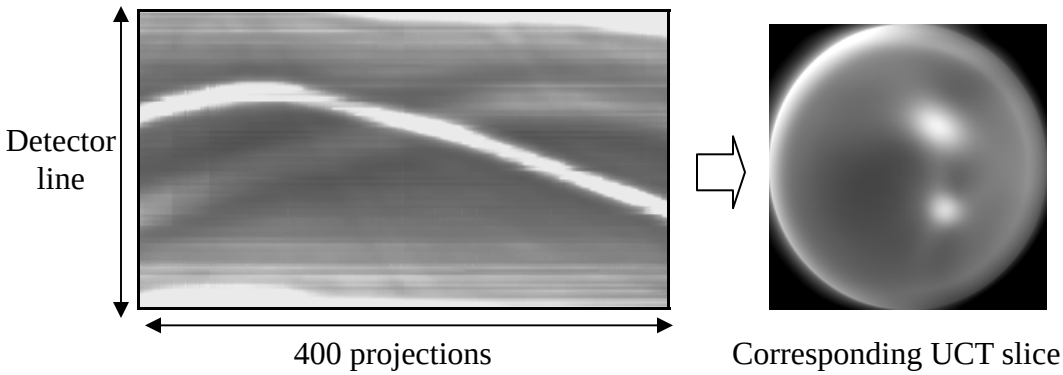

Figure 4-8. Example of a sinogram which associates with the reconstruction of the corresponding ultrasound CT slice. 400 projections were taken from 180 degree with each increment of 0.45 degree.

4.2 Ultrasound CT Studies using C-scan Prototype #1

4.2.1 System Configuration of the First Ultrasound CT Study

Ultrasound CT studies using the C-scan prototype #1 were performed by integrating a micro stepping motor to control the rotation of the test target. A total of 400 C-scan ultrasound images were acquired in a 180 degree rotation (0.45 degree per step). In each receiving line, the corresponding projection views were collected to form a sinogram for 400 images. The ultrasound CT results were then reconstructed using the filtered back-projection method based on the sinograms.

The detailed configuration of the ultrasound CT system is illustrated in Figure 4-9. The top of the water tank contained the controller of micro-stepping motor (Model MS-1 by Stepperworld - Los Angels, CA) and its power supply. Located towards the left side of the water tank, the sensing array was contained in a metal box and mounted with a compound acoustic lens. In the center, the target was directly connected to the stepping motor for rotation. The 5MHz ultrasound plane wave transducer was located on the lower right side of the water tank.

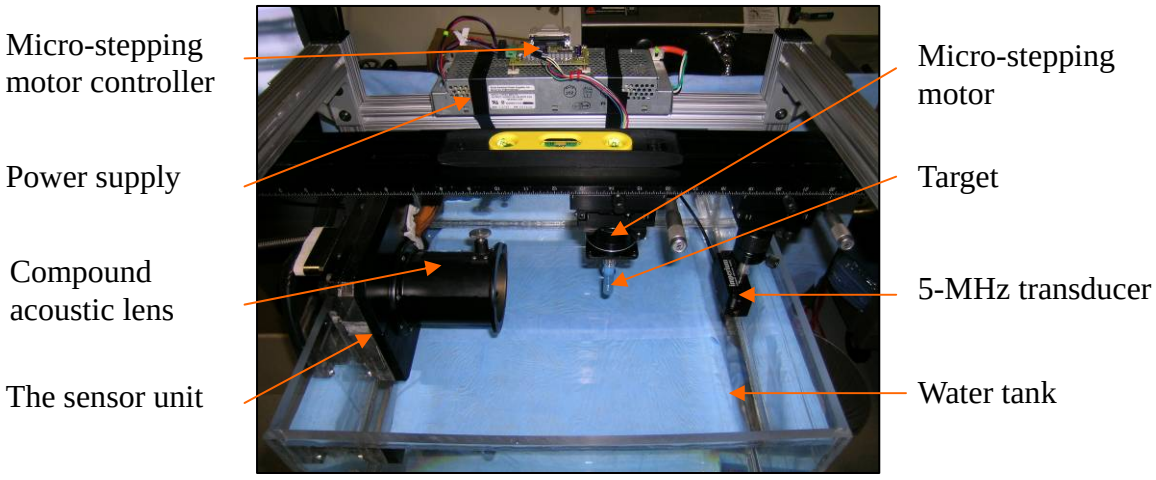

Figure 4-9. Closer view of the laboratory ultrasound CT system configuration with C-scan prototype #1.

4.2.2 Test Targets and C-scan Images

For the purpose of studying the possibility in generating ultrasound computed tomography images, two targets were frabricated for ultrasound CT experiments using silicone, plastic based pearl shape objects, plastic tubes and metal wires as shown in Figure 4-10A. The test targets were about 1.3cm in diameter and 5cm in length in cylinder shape. A 3mm pearl object was inserted in one phantom (see Figure 4-10B) while a 2mm pearl object and a wire of 0.6mm in diameter were inserted in the other phantom (see Figure 4-10C). The center section slice of test target No.1 and No.2 with their C-scan images are also displayed in Figures 7 (B)(C).

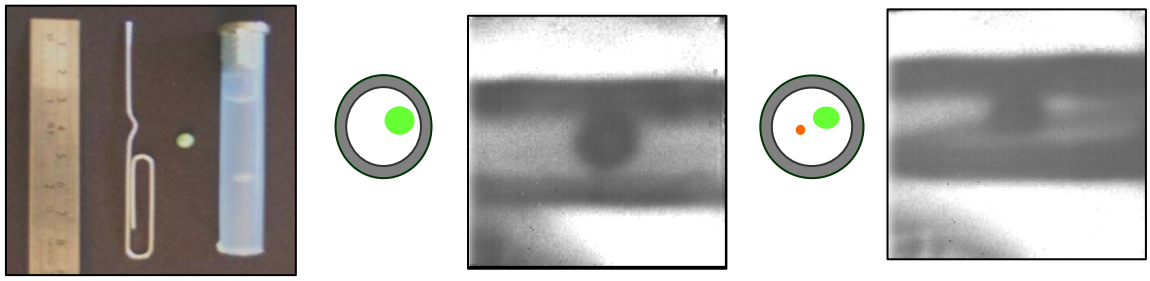

(A) (B) Test target No. 1 (C) Test target No. 2

Figure 4-10. (A) A photo picture of the test target and its contents. (B) The center cross section slice of test target No.1 in drawing and its C-scan ultrasound image at the initial viewing angle. (C) The center cross section of test target No.2 in drawing and its C-scan ultrasound image at the initial viewing angle.

4.2.3 Ultrasound Attenuation in C-scan Geometry

The fundamental assumption of ultrasound as it transmits through materials is that the ultrasound intensity is attenuated based on exponential decay along the propagation path. In this ultrasound CT phantom study, with the tube phantom made by the plastic wall and silicone, a “W” shaped attenuation profile in one-dimension was expected without considering other physical processes. As shown in Figure 4-11, ultrasound waves

passed through more plastic material and received higher attenuation at the edge of the tube than at the center section of the test target.

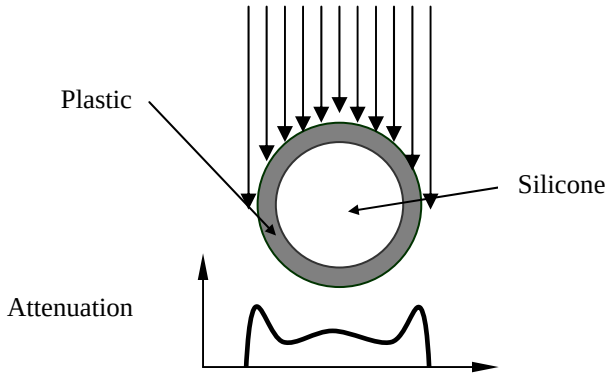

Figure 4-11. The attenuation profile of the test target with primary ultrasound.

4.2.4 Initial Ultrasound CT Images

The initial results for test targets No.1 and No.2 are shown in Figure 4-12 (A) and (B) respectively. Each ultrasound CT image represented a slice of the target in the position of the dash line on the C-scan image. The outer bright ring (the plastic tube) was clearly shown; however, the pearl shaped object was barely observable. The center part of the ultrasound CT image suffered a circular shadow effect and this effect is commonly encountered when a planar detector is employed [108, 109].

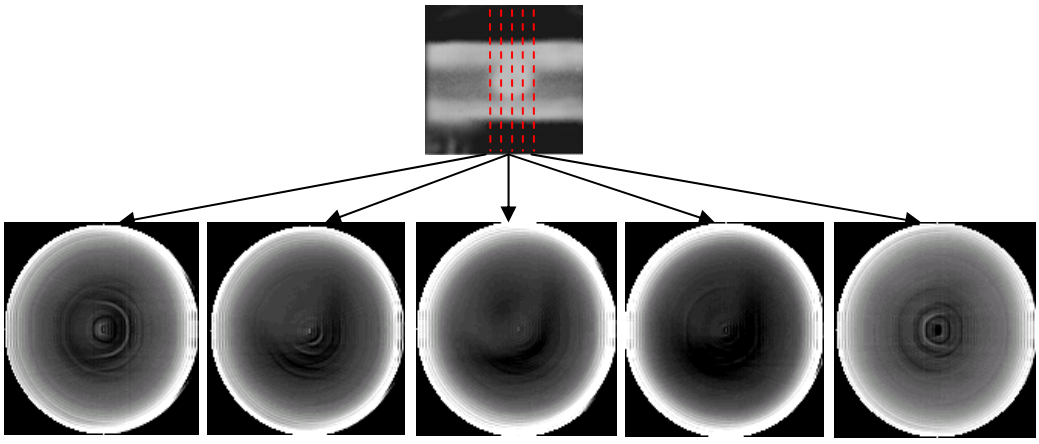

(A)

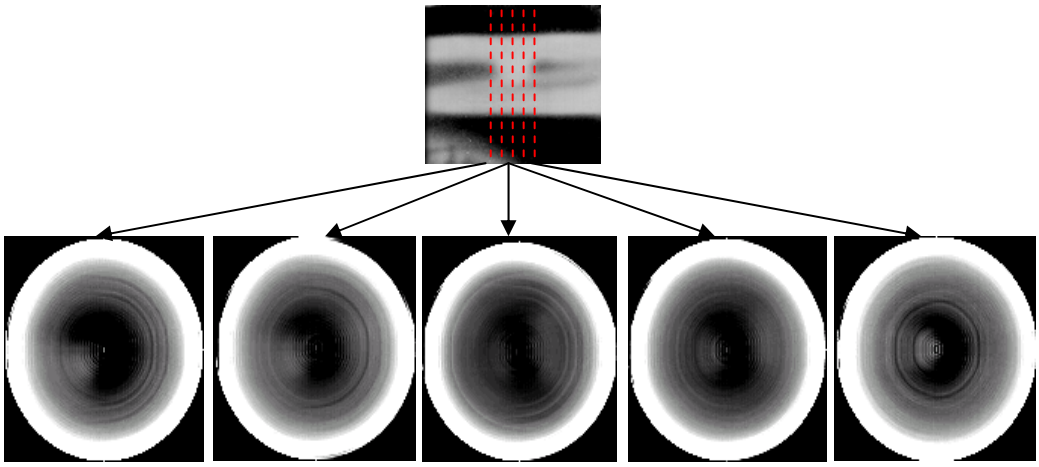

(B)

Figure 4-12. Initial reconstructed ultrasound CT results: (A) for test target No.1; (B) for test target No. 2. Each ultrasound CT image represents a slice of the target in the position of the dashed line on the C-scan image.

4.2.5 Circular Shadow and the Compensation Method

In order to reduce the shadowing effect, the shadow image was remodeled by generating a reference shadow frame without objects embedded in the silicone phantom. This process aimed to compensate for the basic attenuation distortion in the sinogram domain. Figure 4-13 (A) and (B) display the attenuation shadow frame and its inversed image respectively. Computer re-projection [110] was applied as shown in Figure 4-13 (C) to generate attenuation correction profiles for all 400 views.

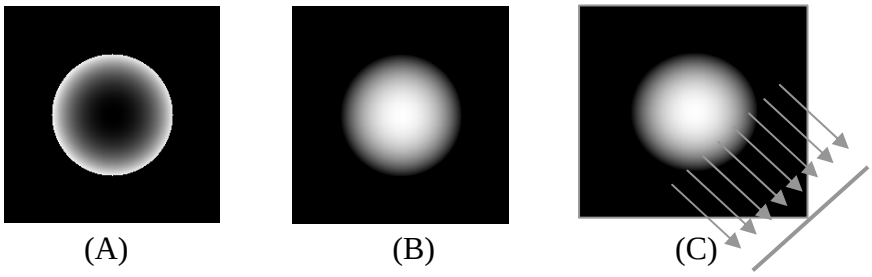

(A) (B) (C)

Figure 4-13. (A) The circular shadow model, (B) its inversed image, and (C) the computer reprojection method.

The inversed shadow profiles are defined as [110]:

$$p_s(t,\theta) = \int_{(t,\theta)} IS(x,y)ds \qquad (4.9)$$

where *IS(x,y)* is the inversed shadow, and "s" is the integration path that is perpendicular to the profile direction "t". The filtered back-projection reconstruction was then applied on the compensated attenuation profile as

$$f_c(x,y) = \frac{1}{4\pi^2}\int_{-\infty}^{\infty}\int_{-\infty}^{\infty} P_c(\omega)e^{j2\pi(x\sin\theta + y\cos\theta)}k(\omega)d\omega d\theta \qquad (4.10)$$

where $P_c(\omega) = DFT\{p_c(t,\theta)\}$ and $p_c(\theta,t) = p(\theta,t) + p_s(\theta,t)$. Note that the $p(\theta,t)$ contains negative values (attenuation coefficient) and therefore adding the computer-re-projection sinogram is actually a subtraction between each other. The reason of performing the shadow compensation processes in the sinogram domain is to avoid the arising noises may happen while directly applying the reduction method to each projection images.

4.2.6 Shadow-Compensated Ultrasound CT Results

After the computer produced re-projection for the intensity profile, the original sinogram was corrected using the re-projection sinogram. The FBP process for each corrected sinogram was then repeated. The shadow-compensated ultrasound CT reconstructed images are shown in Figure 4-14. By comparing the corresponding image sequences in the second rows of Figure 4-14 (A) and (B), the circular shadow effect was significantly reduced among all ultrasound CT images. In addition, the structures of the test objects inside the target (i.e., pearl shaped object and the wire) were significantly improved. As shown in Figure 4-14 (B), it was apparent that the wire on the left slices of the C-scan image appeared closer to the center while cutting the slices toward the right side of the C-scan image. Moreover, the pearl shaped object was correctly located on the right side of the cross section ultrasound CT image corresponding to the center C-scan image.

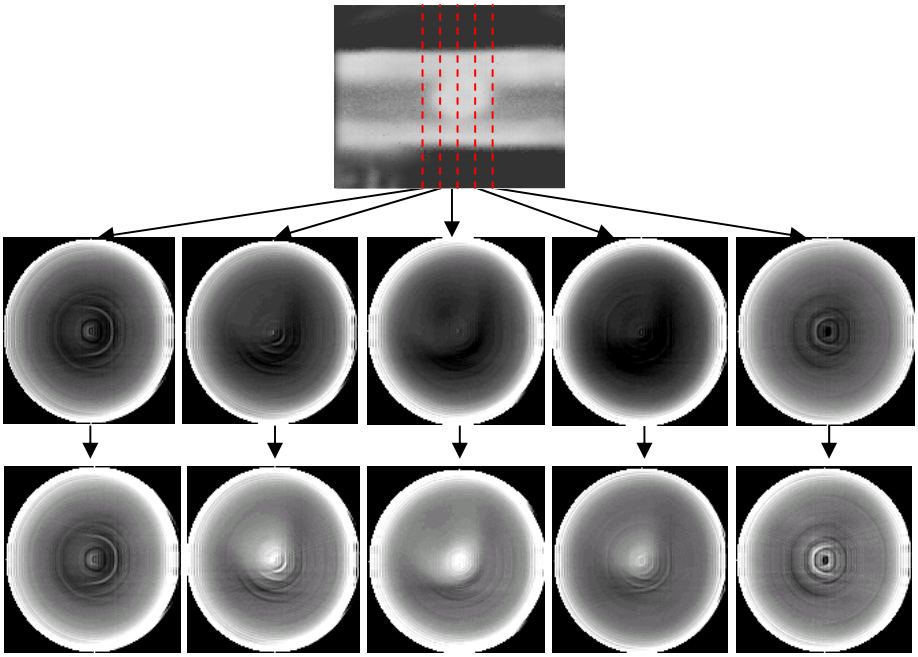

(A) The ultrasound CT reconstruction image sequence of test target No.1.

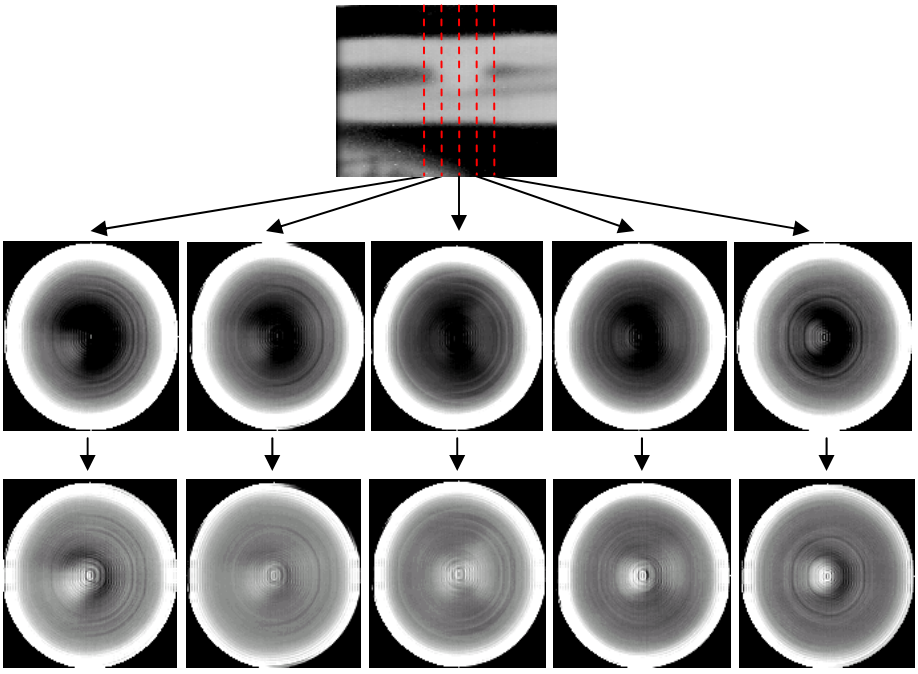

(B) The ultrasound CT reconstruction image sequence of test target No.2

Figure 4-14. Comparison of the initial results and the shadow-compensated images for the two targets. Each ultrasound CT image represents a slice of the target in the position of the dashed line on the C-scan image.

4.2.7 Analyses of Ultrasound CT Images

These ultrasound CT studies concluded that the PE-CMOS sensing array is capable of generating real-time and speckle-free C-scan ultrasound images. Due to the inconsistency of the center of rotation (off-axis rotation) during the ultrasound CT experiment, several ring artifacts appeared in the center of the ultrasound CT images. The ring artifacts may have been avoided if less than a sub-millimeter shift of the object was maintained. A more sophisticated rotating apparatus would be needed to achieve this system requirement. Figure 4-15 illustrates the diagram of the off-axis rotation in the first ultrasound CT investigation.

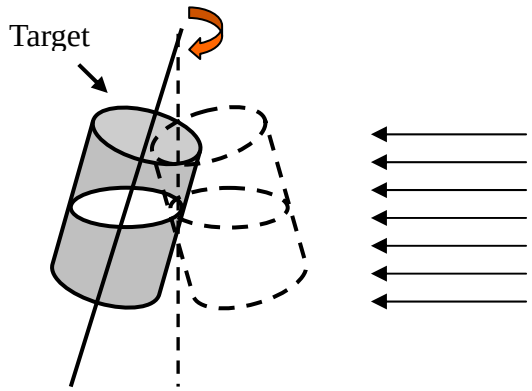

Figure 4-15. Diagram of the off-axis rotation problem.

Several potential artifacts were encountered as those experienced in x-ray CT system developments including cone beam CT systems [99]. Obvious artifacts during the first ultrasound CT study included (1) circular shadow due to scattering on the planar array, (2) ring artifact due to off-center rotation during the ultrasound CT rotation/projection scan, and (3) beam hardening effect due to the high attenuation of the object. The computer re-projection technique on the scattering model was successfully exercised to significantly overcome the circular shadow effect. The shadow compensated ultrasound CT images revealed the structures of small objects in the test target. Finally, in order to avoid ring artifacts in future studies, a more accurate rotating frame would be essential.

4.2.8 Additional Ultrasound CT Study – Animal Tissue Specimen

In order to further examine the ability of C-scan prototype #1 in obtaining ultrasound CT images of real tissue, a chicken finger was selected to be the imaging target for the ultrasound CT experiment. Due to the field-of-view limitations of the ultrasound imaging system, we used the joint portion of the chicken tissue sample that contained skin, muscle and bone structure in it. Figure 4-16 shows the picture of the test sample and its C-scan ultrasound image.

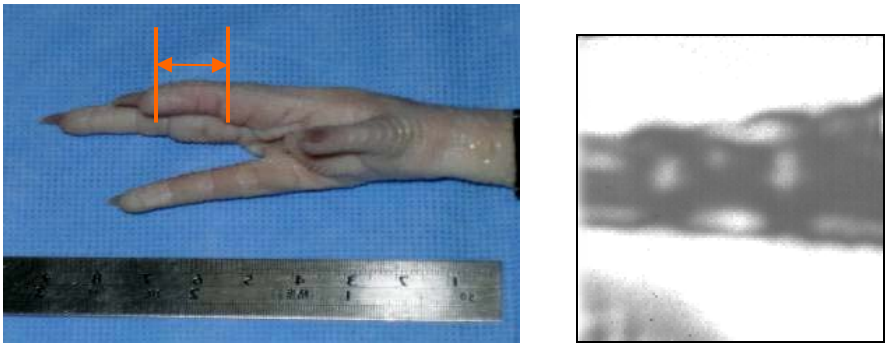

(A) (B)

Figure 4-16. (A) The test sample with marked portion was used in the experiment. The dimensions of the sample are ~2.5cm in length, ~0.6cm in diameter (tip of the chicken finger) and ~0.9cm in diameter (bottom of the sample). (B) The C-scan ultrasound image of the testing sample.

After the computer re-projection processing for the intensity profile, the original sinogram was compensated using the re-projection sinogram. Next, the FBP process was re-applied to each compensated sinogram. The compensated ultrasound CT reconstructed images are shown in Figure 4-17. Each ultrasound CT image represents a slice of the target in the position of the dashed lines on the ultrasound image. The dimensions of the CT image are 236 pixels × 236 pixels (2cm × 2cm). There are two circular contours in each ultrasound CT images: the outer contour represents the cross-sectional shape of the chicken sample; and the inner contour represents the bone structure of the chicken sample.

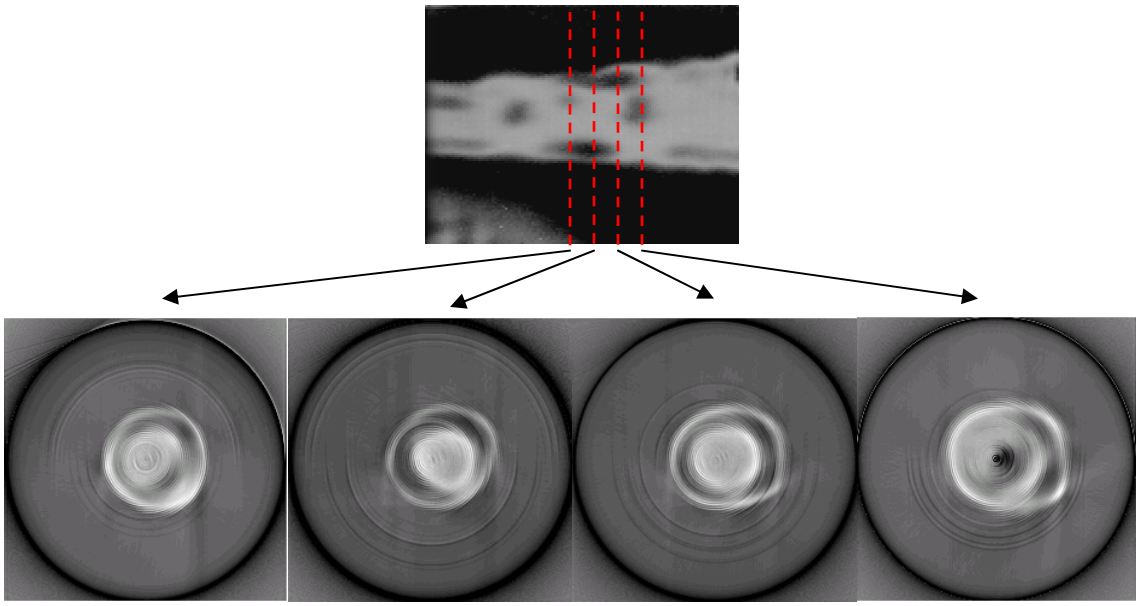

Figure 4-17. Reconstructed ultrasound CT images. Each ultrasound CT image represents a slice of the target in the position of the dashed line on the C-scan image.

4.3 Ultrasound CT Studies using C-scan prototype #2

4.3.1 System Configuration of the Second Ultrasound CT Study

In general, there are two typical CT scanning configurations: the first type is where the transducer-receiver units are stationary during the scan while the target rotates; the other type is where the target is stationary while the transducer-receiver units rotate during the scan. Initial ultrasound CT studies (refer to Section 4.2) indicated that the first CT scanning configuration was difficult to achieve stationary when the accurate system standard was not reached. However, encouraged by initial ultrasound CT studies with prototype #1 and the improved imaging performance of the I-400 PE-CMOS sensor array, a new ultrasound CT system was developed with the integration of a high torque stepping motor and the C-scan prototype #2. Major improvements of the new system included mounting the target on the main frame of the bridge and rotating the water tank which contained the transducer and receiving units around the target.

A picture of the new ultrasound CT study's system configuration is diagramed in Figure 4-18. The plane wave ultrasound transducer was placed inside the water container. The receiving unit, the acoustic lens system, and the I-400 PE-CMOS sensor array were mounted on the side of the container. The testing target was hung on the top main frame of the bridge. The concept of the design was to build a rotating water container driven by a micro-stepping motor (Model MD2, Arrick Robotics, TX) underneath in order to generate 180 degree C-scan images around a testing target. The steady scanning plane between the transducer and the receiving unit was maintained to overcome the off-axis rotation problem encountered in the first ultrasound CT study using C-scan prototype #1. Figure 4-19 illustrates the diagram of the new scanning geometry when the imaging target is placed at a tilt angle.

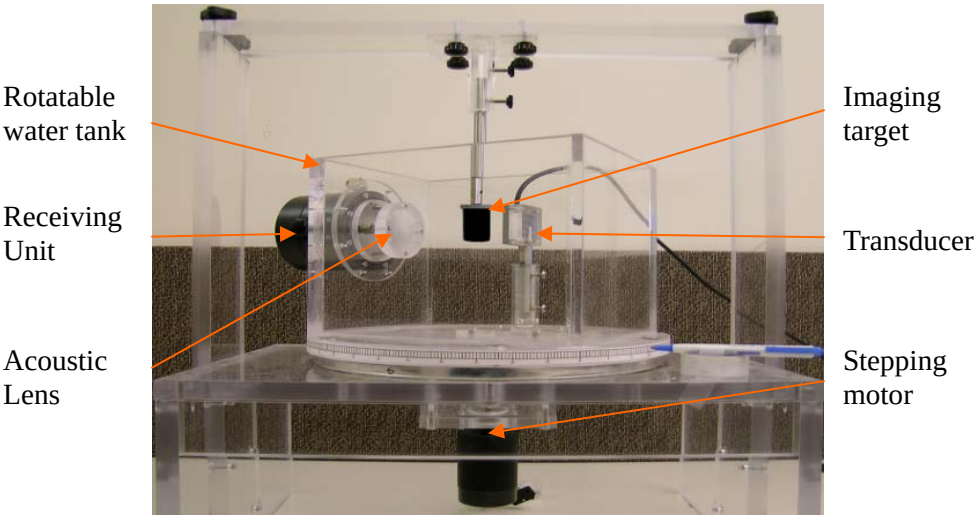

Figure 4-18. A picture of the new portable ultrasound CT system's configuration.

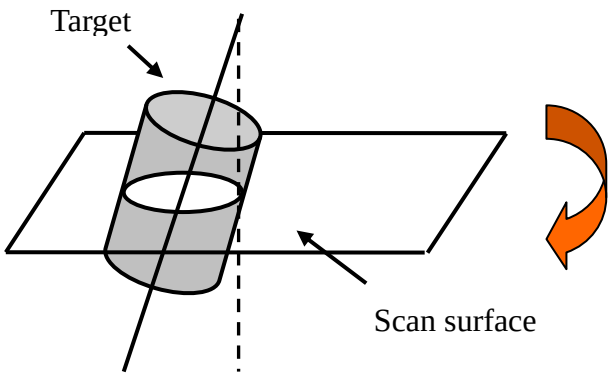

Figure 4-19. A skeleton diagram of the new scanning geometry.

4.3.2 Targets and C-scan Images

New imaging phantoms were fabricated for the ultrasound CT experiment using agar gel, plastic based pearl shape objects, plastic tubes (film containers) and a metal wire as shown in Figure 4-20. Agar powder was selected to replace the silicone-base used in the previous ultrasound CT study. The test phantoms were approximately 3cm in diameter and 5cm in length with a cylinder shape in film containers. Same type of the plastic-based pearl shape objects which were used in the first ultrasound CT study (refer to Section 4.2.2) were inserted in one phantom while a 2.5mm object and a same kind of wire with 0.9mm in diameter was inserted in the other phantom. The center section slice of test phantom No.1 and No.2 with their C-scan images are displayed in Figure 4-21 (A) and (B). The dimensions of each C-scan images were 200 pixels by 200 pixels. Note that in test phantom No.1, an air pocket was found within the pearl shape object; moreover, an air bubble was trapped while pouring the agar solution into the container, as illustrated on the C-scan image in Figure 4-21 (A).

Figure 4-20. Materials which were used to fabricate test phantoms.

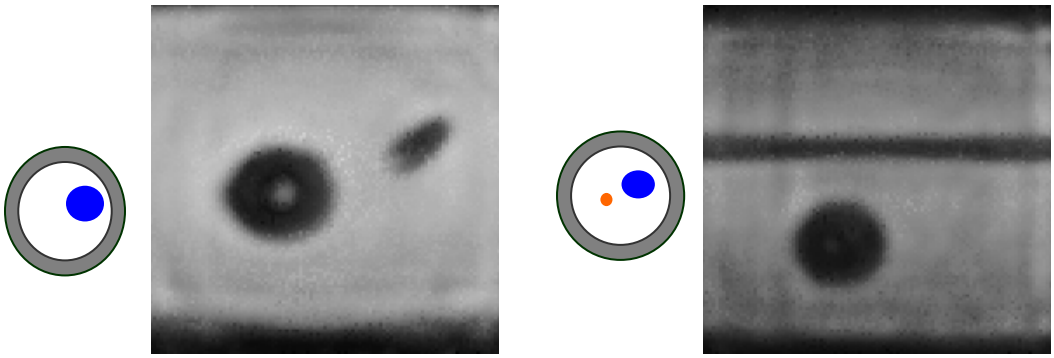

(A) (B)

Figure 4-21. (A) The center cross-sectional diagram of phantom No.1 and its C-scan ultrasound image at the initial viewing angle. Notice that the small black area on the right of the image is an air bubble. (B) The center cross-sectional diagram of phantom No.2 and its C-scan ultrasound image at the initial viewing angle.

4.3.3 Ultrasound CT Phantom Images

A total of 400 C-scan images of each phantom were acquired by rotating the water tank with 0.45 degree increments covering 180 degrees around the phantom. Followed by the same ultrasound CT procedures described in Section 4.2.2, reconstructed ultrasound CT images of test phantoms No.1 and No.2 were obtained using the FBP method. Figure

4-22 illustrates reconstructed ultrasound CT images of two test phantoms and each ultrasound CT image represents a slice of the target in the position of the dashed lines on the intensity-inversed C-scan images. The corresponding reconstructed ultrasound CT images obtained from the “scattering-corrected” C-scan images are displayed at the second rows in Figure 4-22.

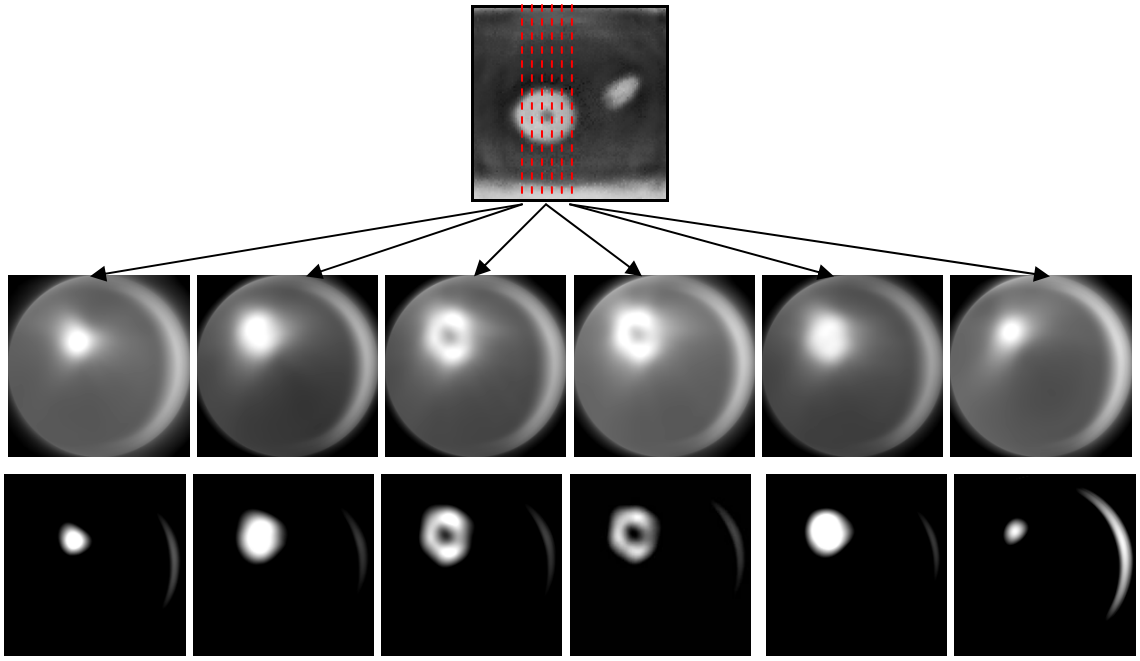

(A)

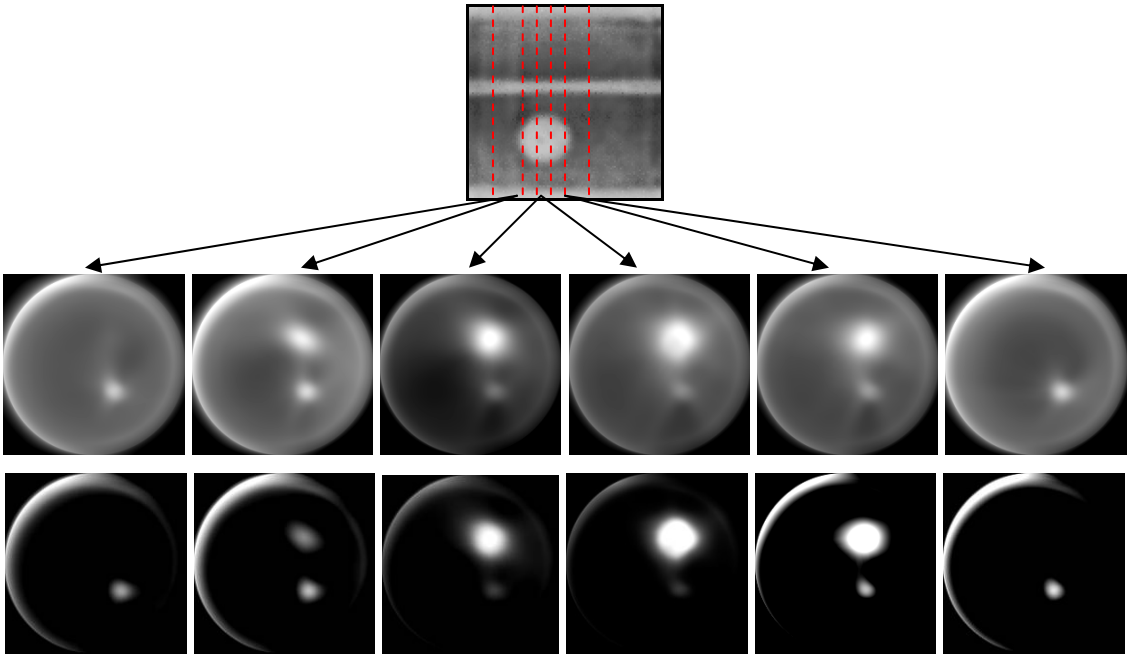

(B)

Figure 4-22. Original reconstructed and “scattering-corrected” ultrasound CT images of test phantoms: (A) test phantom No.1; (B) for test phantom No. 2. Each ultrasound CT image represents a slice of the target in the position of the dashed line on the C-scan images.

4.3.4 Analyses of Ultrasound CT Images

By replacing the silicone-based target used in the first ultrasound CT study with an agar-based phantom, the circular shadow effect was significantly reduced. The “W” shaped attenuation profile mentioned in Section 4.2.3 was no longer suitable for describing the new phantoms due to the fact that silicone gel had much higher acoustic impedance than the agar-based material. Therefore, the shadow compensation method, the computer re-projection model, was not applied for the reconstruction of the ultrasound CT images as illustrated in Figure 4-22.

With the accurate system design of the ultrasound CT experiment using C-scan prototype #2, the ring artifact was not observed in the reconstructed ultrasound CT images. The off-axis rotation problem encountered in the first ultrasound CT study using C-scan prototype #1 was also resolved. Other artifacts caused by inactive pixels were eliminated by using the I-400 sensor array. The reconstructed ultrasound CT images had improved image quality than the previous results. Furthermore, reconstructed ultrasound CT images from the “scattering-corrected” C-scan images showed better contours of the object as compared with the unprocessed images.

4.3.5 Potential 3-D Ultrasound Images

In order to investigate the potential of generating 3-D ultrasound image, the reconstructed ultrasound CT images of phantom No.1 and No.2 were processed by a commercially available 3-D viewing software program *Volview 2.0*. Direct volume rendering of maximum intensity function was selected to obtain raw ultrasound 3-D models without any smooth filtering processing.

A complete ultrasound CT image set of each phantom contained 200 raw slices with 16 bits of image depths. 3-D ultrasound images of each phantom with volume dimensions of 200 × 200 × 200 pixels were acquired and a conventional window and leveling operation was performed for the purpose of displaying 3-D images. Figure 4-22 and 4-23 illustrate the alternate views of the 3-D ultrasound images of test phantom No.1 and No.2 respectively. In Figure 4-23, the 3-D ultrasound raw images displayed not only the pearl shaped objects but also the small air bubble contained in the phantom; moreover, after applying the scattering correction method, the air pocket within the center of the pearl was revealed. As for Figure 4-24, both of the pearl shape object and the metal wire embedded in phantom No.2 were observable; and the 3-D images based on the scattering-corrected images illustrated significantly improved results as compared with their raw images.

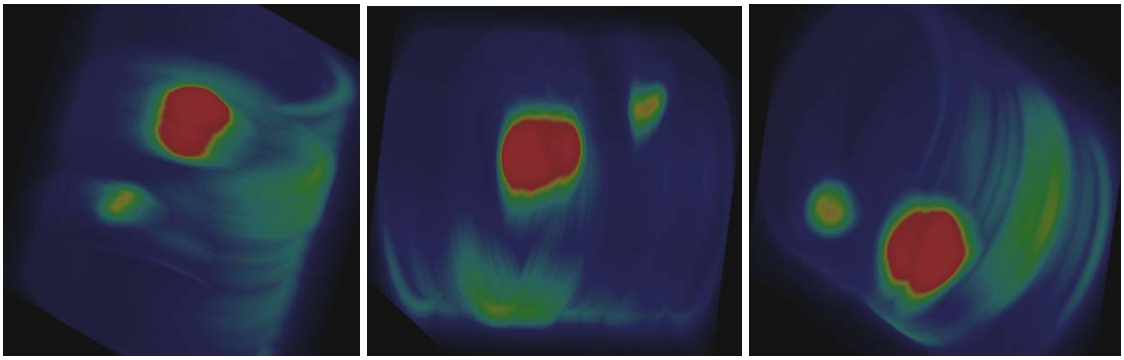

(A) Generated by original ultrasound CT images.

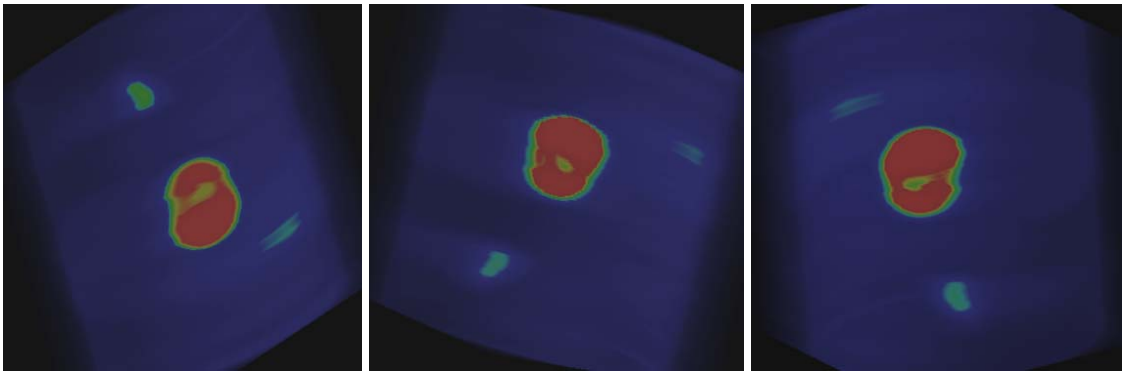

(B) Generated by “scattering-corrected” ultrasound CT images.

Figure 4-23. Alternate views for the 3-D ultrasound image of the test phantom No.1. (A) Generated from original ultrasound CT images and (B) from “scattering-corrected” ultrasound CT images.

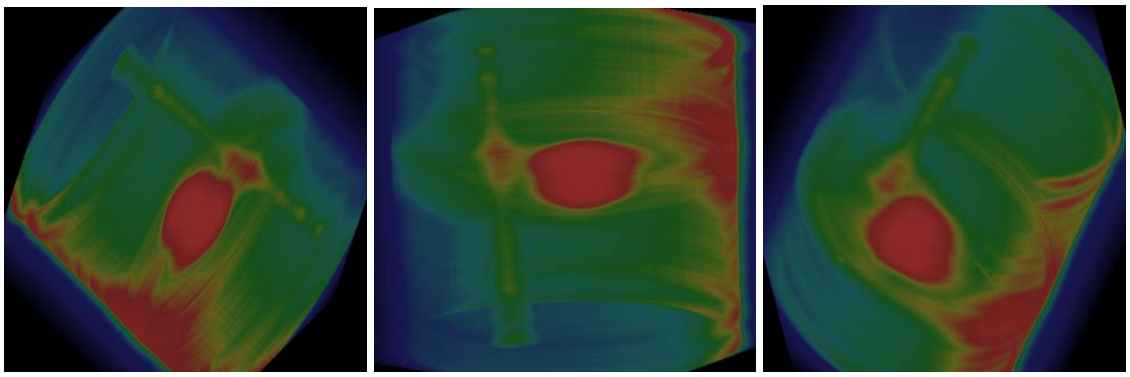

(A) Generated by original ultrasound CT images.

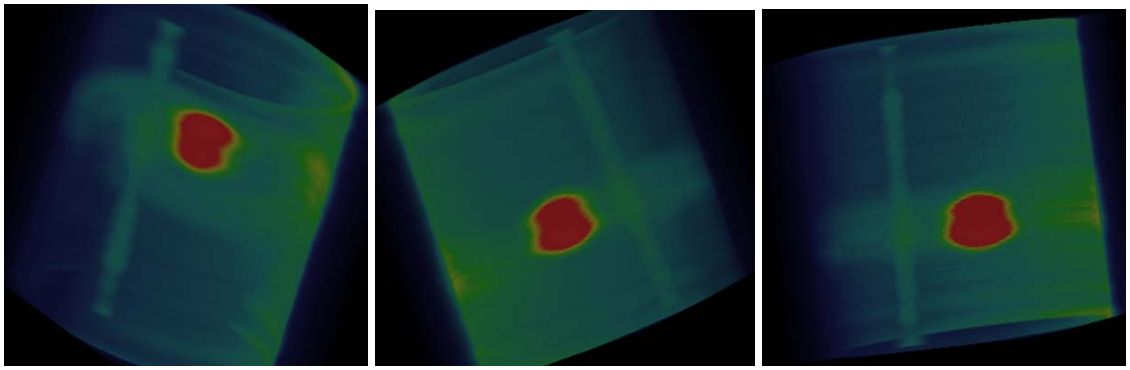

(B) Generated by “scattering-corrected” ultrasound CT images.

Figure 4-24. Alternate views for the 3-D ultrasound model of phantom No.2. (A) Generated from original ultrasound CT images and (B) from “scattering-corrected” ultrasound CT images.

4.4 Summary

In this chapter, we described the design of an ultrasound CT system, reconstruction methods for planar beam source, a shadow compensation method specifically applicable to planar beam CT image and demonstration of the ultrasound CT images. The shadow compensation method developed here is also applicable to cone beam CT, which is a current research and development topic in the field of CT. Based on the essential information obtained from the first preliminary ultrasound CT studies performed by the C-scan prototype #1, modifications were made to build the second prototype to overcome several drawbacks. A more accurate system design and new scanning geometry were integrated into the C-scan prototype #2 to reduce artifacts found

previously. The study results indicated that the second prototype could produce CT images with more details and fewer artifacts than the CT images acquired by the first prototype.

It is concluded that the ultrasound C-scan prototype #2 had the potential of generating 3-D ultrasound raw images although artifacts were observable especially around the edges of the cylinder volume and the layers contained the pearl shaped objects. However, after applying the proposed scattering reduction method described in Chapter 3, the reprocessed 3-D images were significantly improved as compared with their raw 3-D images. There are many advanced 3-D rendering techniques and a variety of interpolation methods or smooth filters available to further enhance the 3-D display. Therefore, superior 3-D ultrasound image is expected to be generated by the proposed C-scan prototype #2 equipping with a PE-CMOS sensor array.

Chapter 5

New Sensor Capabilities and Potential Medical Applications

5.1 Needle Biopsy Simulation using C-scan Prototype #1

The use of ultrasound in image-guided needle biopsy has been hindered by the physics of pulse echo ultrasound[111, 112]. In the use of conventional pulse echo ultrasound for breast biopsy, the needle must be kept in a perpendicular orientation to the ultrasound transducer. The C-scan systems provides excellent orientation in the x and y directions, but, in its initial configuration, does not give much information about the z-direction.

The C-scan prototype #1 was tested for potential applications using breast phantoms. Breast phantoms containing simulated breast abnormalities including tumors and cysts were utilized during investigative tests performed on the first C-scan prototype with I-100 sensor array. Each image was extracted from a single frame (1/30 second) of the sequential images without post-processing.

The biopsy simulation was performed by placing a CIRS breast phantom (Model 52) between the transducer and receiver of the first C-scan prototype. The camera (detecting unit) was set to focus on the area with two small simulated masses contained in the breast phantom. The breast phantom was 8 cm thick. A biopsy needle was placed at about 4 cm below the phantom's surface. The biopsy needle first punctured the target, was then removed, and then was used to puncture the target again. C-scan ultrasound images were also captured while the needle orientation was rotated clockwise. This procedure, however, pushed the right upper corner of the mass out of the focal plane. Figures 5-1 (A) to (F) display a sequence of needle biopsy images using a CIRS phantom with the C-scan prototype #1. These images were sampled from a sequence of 150 ultrasound images taken at a speed of 30 frames per second for a period of five seconds with the CIRS breast phantom.

A 2cm tumor contained in the same phantom was used as a model in the second part of the experiment. Figure 5-2 (A) to (E) demonstrates several focal plane fields of the same details obtained when focused from the edge into the center of the simulated lesion. Each image contained a black boundary representing the region outside of the field of view from the transducer disk. The lighter grey areas within the boundary represented the background material of the phantom which surrounded the spherical details. The black linear streaks were the needle tracks. The white streaks were believed to be areas of leakage of the material from the spherical objects.

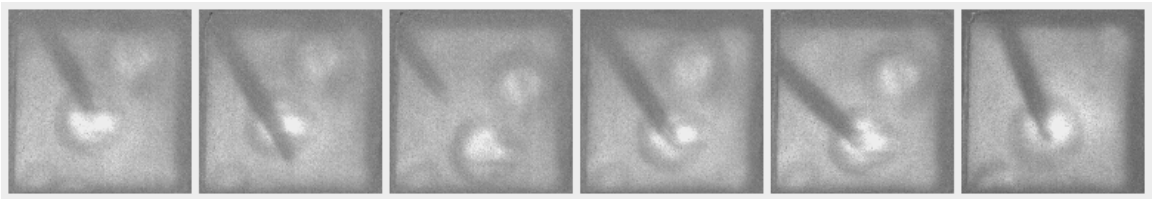

(A) (B) (C) (D) (E) (F)

Figure 5-1. Ultrasound images of the biopsy simulation. The needle first punctured the target (A) and (B), then removed (C), and punctured the target again (D) and (E). The needle was rotated clockwise from (E) to (F). This operation pushed the mass on the right upper corner out of the focal plane.

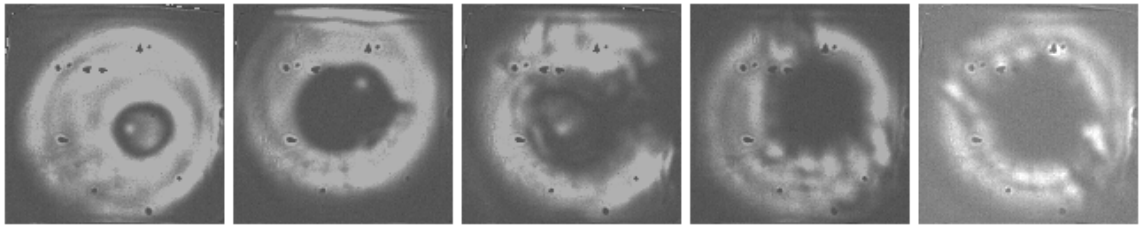

(A) (B) (C) (D) (E)

Figure 5-2. These images are of a specific detail of simulated tumors in the CIRS breast phantom Model 52 designed for tissue equivalent ultrasound needle biopsy training. The imaged detail is a spherical echogenic object simulating solid tumor within the phantom. The detail has been punctured multiple times under ultrasound guidance leaving multiple needle tracks.

5.2 Foreign Object in Soft-tissue Study (C-scan Prototype #2)

Penetrating trauma with retained foreign matter is commonly seen in medical emergency departments, in battlefield casualties, and in industrial accidents. The inability to detect and remove foreign objects may lead to serious infection, inflammation or other complications. For injured patients, identification and localization of foreign objects are essential to facilitate the removal and treatment. Imaging modalities such as conventional radiography[113] and B-scan ultrasound[114-116] are commonly used for detecting the location, size and shape of the foreign object. Radiologist then identifies a foreign object by distinguishing its different radiodensity (or echo pattern in B-scan ultrasound) from that of the surrounding normal tissue. Once identified, localization for removal remains challenging; radiographs are usually done in a separate facility, limiting interactive wound cleaning and imaging; conventional ultrasound images require that the foreign matter presents a surface perpendicular to the ultrasonic beam.

Based on our preliminary studies described in Section 5.1, C-scan ultrasound imaging potentially has the advantage for identifying, localizing and allowing continuous imaging as wounds are treated. Instead of repeating angular shift of the transducer as is done with B-scan ultrasound to find the reflection signal, C-scan ultrasound provides the

steadily scanning capability without moving the transducer. Moreover, the varying pressure applied with B-mode transducer may cause foreign object to shift location which is less of an issue with C-scan.

In the study shown here, we compared the capability of the C-scan prototype #2 with three conventional imaging modalities in their capability of detecting foreign objects contained in soft tissue. Foreign objects, made of varying materials including bamboo, plastics, glass, and aluminum alloys, were inserted into a slab of pork with skin, fat, and muscle tissues. Each object was individually inserted into the skin, passed through the fat layer, and penetrated into the muscle layer of the porcine tissue sample. Images of the porcine tissue sample were taken using the C-scan prototype #2, a portable B-scan ultrasound, a film-based radiography, and a computerized radiography (CR). We then computed the contrast-to-noise ratio (CNR) for each object in the soft tissue to evaluate the performance of the C-scan prototype #2 against other imaging modalities.

5.2.1 Design of the Study

In this comparative study, four imaging modalities were used to evaluate their ability to detect foreign objects in soft tissue. The selected porcine tissue sample was a slab of pork consisting of skin, fat, and muscle layers (Figure 5-3). The dimensions of the sample are ~10cm (L) × ~5cm (W) × ~2.5cm (H). The average sound speed for the porcine soft tissue is close to water: skin (~1500m/s), fat (~1430m/s), and muscle (~1580m/s)[117]. Their corresponding attenuation coefficients are: skin (2-4 $dB \cdot cm^{-1} \cdot MHz^{-1}$), fat (0.8 $dB \cdot cm^{-1} \cdot MHz^{-1}$ z) and muscle (0.5-1.5 $dB \cdot cm^{-1} \cdot MHz^{-1}$) [24].

To better simulate injured soft tissue due to forceful penetration, seven foreign objects were inserted into the porcine soft tissue sample from the skin through the fat tissue, into the muscle layer. The insertion process was conducted in a container of water to prevent air bubbles. Figure 5-4 illustrates the seven foreign objects employed in the experiment including one bamboo object, three kinds of plastic objects, one glass object

and two aluminum alloy objects with different shapes and sizes. Object No.1 is a bamboo skewer. Plastic objects No.2, No.3 and No.7 are made of heavy-weight polystyrene, nylon and extra heavy-weight polystyrene, respectively. The glass object (No.6) is obtained from a broken light bulb. Metal objects are made of aluminum alloys of 5182 (No.4) and 3104 (No.5) series. The thicknesses of these objects vary from 0.01 cm to 0.25 cm. Dimensions of these objects and their corresponding acoustic properties are listed in Table 5-1. Note that objects with unknown attenuation information were computed by the average intensity loss between their individual C-scan image and the initial image acquired without target (i.e. water only).

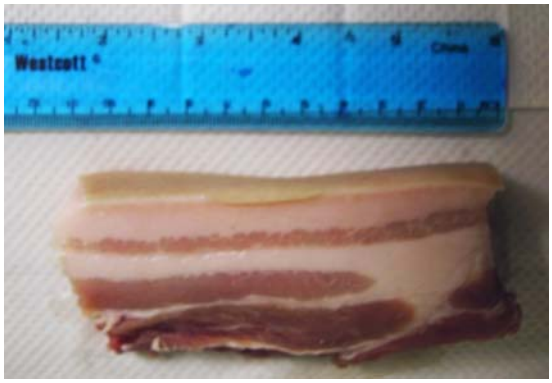

Figure 5-3. The soft-tissue sample composed of skin, fat, and muscle tissues.

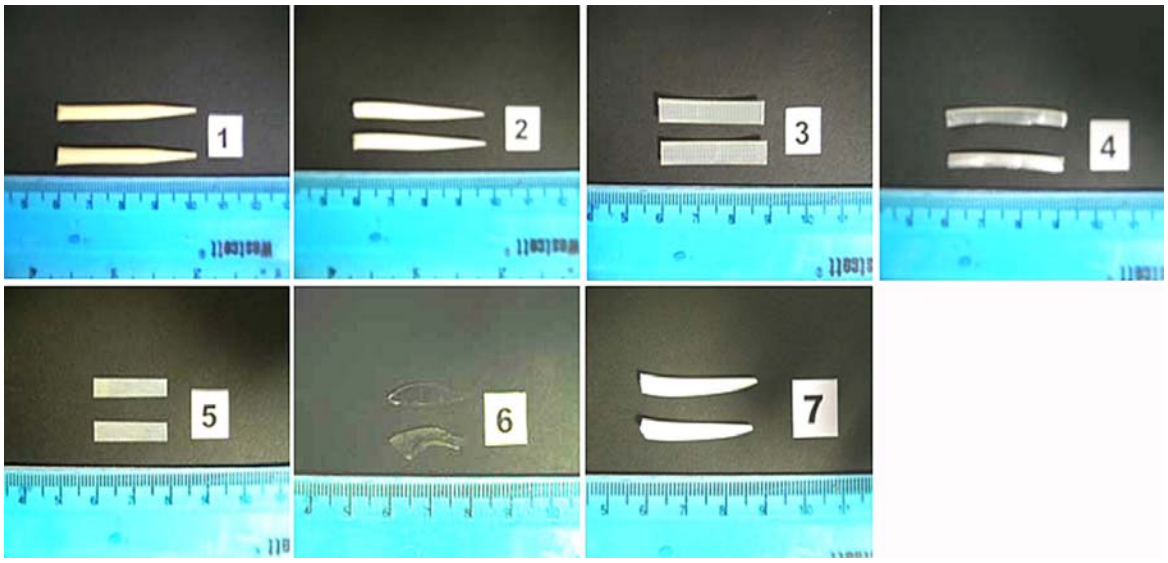

Figure 5-4. The foreign objects used in the experiment: objects of No.1 are bamboo skewers; Nos. 2, 3, and 7 are plastic sticks; Nos. 4 and 5 are aluminum alloys; No.6 are pieces of glass. Note that only one object in each category was selected.

Table 5-1. Parameters and acoustic properties of test objects

Object	**No.1**	**No.2**	**No.3**	**No.4**	**No.5**	**No.6**	**No.7**
Material	bamboo	heavy-weight polystyrene	nylon	aluminum alloy-5182	aluminum alloy-3104	glass	extra heavy-weight polystyrene
Thickness (cm)	0.25	0.15	0.1	0.1	0.01	0.1	0.2
Length (cm)	4	4	3	3	2	2	2.5
Width (cm)	0.2	0.15	0.3	0.2	0.3	0.2	0.25
Density[a] (g/cm^3)	0.9	1.05	1.12	2.65	2.72	2.2	1.04
Average Sound Speed[1] (m/s)	5600	2400	2600	6500	6320	5900	2320
Attenuation[1] (dB/cm @ 5MHz)	19.0[2,3]	1.8	2.9	14.2[2]	14.1[2]	12.5[2]	3.6

[1] From Selfridge[118] and Wegst[119]

[2] Experimental data computed by using the C-scan prototype #2

[3] Approximate value with air contained inside its fibrotic structure

The same porcine soft tissue sample, containing the foreign objects, was imaged by the C-scan ultrasound prototype #2 operated at 5MHz and three other imaging modalities including a portable B-scan ultrasound imaging system (Terason Ultrasound System with curved linear 4C2 wideband 128 elements probe operated at 4MHz), a film-based radiography system operated at 44kVP, and a CR system operated at 40kVP. All images were obtained using a perpendicular viewing orientation in order to cover most of the foreign objects in the same view (Figure 5-5).

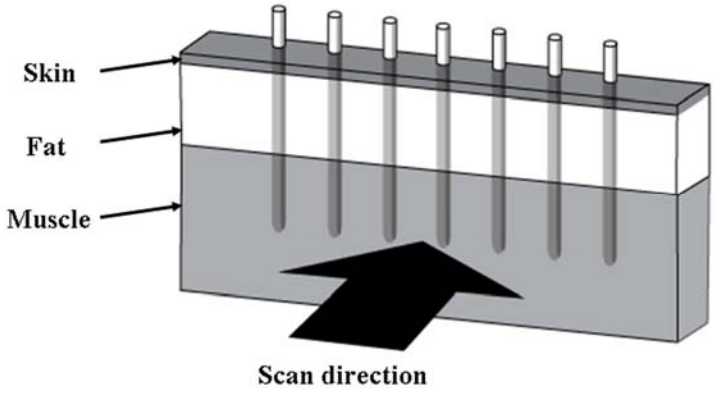

Figure 5-5. The source emitting direction for all image modalities was perpendicular to the inserting direction.

5.2.2 The C-scan Images

In this experiment, a 5MHz transducer was employed to acquire ultrasound images of the porcine tissue sample using the C-scan prototype #2. Figure 5-6 shows a series of the C-scan images with each centered at a foreign object. The C-scan images revealed that most of foreign objects were observable. In addition, the structural features of fat and muscle tissues were clearly captured in the C-scan images.

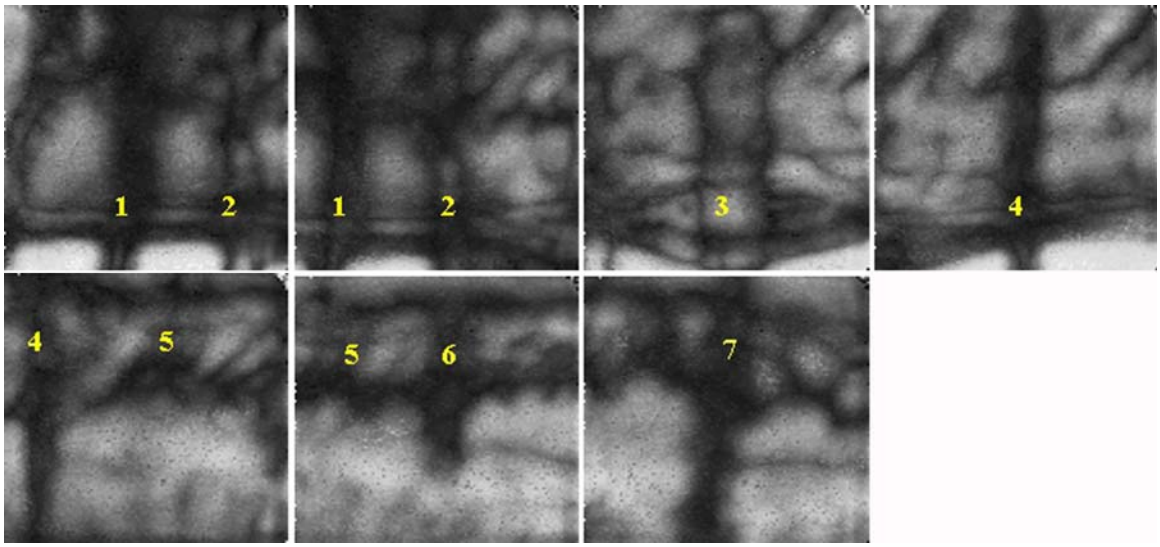

Figure 5-6. A series of C-scan images for the foreign objects contained in the porcine tissue sample. The bold numbers indicate the specific foreign object according to Table 5-1.

In order to view the C-scan image of the whole area containing the foreign objects, standard image stitching processes were performed to combine these C-scan images (Figure 5-7). The stitched C-scan image facilitates visual comparisons with the images obtained from other modalities.

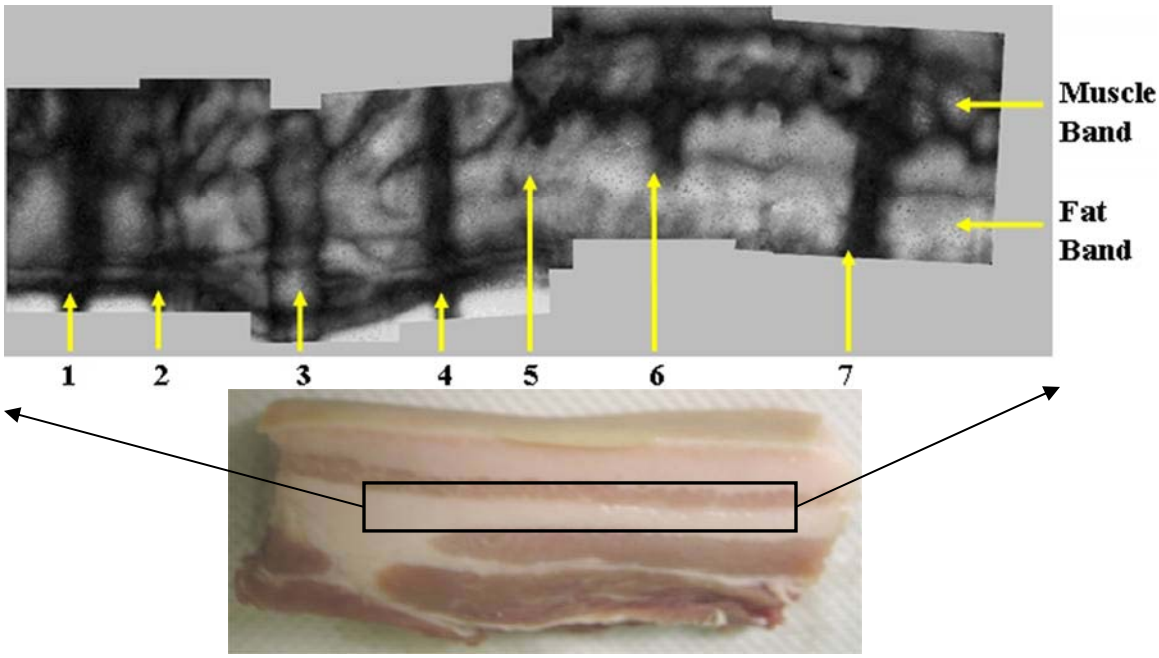

Figure 5-7. The stitched C-scan image of the porcine sample and foreign objects (above). The image reveals a section of the porcine sample (below). The arrows 1 to 7 point to the locations of the foreign objects inserted in the pork. The arrow numbering corresponds to the particular foreign objects as listed in Table 5-1.

5.2.3 The B-Scan Ultrasound Images

The same pork sample was also imaged by a portable B-Scan ultrasound system, the Terason®, with Curved Linear 4C2 Wideband 128 Element probe at 4MHz. The B-scan ultrasound images were acquired by attaching the probe to the side of the pork sample. Due to the strict requirement of pulse-echo orientations in operating the probe scanner; multiple images were captured in order to view all foreign objects in the pork sample. In the B-scan images which are illustrated in Figure 5-8, the bamboo skewer, plastic objects, and the glass piece are observable; however, edges of objects are not sharp due to speckle artifacts. The metal object (No.5) is only apparent in one of the B-scan images due to its tilt orientation.

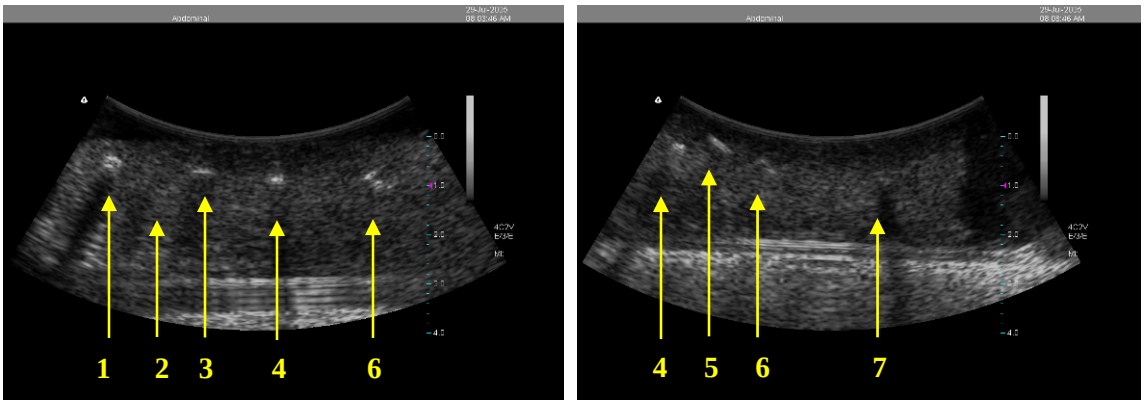

Figure 5-8. The B-scan ultrasound images of the porcine tissue with foreign objects. The arrows point to the locations of the foreign objects inserted in the porcine tissue. The numbers indicate the foreign objects and correspond to Table 5-1.

5.2.4 The Film-based Radiograph and CR Images

The same porcine tissue sample was then imaged by two radiography systems. Figure 5-9A illustrates the film-based radiograph of the porcine tissue obtained at 44kVP and Figure 5-9B shows the CR image obtained at 40kVP. The thicker metal piece and the glass piece are the most visible in both the radiographs. For the aluminum alloy pieces (Nos. 4 and 5), the CR image shows better contour than the film-based radiograph. The bamboo skewer and plastic sticks are barely observable in either the film-based radiographs or CR images except the portions outside of the porcine tissue sample that are surrounded by air.

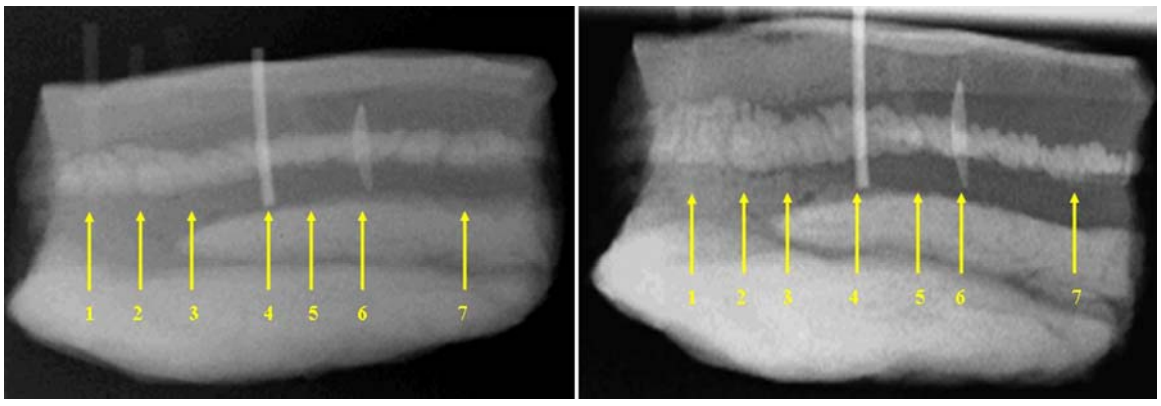

(A) (B)

Figure 5-9. (A) The film-based radiograph obtained at 44kVP. (B) The CR image obtained at 40kVP. The arrows point to the locations of the foreign objects inserted in the porcine tissue. The numbers indicate the foreign objects corresponding to Table 5-1.

5.2.5 Visual Comparisons of the C-scan Images and the X-ray Images

Although C-scan ultrasound and radiography systems use similar imaging geometries, their intensity representations are different. The foreign objects are represented with higher grey levels (brighter) in the radiographs rather than the lower grey levels (darker) in the C-scan images. For better visual comparison, we inverted the intensity of the C-scan images and placed them above the radiographs. Figure 5-10A shows the intensity inverted C-scan image and the film-based radiograph; Figure 5-10B shows the intensity inverted C-scan image and the CR image. The arrows connected to each number point out the same object in both images. The comparison images illustrate that both the bamboo skewer and plastic objects in the C-scan images are more conspicuous than those in the radiographs.

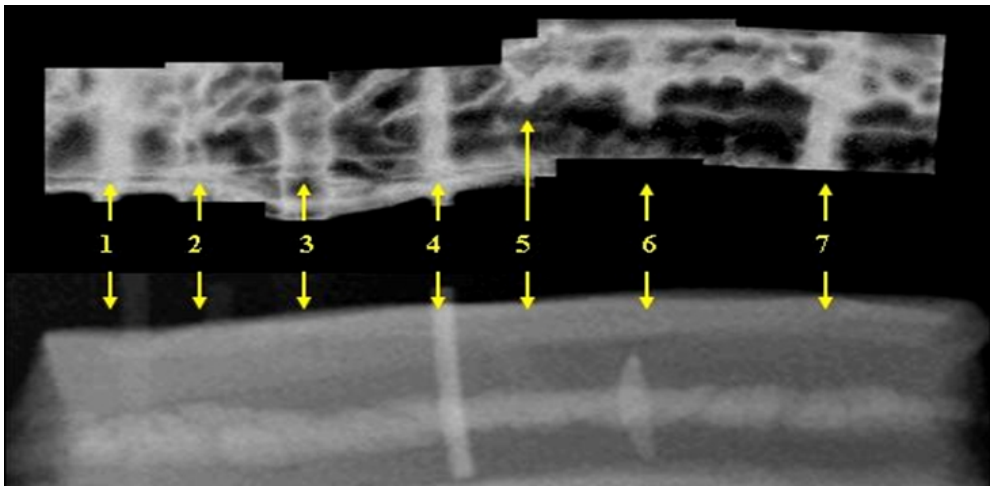

(A)

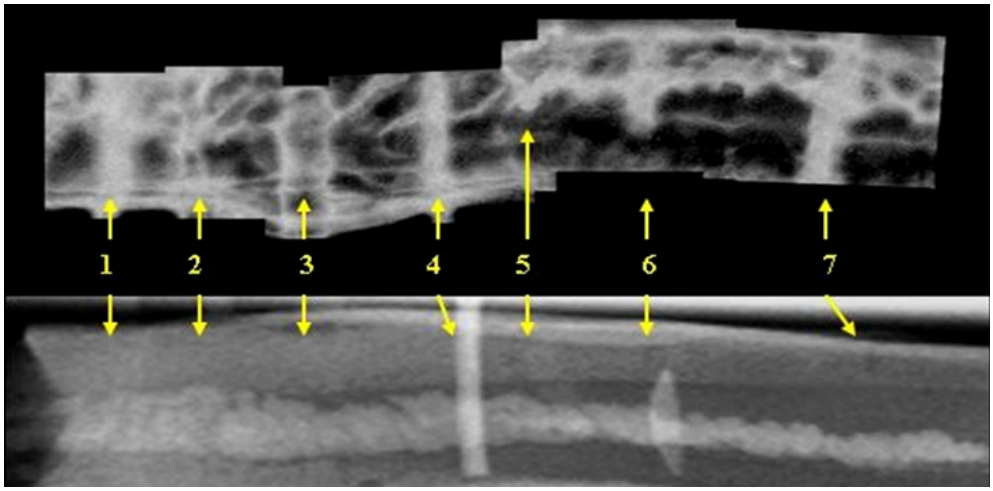

(B)

Figure 5-10. Displays of the inverted C-scan image with film-based radiograph and CR image: (A) C-scan image vs. film-based radiograph and (B) C-scan image vs. CR image. The numbers indicate the foreign objects corresponding to Table 5-1.

5.2.6 Quantitative Analyses

We further analyzed the detectability of the object image by computing the contrast-to-noise ratio (CNR) for each foreign object within the porcine tissue sample per modality. The CNR was computed as follows[120]:

$$CNR = \frac{(f_m - b_m)}{\sqrt{(\sigma_f^2 + \sigma_b^2)/2}} \qquad (5.1)$$

where f_m and b_m are mean intensity values of foreground and background in the image, respectively. The quantities of σ_f and σ_b are the corresponding standard deviations. The measurements are listed in Table 5-2 for all modalities used in the experiment. Bold numbers in Table 5-2 indicate the highest CNR value among all imaging modalities.

Table 5-2. CNR values of each foreign object for all imaging modalities

Object	**No.1**	**No.2**	**No.3**	**No.4**	**No.5**	**No.6**	**No.7**
Material	bamboo	heavy-weight polystyrene	nylon	aluminum alloy-5182	aluminum alloy-3104	glass	extra heavy-weight polystyrene
C-scan Ultrasound	**3.80**	**2.17**	1.71	**8.62**	1.1	**7.51**	**1.76**
B-scan Ultrasound	2.08	1.25	**4.09**	3.84	1.79	1.77	0.47
Film-Based Radiography	1.1	0.2	0.57	7.6	1.12	8.43	0.42
Computerized Radiography	0.2	0.39	0.45	7.27	**3.46**	8.04	0.62

From Table 5-2, we found that for the thin aluminum alloy (No.5) and glass (No.6) objects, radiographs had highest CNR values of 3.46 (CR) and 8.43 (Film-based radiography) as compared to the ultrasound images; for the thicker aluminum alloy (No.4), the CNR values of both radiographs were also over 7. However, their performance in detecting objects Nos.1, 2, 3, and 7 was not considered as observable due to lower CNR values.

The C-scan ultrasound had four highest CNR values of the total seven foreign objects over the other modalities. The CNR value of the thicker aluminum alloy (No.4) and the glass object (No.6) in C-scan images reached 8.62 and 7.51 respectively. The B-scan ultrasound also had one highest value of 4.09 in detecting nylon (No.3). However, only a single cross section of each foreign object can be seen in the conventional B-scan image which makes it less favorable as a device for detecting foreign object in soft tissue. If we consider a CNR value of 1.5 as the contrast threshold, C-scan ultrasound images can clearly see the foreign objects except the thin aluminum alloy (No.5) whose acoustic attenuation is very close to the muscle.

Based on the visual comparisons and CNR analyses, we found that for film-based radiography and CR, aluminum alloys and glass possess highest CNR values; nevertheless, they were clearly visible in both C-scan and B-scan ultrasound images. The

study demonstrated that bamboo, aluminum alloy (5182 series), heavy-weight polystyrene, nylon, and extra heavy-weight polystyrene objects were better detected by ultrasound imaging systems than radiography systems.

Comparatively, the C-scan images were speckle-free and did not have the same degree of geometric distortion as the conventional B-scan ultrasound images. In addition, the structural features of the fat and muscle tissues in the porcine tissue sample were observable in the C-scan, but not in the B-scan images. According to the CNR analysis, the C-scan images had the highest values for four out of seven foreign objects and the three remaining objects were also clearly visible. Hence, the C-scan prototype #2 can provide greater image quality and lead to better clinical detection for many types of foreign objects.

5.3 Small Animal Study

Clinical interpretation of conventional ultrasound images requires both the general acoustic heterogeneity of human organs and the similarity in acoustic properties between normal and abnormal tissues. The small animal study was designed to evaluate the C-scan ultrasound prototype #2 in imaging a live animal and identifying organs and principal body structures. A live mouse, three inches long with fur covering, was selected as the imaging target in the small animal study. Another imaging modality, a small animal MRI[121], was also introduced to obtain the reference MRI images of the same target.

5.3.1 Configuration of the Study

The live mouse with approximate sizes of 10cm × 3cm ×2.5cm (not including the tail) was hung between the ultrasound transducer and the receiving unit in the water tank of the C-scan prototype #2; the mouse's head was above water. The experimental configuration is illustrated in Figure 5-11. The C-scan ultrasound images of the mouse

were obtained by using multiple ultrasound frequencies at 3.5MHz and 5MHz. Both ultrasound projection images and real-time videos were recorded.

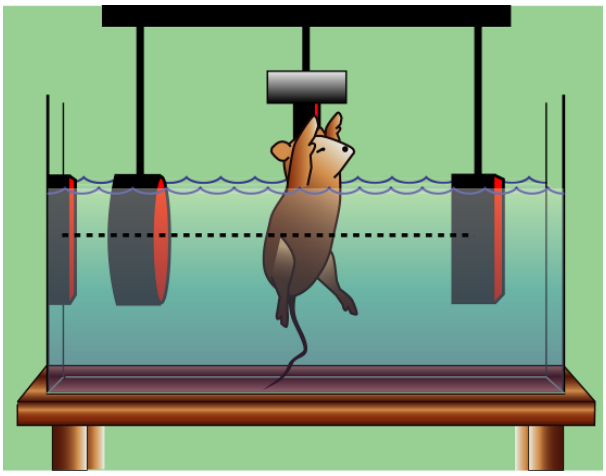

Figure 5-11. A diagram of the system configuration for the small animal study.

5.3.2 Small Animal MRI

A detailed MRI examination of the same live mouse was performed as an imaging reference to the ultrasound study. With the supports provided by Dr. Paul C. Wang, MRI images of the live mouse, as displayed in Figure 5-12, were obtained by the small animal Varian 4.7T system at the Biomedical Nuclear Magnetic Resonance (BNMR) Laboratory at Howard University in Washington, D.C. The live mouse was placed on a supporting plane with electrocardiogram (ECG) wires connected. The ECG curves were monitored during the experiment to generate stable ECG gated MRI images.

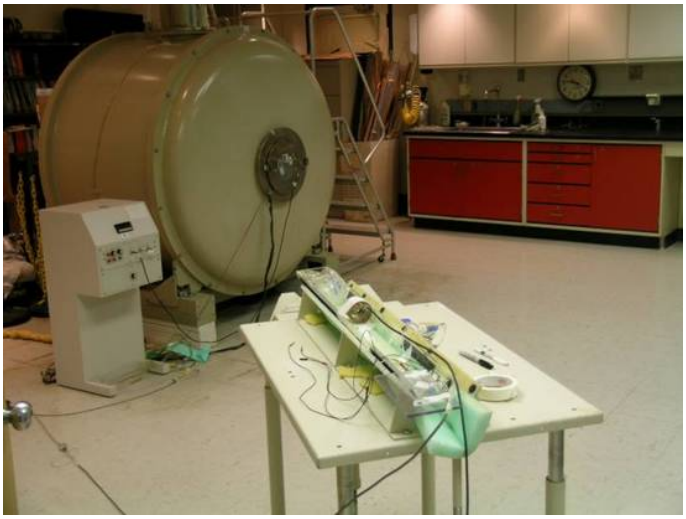

Figure 5-12. Small animal MRI system (4.7 T) at Howard University.

5.3.3 Image Analyses

C-scan ultrasound videos of the beatings of the heart as well as movements of the whole body were captured at frequencies of 3.5MHz and 5MHz. The C-scan ultrasound images were further extracted from a sequence of 2,700 ultrasound images taken at a speed of 30 frames per second for a period of 90 seconds. The beatings of the heart and movements of breath were sampled and illustrated in Figure 5-13. Other images were selected and stitched to be a composite body image of the mouse as illustrated in Figure 5-14(A). The MRI image of the entire mouse body is exhibited in Figure 5-14(B).

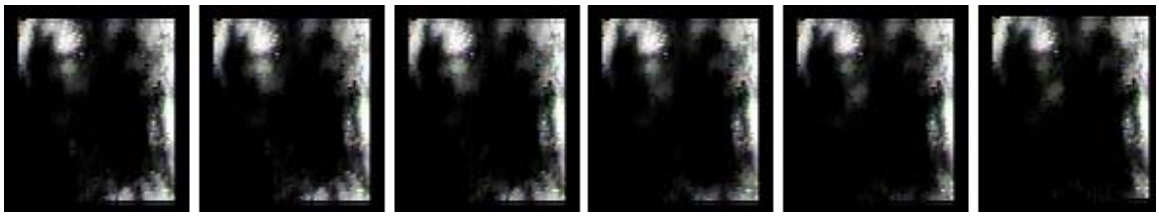

Figure 5-13. Mouse heart beating images and breath movements captured at 3.5 MHz.

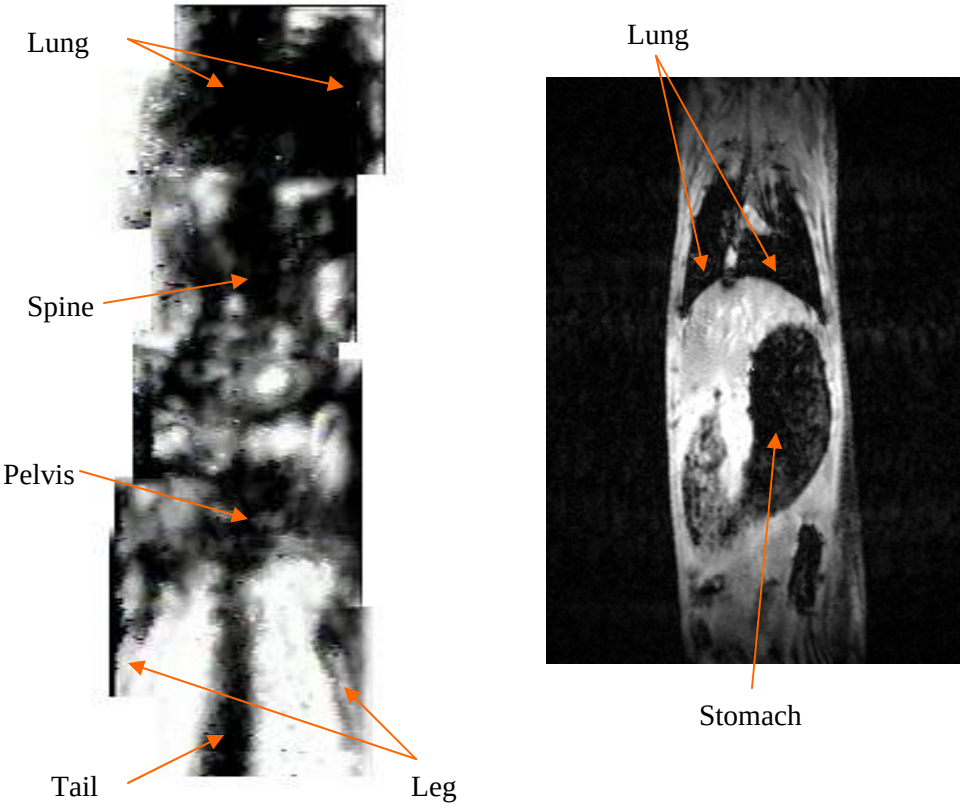

Figure 5-14. The composite C-scan image (left) and the MRI image (right) of a whole mouse body. Individual C-scan images were obtained at 5MHz.

The resolution of C-scan ultrasound images was not as lucid as the MRI images. However, C-scan ultrasound was able to produce real-time images while viewing the beatings of the heart or other direct projections of a specific organ of the mouse. In many cases, live athymic nude mice (lab mice) without fur are the most common targets of animal medical study. The particular live mouse served in this imaging study, however, was three inches long and with fur. Therefore, the thickness of the mouse body and the micro air bubbles underneath the fur were two major influences of the C-scan image quality. The study results indicated that the C-scan ultrasound had the potential in real-time animal medical imaging, for instance on lab mice with tumor or other diseases.

5.4 C-scan Ultrasound Mammography Study

A C-scan ultrasound mammography prototype was designed and fabricated using the I-400 PE-CMOS sensor array. The system was capable to generating projection ultrasound breast images in the “dry” configuration concept. The C-scan mammography prototype equipped with two paddles which were designed for the use of compressing the imaging target to create evenly contact between the transducer, the target, and the detecting unit (see Figures 5-15 A-C). Depending on the thickness of the target, variety frequencies from 1MHz to 10MHz of ultrasound transducers can be installed. Currently, a 4MHz plane wave transducer was located above the upper paddle and the detecting unit was located below the lower paddle of an alignment of the projection geometry. In addition, a handling bar at the right side of the system was constructed to control the imaging position of the transducer-receiver instrument pair.

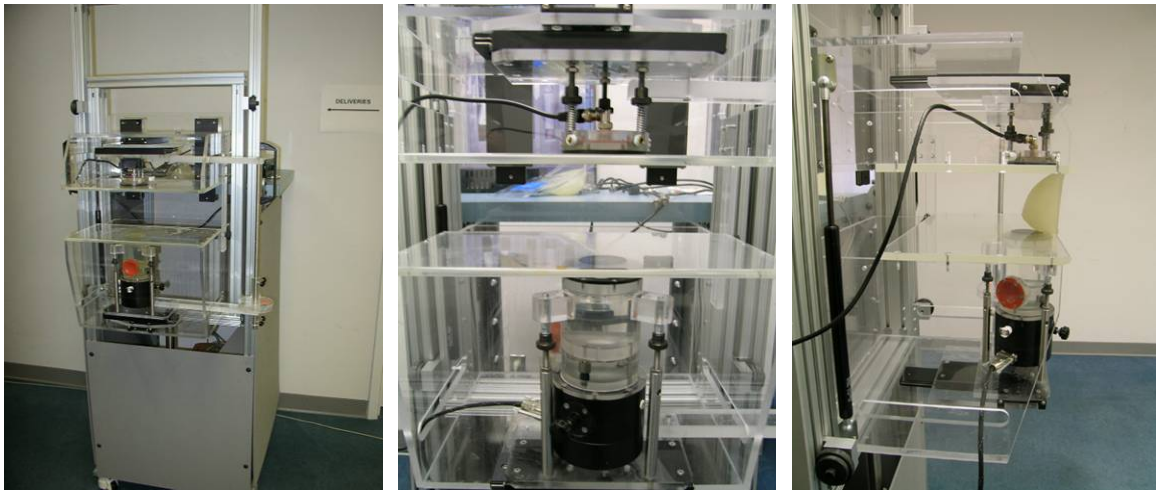

(A) (B) (C)

Figure 5-15. The configurations of first C-scan ultrasound mammography prototype. (A) The front view of the complete system. (B) The closer view of the transducer (top) and detecting unit (bottom). (C) The side view of the system with a breast phantom.

During an actual study with the C-scan ultrasound mammography prototype, medical ultrasound gel or other equivalent liquid is required to be applied on the breast as the transmission medium. The patient would stand in front of the C-scan mammography

prototype while an operator controls the compression of paddles, changes the focus depth of breast, and works with the imaging software. Real-time C-scan images or video clips which cover the entire compressed breast area can be generated while moving the handing bar.

5.4.1 Initial Breast Phantom Test

A CIRS breast phantom, Model 013, was used to perform the initial imaging test (see Figure 5-16). The phantom was compressible and consisted of several simulated tumors and cysts ranging from 0.5cm to 1.5cm embedded in a uniform tissue mimicking material. A proper pressure between the compressing paddles was applied to the breast phantom. The C-scan images of several tumors with varying dimensions of 0.5cm, 0.9cm and 1.2cm are displayed in Figure 5-17. The initial test results indicated that this C-scan mammography prototype can produce potentially clinical useful ultrasound images in the gel-based (dry) configuration.

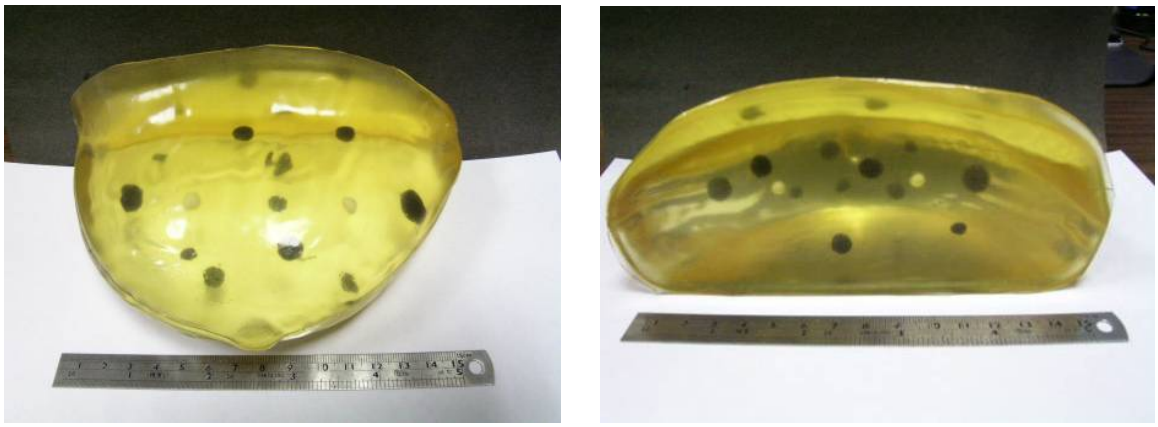

(A) (B)

Figure 5-16. Pictures of the CIRS compressible breast phantom model 013; top view (A) and side view (B).

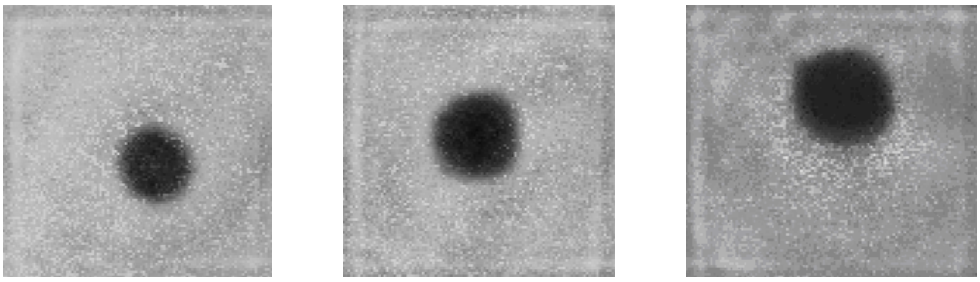

(A) 0.5 cm (B) 0.9cm (C) 1.2cm

Figure 5-17. C-scan images of three simulated tumor with 0.5cm, 0.9cm and 1.2cm contained in the breast phantom using the C-scan ultrasound mammography prototype.

5.4.2 *In vivo* C-scan Images of Human Breast

Ultrasound mammography research with the C-scan ultrasound using I-400 sensor array is currently in the clinical study stage. C-scan images of normal human breasts were captured from several volunteers from Imaging Science and Information Systems (ISIS) Center of Georgetown University. Some of the ultrasound mammographic images are exhibited in Figure 5-18. It is shown that fibrous structures and fatty patterns in brighter areas were observable in these images. However, the clinical validation of those patterns is under future investigation.

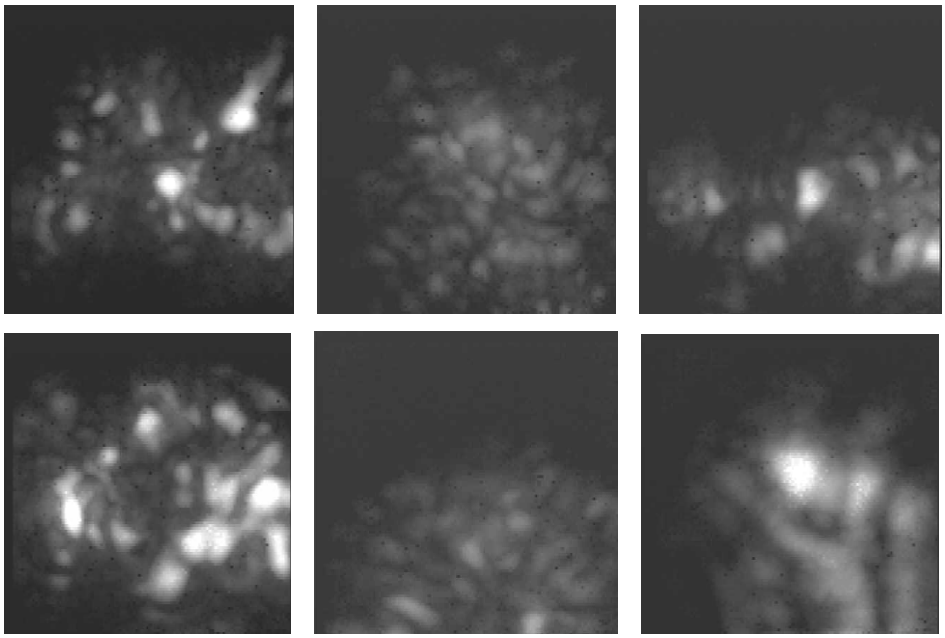

Figure 5-18. C-scan breast images of human breasts acquired by the ultrasound mammography prototype using I-400 sensor array operated at 4MHz.

Further examinations of these images are expected by radiologists from Georgetown University Hospital. During the next stage of clinical study, this C-scan ultrasound mammography prototype will be relocated next to the X-ray mammography system in Georgetown University Hospital for the purpose of future comparative analysis.

5.5 Potential *In vitro* Breast Tissue Examination

5.5.1 *In vitro* Breast Imaging with C-scan Prototype #2

Several breast reduction tissue specimens consisted of fat, fibrous structure, mammary gland, blood vessel, and skin were imaged with the C-scan prototype #2. Sample specimens were obtained from the Georgetown University Hospital. This investigation was designed to learn the appearance of normal mammary tissues in the C-scan ultrasound. Pictures of the sample specimens are displayed in Figure 5-19.

Figure 5-19. Pictures of sample specimens from breast reduction surgery.

The breast reduction surgery yields normal tissue, consisting mainly of fat, but with some glandular tissue and some pieces of skin. The patterns seen in the tissue are predominately lobular, likely representing the lobules of fat. Areas of skin showing skin pores were also visible. These patterns obtained in C-scan images represent the difference of attenuations between the fat tissues and other structures. The image patterns of the reduction mammoplasty specimens greatly resemble the initial *in vivo* breast C-scan images shown above in Section 5.4.2. Particularly the top row, second image shown in Figure 5-20 compares to Figure 5-18. The use of the reduction mammoplasty tissues could possible allows establishing a true correlation of real tissue to image pattern.

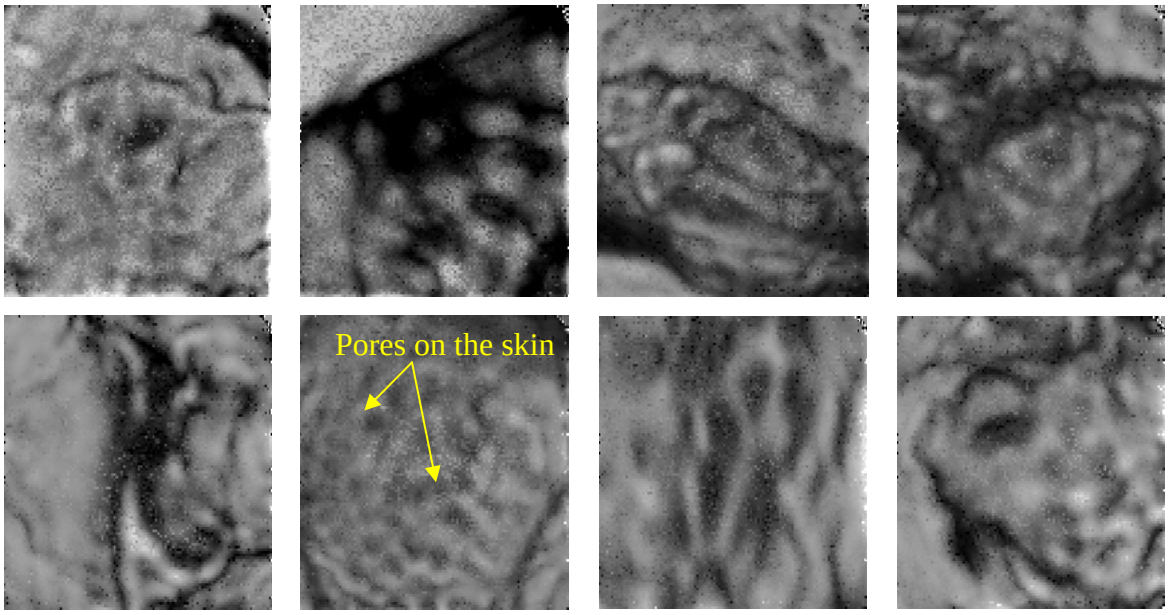

Figure 5-20. C-scan ultrasound images of human breast specimens obtained by the C-scan prototype #2. The image of skin pores from the skin specimen shown in Figure 5-17 (on the right of the second row) is marked above.

5.5.2 *In vitro* Breast Imaging with C-scan Mammography Prototype

During the standard breast biopsy operation, the doctor would remove tissue specimens from the suspicious area. Pathological examination of the specimens is typically conducted by pathologists or is analyzed chemically to determine if the tissues

contain cancer cells. Images of the specimen can provide essential diagnostic information to facilitate the examination.

With the supports provided by Dr. Erini V. Makariou, the C-scan mammography prototype was installed at Betty Lou Ourisman Breast Health Center at Georgetown University Hospital for the breast tissue study. Several breast specimens were directly obtained after the excisional biopsy surgery and C-scan images were taken.

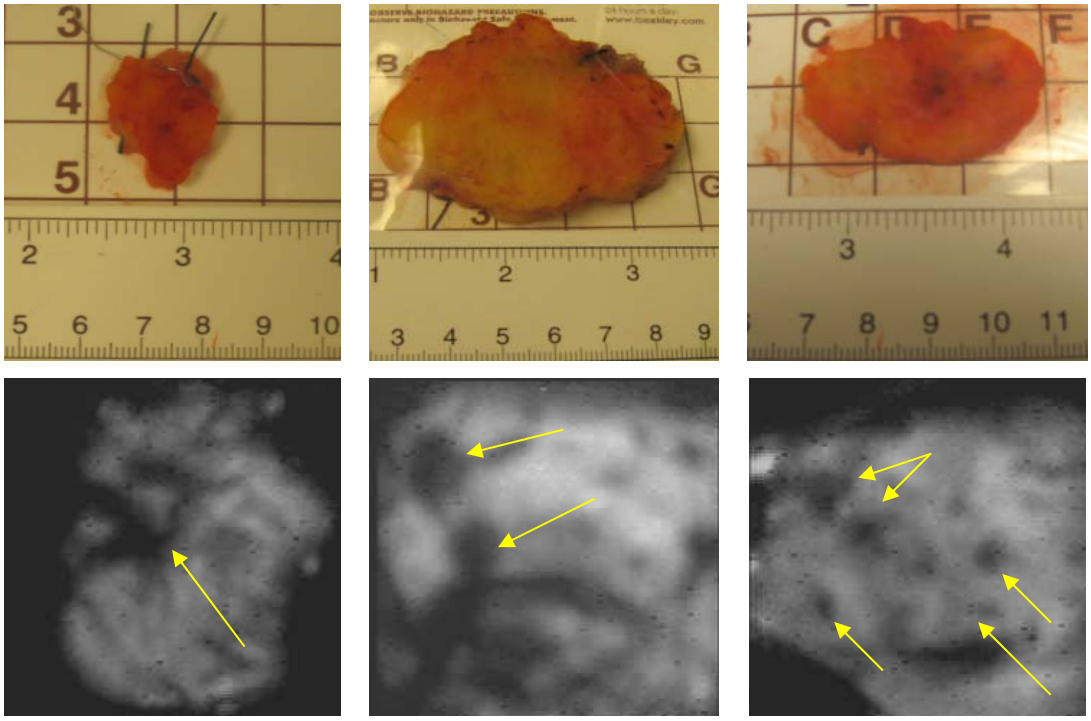

Figure 5-21. Photographs of the breast specimens and their corresponding C-scan images. Arrows indicates the suspicious area in the C-scan images.

Photographs and the corresponding C-scan images of these specimens are illustrated in Figure 5-21. Fibrous structures and masses were identifiable in these C-scan images with higher acoustic attenuations (darker area). These initial C-scan images of the tissue specimens could provide additional attenuation information that is currently unavailable in the B-scan ultrasound. However, clinical and pathological validations of the specimens are not released yet.

5.6 Summary

Ultrasound imaging has been widely used in medical diagnostic applications based on its real-time imaging ability, radiation-free, and non-invasive nature. The C-scan prototypes described in this research have been developed to combine the advantages of using ultrasound as a non-ionizing source and a projection imaging geometry similar to conventional radiography. Investigations of exploring potential medical applications are presented in this chapter.

The real-time ultrasound image guided needle biopsy simulation was performed by C-scan prototype #1 with a CIRS breast phantom (Model 52). The detection of the needle and the target with the C-scan ultrasound is not as sensitive to orientation of the target. Sequences of C-scan needle biopsy images illustrated the biopsy needle paths of puncturing through simulated lesions. Furthermore, the details of needle tracks were also captured by C-scan prototype #1.

In current medical practice, standard X-ray imaging or, less commonly, standard ultrasound device are used to localize the objects to aid in their removal. Radiologist usually detects a foreign object based on it having a different radiodensity (or echo pattern) than normal tissue. In Section 5.2, we performed a comparative study between multi-modalities included C-scan prototype #2, conventional B-scan ultrasound, standard radiography and CR in detecting foreign matters in soft tissue. Based on the quantitative analysis of the CNR value of each foreign object, C-scan ultrasound had the highest value in 4 of 7 samples. The multi-modalities investigation indicate that the C-scan ultrasound imaging, when used for the detection of foreign objects in soft tissues, can be a useful tool in the care of patients with penetrating injuries, both for the detection of and as an interactive imaging tool to facilitate wound treatment.

In Section 5.3, the small animal study demonstrated the ability of capturing real-time images of live animal using C-scan prototype #2. The heart beatings and breath movements of the mouse were captured in real-time at 3.5 MHz. Moreover, the stitched

mouse body image, which was obtained at the ultrasound frequency of 5MHz, was extracted from a 90 seconds real-time video clip covering the whole mouse body. It is demonstrated that the C-scan prototype #2 produced analogous ultrasound images of a live animal in identifying its principal body structures and organs when compared to reference images obtained by a small animal MRI system.

Sections 5.4 and 5.5 illustrated the potential in medical breast imaging of the proposed C-scan prototypes #2 and the C-scan mammography prototype. Fibrous structures, fatty tissues, mammary gland, blood vessel, and skin were identifiable in the initial C-scan breast and specimen images. Some of the patterns seen in C-scan breast images are predominately lobular, likely representing the lobules of fat. It will take additional experience/research in looking both at normal excised tissue and *in vivo* breast imaging to learn what these patterns represent as they differ greatly in contrast from the patterns seen with conventional ultrasound and other standard methods of breast imaging. Accordingly, the true corrections between patterns observed in C-scan images and corresponding pathological information of the breast specimens are yet to be determined.

Chapter 6

Contributions, Future Works, and Conclusions

6.1 Summary of Original Contributions

During this research, three projection ultrasound imaging prototypes, which include C-scan prototypes #1, #2 and a mammography system, were developed and fabricated in collaboration with Imperium Inc. and ISIS Center of Georgetown University Medical Center (GUMC). A series of preliminary simulations, tissue examinations, phantom studies, and ultrasound CT investigations were conducted by these proposed prototypes. In addition, quantitative analyses of the image characteristics were performed and a novel scattering reduction method was developed and investigated. Finally, potential medical applications of C-scan ultrasound were explored.

With the support from mentors and the collaboration with Imperium, I have been involved in hardware designs, software improvements, and exploring potential medical applications are detailed as following:

6.1.1 Hardware Developments

Specifically, quantitative and systematic evaluations were conducted in order to obtain imaging characteristics of C-scan prototypes. Because most of commercially available ultrasound phantoms are designed for conventional reflection systems but not for transmission systems, custom-made phantoms were designed and fabricated for major performance parameters including spatial resolution, dynamic range, contrast resolution, and tissue detectability as well as other important imaging characteristics. Evaluative investigations were subsequently conducted to provide highly valuable yet first-hand data of the unique operating characteristics of C-scan prototypes as well as the PE-CMOS sensor array.

Based on the data obtained from initial system evaluations and quantitative image analyses, we have provided feedbacks and suggestions to the engineers of Imperium Inc. for the developments of the state-of-the-art PE-CMOS sensor arrays. Subsequent improvements were made as a result to enhance the performance of these sensor arrays. Compact and specific imaging prototypes were jointly designed and fabricated with the newly developed sensors. The C-scan prototype #2 performs ultrasound imaging in a wet environment (water-based) and the C-scan mammography prototype supports dry environment (gel-based). These hardware developments make the C-scan ultrasound possible for broader medical uses in diagnostic imaging as encouraged by a National Institutes of Health (NIH) National Institute of Biomedical Imaging and Bioengineering (NIBIB) grant (R21/33 EB02130).

According to preliminary ultrasound CT studies performed by the first C-scan prototype, hardware enhancements associated with accurate system configurations, rotation of transducer-receiver units, and an upgraded sensor array were utilized to build the C-scan prototype #2. Moreover, a high torque micro stepping motor was introduced and integrated to the prototype for the precise control in each rotation step. Study results indicated that these modifications made the C-scan prototype #2 capable of producing potential CT and 3-D ultrasound applications for small objects. This project was awarded

by an Army Breast Cancer Research Program (BCRP) Pre-doctoral Award (DAMD17-01-1-0197).

6.1.2 Software Developments

When performing initial ultrasound CT studies using C-scan prototype #1, we observed circular shadow effects in each reconstructed ultrasound CT slice. Therefore, a shadow compensation method had been investigated to enhance the raw data in the initial UCT study utilizing a computer re-projection reference shadow frame in the sinogram domain. Results indicated that the shadow patterns were significantly reduced. However, this method requires that the target has a relatively uniform base.

Based on the extension of Twersky's multiple scattering theory and the analysis of through-transmitted ultrasound energy, an analytical method, which utilizes an annular aperture to model the ultrasound forward scattering distribution, was developed to improve the quality of C-scan images. Due to the projection configuration of the C-scan ultrasound, the sensor array collects not only the residual of the attenuated primary ultrasound beam but also multiple scattering energies. According to quantitative analyses of the annular C-scan images, forward scattering distributions (FSDs) were estimated for breast mimicking soft-tissue phantoms at varying thicknesses. The normalized FSD for a particular thickness of soft tissue was then applied in the standard image deconvolution processes for several tissue specimens (refer to Section 3.8). The scattering-corrected C-scan ultrasound images were successfully obtained and detail structures were observable. Adapted to our newly developed imaging prototypes and experiment designs, we have provided major mathematical descriptions of the underlying theoretical models, together with detailed numerical algorithm implementations. Both theoretical solutions and experimental data have been produced and compared with excellent match.

The specific objective of this research in performing ultrasound CT and reconstruct 3-D images was successfully accomplished by the C-scan prototype #2 with the I-400 PE-CMOS sensor array. 3-D raw images of two phantoms were constructed.

Moreover, scattering-corrected C-scan images were obtained by applying the analytical scattering reduction method. Accordingly, processed ultrasound CT cross-sectional images were reconstructed to generate the enhanced 3-D ultrasound displays which exhibit more detailed features with fewer artifacts than the raw data.

6.1.3 Exploration of Potential Medical Applications

As compare with other imaging modalities, the proposed C-scan ultrasound has advantages to generate real-time, speckle-free, no geometric distortion, and fluoroscopy-like images and yet non-ionization. Therefore, we have attempted to discover the potential use of C-scan ultrasound in medical applications in this research.

Preliminary investigations of needle biopsy simulation, foreign object detection, *in vivo* live animal imaging, and initial ultrasound CT were conducted in this research. In the initial needle biopsy simulation, C-scan ultrasound displayed real-time imaging-guided capability during the operation. In the comparative multi-modality studies, C-scan prototype #2 provided better detectability in 4 of 7 foreign objects as compared with other imaging modalities which included conventional B-scan ultrasound, filmed-based radiography, and computed radiography. Additionally, a small animal investigation was also accomplished by generating images of a live mouse using the C-scan prototype #2 and a small animal MRI system. We found that major organs and body structures of the mouse were identifiable in the stitched C-scan images.

Subsequently, initial breast imaging and breast tissue examinations were conducted by employing the C-scan prototype #2 and the C-scan mammography system. C-scan ultrasound images of breast phantom, *in vivo* (normal human breast), and *in vitro* human breast specimens (normal breast reduction samples and abnormal samples from biopsy operation) were successfully obtained (refer to Section 5.4 and 5.5). Further investigations and validations using the C-scan mammography prototype, a standard X-ray mammography system and pathological examination of breast specimens will be

jointly performed at the ISIS center and Betty Lou Ourisman Breast Health Center at Georgetown University Hospital.

6.2 Future Works

6.2.1 Ultrasound Forward Scattering Data Bank

Base on the scattering reduction method which estimates the FSD, a scattering distribution data bank is also under further investigation. This data bank will contain scattering distributions of different thicknesses of soft-tissue simulated phantoms of 1cm ~ 8cm at operating frequencies range between 1~10MHz. For instance, while performing a C-scan breast ultrasound imaging, an approximation of the scattering distribution for an average thickness of breast tissue can be pre-selected form the data bank and provide an option to process the “scattering-corrected” C-scan image. Furthermore, we plan to apply this scattering reduction method in a conventional radiography machine in the future.

6.2.2 Investigate Alternative Filtering Methods for Scatter-reduced C-scan Images

In order to enhance the image quality of the scatter-reduced C-scan image (refer to Chapter 3), an alternative filtering method, Wiener filter[122], will be further investigated and employed to suppress the revealed noises. The Wiener filter estimates the local mean and variance around each pixel of the image and then creates a pixel-wise filter using these estimates. Initial results obtained by applying 3-by-3, 5-by-5, and 7-by-7 Wiener kernels to a sample scatter-reduced C-scan image are shown in Figure 6-1 (A-D). The horizontal intensity plots of an edge pattern contained in this image are displayed in Figure 6-1 (E) as well. For this particular image sample, it is shown that the processed image acquired by applying a 5-by-5 Wiener kernel has suppressed the noise patterns yet preserved better edges. The result obtained by employing the 7-by-7 Wiener filter displays a smooth background even though some of the details are wiped out. Thus, the future investigation will be focused on the relationship between the preservation of features and reduction of noises.

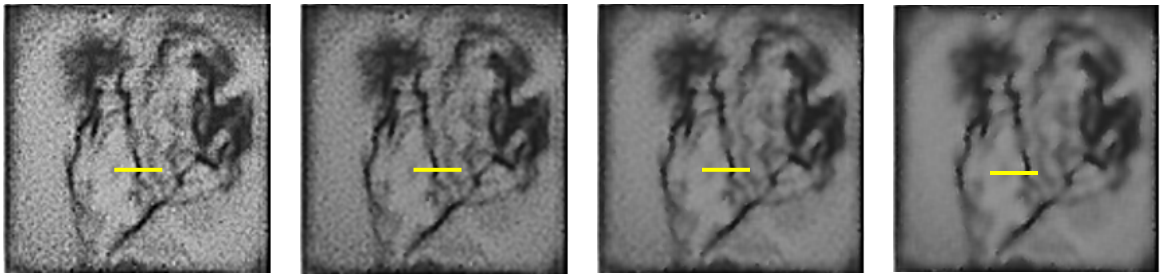

(A) (B) (C) (D)

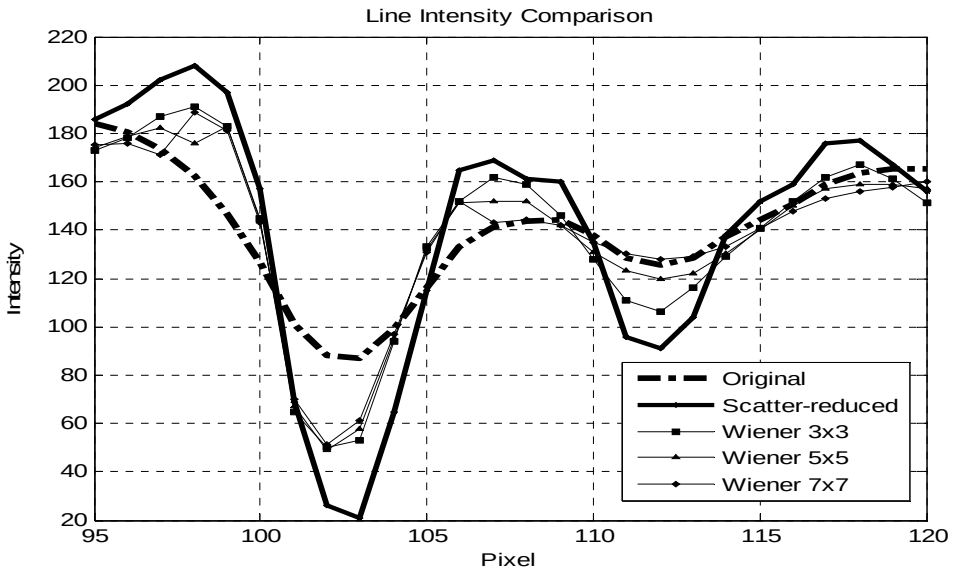

(E)

Figure 6-1. (A) The sample scatter-reduced C-scan image. (B)(C)(D) Initial results processed by 3x3, 5x5, and 7x7 Wiener filter kernels. (E) Intensity plots of an edge pattern contained in those processed images.

6.2.3 Continuous Development of PE-CMOS array

A major component of the C-scan imaging prototype is the PE-CMOS sensor array. The performance of C-scan image is highly dependent on the sensor. With the integration of new sensor technology and improved equipment accuracy, the 6th generation is under construction with significantly improved sensitivity and wider frequency response range. This development allows us to have more varieties in system design and it is possible introduce an acoustic “beam splitter” into C-scan systems. This idea will be addressed in the next section.

We also consider implementing some options for the future sensor design: (1) enlarge the dimensions of array with a larger transducer and new acoustic lens system to cover a wider imaging area (≥ 2 inches square field of view); and (2) increase the density of detecting elements on the CMOS array to improve resolution and accuracy of the ultrasound image. New designs or modifications will be made to upgrade the C-scan system in order to investigate more possible applications.

6.2.4 C-scan Ultrasound in Reflection Geometry

In order to explore the application of imaging subtle bone fractures as well as fine tissue structures, a newly developed laboratory C-scan reflection prototype was fabricated with the following major components: a plane wave transducer, an acoustic beam splitter, an acoustic compound lens system, and a 5^{th} generation PE-CMOS sensor array (model I-500). In the new reflection configuration illustrated in Figure 6-2, the plane wave transducer is placed 45° with the beam splitter. The primary ultrasound beam which generated by the transducer (1) is first passed through the beam splitter, however, only 50% of intensity is propagated toward the target; (2) is attenuated and scattered inside the soft tissue of the target; (3) is reflected from the bone; (4) is attenuated and scattered inside the same soft tissue but in the reverse direction; (5) is passed the beam splitter again but only 50% of the remaining intensity would be delivered toward to lens and sensor; (6) is focused by the acoustic lens onto the sensor array; (7) is converted to voltage by the sensor array; and (8) the voltage on each element of the array is further processed by ROIC for the real-time display.

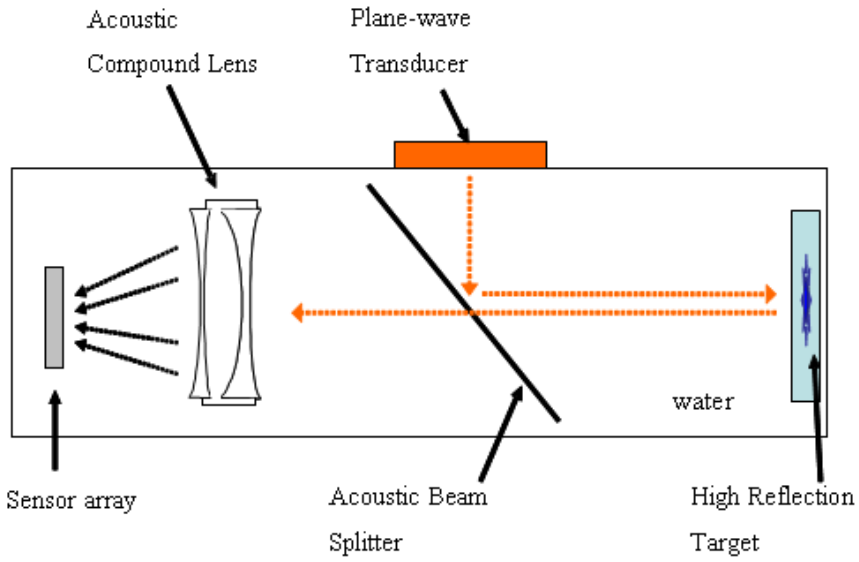

Figure 6-2. A diagram of the laboratory reflection system.

Encouraged by the foreign object study performed with the C-scan prototype #2, a new ARMY Small Business Innovation Research (SBIR) funding (W81XWH-07-C-0021) and a Small Business Technology Transfer Program (STTR) funding (W81XWH-08-C-0117) has just been received to develop a new C-scan ultrasound imaging system for detecting bone hair-line fractures and soft tissue injury. Based on the concept in C-scan reflection geometry, a blueprint of the new compact system design is illustrated in Figure 6-3. With the integration of beam splitter, the dimension of the system is significantly reduced for possible one-hand operation. The dry system configuration makes it possible to be used in the emergency room or in combat environments to facilitate bone fracture detection or wound treatment in extremities. The orientation of C-scan images generated by this reflection system is also different from the cross-sectional representations in the conventional B-scan devices. When this C-scan system is attached to a target, the acquired ultrasound image is parallel to the surface of the target. Further investigations of the image characteristics will be conducted soon.

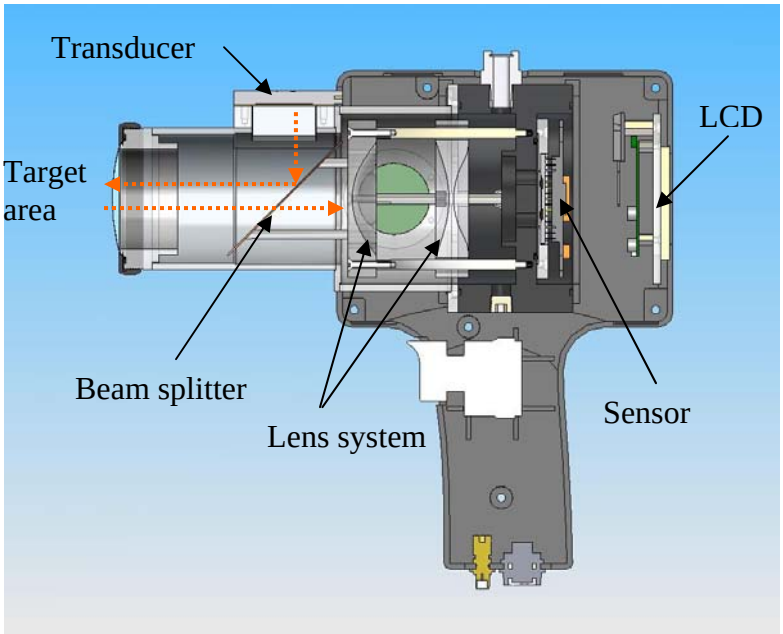

Figure 6-3. A blueprint of the handheld C-scan reflection ultrasound device.

6.3 Conclusions

Developments in the projection geometry and the state-of-the-art PE-CMOS sensor array have enabled the C-scan ultrasound imaging to not only perform well in generating real-time, high resolution and fluoroscopy-like images but also produce images without speckle effects and geometric distortions which are commonly seen in conventional B-scan ultrasound. The C-scan ultrasound is concluded to produce compatible images rival those resulted from other imaging modalities such as conventional B-scan ultrasound, radiography, CR and MRI in specific medical applications. While awaiting additional clinical validation, the innovative C-scan ultrasound prototypes provide veritable value and hold real and imminent promise in medical diagnostic imaging. C-scan ultrasound has demonstrated great perspectives in the evolution of medical domain and the novel PE-CMOS sensor array will likely prove useful in other applications in the future.

Appendix A

A1. Twersky's Multiple Scattering Theory

A uniform medium with volume V containing N random distributed particles located at $\bar{r}_1, \bar{r}_2, \ldots, \bar{r}_N$ is initially considered. Incident waves with a pressure field p are applied to this medium. A pressure field p^a is then taken into consideration which is positioned at $\bar{r}_a$, a location between the scatters. In this instance, p^a denotes the position where the pressure field is observed and the subscript denotes the origin of the field. The pressure field p^a is depicted as the sum of the incident pressure p_i^a and the contributions U_s^a from all N particles at $\bar{r}_s$, s = 1, 2, … N.

$$p^a = p_i^a + \sum_{s=1}^{N} U_s^a \qquad \text{(a.1)}$$

U_s^a is the wave pressure detected at $\bar{r}_a$ and dispersed from the scatterer located at $\bar{r}_s$. U_s^a may also be articulated as p^s is incident upon the scatterer at $\bar{r}_s$. The scattering characteristic u_s^a in this illustration is the measurement of the particle located at $\bar{r}_s$ as observed from the location of $\bar{r}_a$. Alternatively, it can be stated that

$$U_s^a = u_s^a \mathrm{P}^s \qquad \text{(a.2)}$$

where P^s is the "effective pressure field" while plane waves are incident upon the scatterer at $\bar{r}_s$. P^s contains incident wave p_i^s which is scattered from all particles except for the ones at $\bar{r}_s$.

$$\mathrm{P}^s = p_i^s + \sum_{t=1, t\neq s}^{N} U_t^s \qquad \text{(a.3)}$$

By combining Equations (a.1), (a.2), and (a.3), it is apparent that

$$p^a = p_i^a + \sum_{s=1}^{N} u_s^a \mathrm{P}^s \qquad \text{(a.4)}$$

$$\mathrm{P}^s = p_i^s + \sum_{t=1, t\neq s}^{N} u_t^s \mathrm{P}^t \qquad \text{(a.5)}$$

Furthermore, by substituting Equation (a.5) into Equation (a.4), it is now possible to eliminate P from the Equations above and obtain the solution p^a for a specified incident wave pressure p_i with the following:

$$\begin{aligned} p^a &= p_i^a + \sum_{s=1}^{N} u_s^a \left(p_i^s + \sum_{t=1, t\neq s}^{N} u_t^s \mathrm{P}^t \right) \\ &= p_i^a + \sum_{s=1}^{N} u_s^a p_i^s + \sum_{s=1}^{N} \sum_{t=1, t\neq s}^{N} u_s^a u_t^s p_i^t \\ &= p_i^a + \sum_{s=1}^{N} u_s^a p_i^s + \sum_{s=1}^{N} \sum_{t=1, t\neq s}^{N} \sum_{m=1, m\neq t}^{N} u_s^a u_t^s u_m^t p_i^m + \Lambda \end{aligned} \qquad \text{(a.6)}$$

Normally the complete pressure field p^a at $\bar{r}_a$ is composed of the incident wave and all multiple scattered wave pressures. The Twersky's theory, however, incorporates all terms in Equation (a.6) are the summation of all multiply scattered wave pressures which involve of successive scattering propagating through different scatters (see Figure A-1).

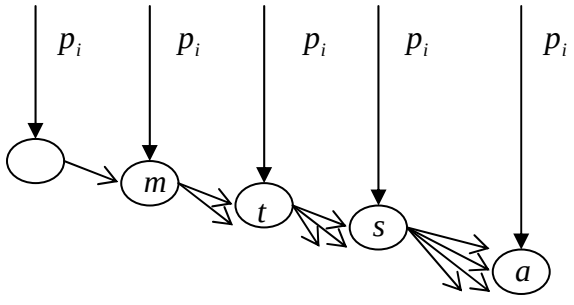

Figure A-1 Chains of successive scattering propagate through different scatters.

A2. Foldy-Twersky's Integral Equation

The total scattering pressure p^a detected at $\bar{r}_a$ can generally be divided into the average field $< p^a >$ and the fluctuating field p_f^a. The average field $< p^a >$ is named the coherent field whilst the square of its magnitude $|< p^a >|^2$ is the coherent intensity. The fluctuating field p_f^a is labeled the incoherent field whilst the square of its magnitude $| p_f^a |^2$ is the coherent intensity. The total intensity is the average of the square of the magnitude of the total field $|< p^a >|^2$ and is equal to the sum of the coherent and incoherent intensities:

$$<| p^a |^2>=<|< p^a > + < p_f^a >|^2>=|< p^a >|^2 + <| p_f^a |^2> \qquad \text{(a.7)}$$

The coherent pressure field $< p^a >$, in accordance with Equation (a.6) and by applying the Foldy-Twersky integral Equation, is illustrated as follows:

$$< p^a >= p_i^a + \int u_s^a < p^s > \rho(r_s) dr_s \qquad \text{(a.8)}$$

where $\rho(r_s)$ is the number of scatters within the volume of dr_s.

A3. Plane Wave Incidence on a Slab of Scatterers

The total intensity $<| p^a |^2>$ defined in Equation (a.7) satisfies the Foldy-Twersky's Equation in (a.8). Therefore

$$<| p^a |^2>=|< p_i^a >|^2 + \int | v_s^a |^2 <| p^s |^2> \rho(r_s) dr_s \qquad \text{(a.9)}$$

and $\qquad v_s^a = u_s^a + \int u_t^a v_s^a \rho(r_t) dt_t$

The symbol v_s^a is an operator and assumptions are defined as the following manner: the density $\rho(r_t)$ is a constant and u_t^a and u_s^a are given by its fat field approximation.

$$u_t^a = f(\hat{i}_{at}, \hat{i}_{ts}) \frac{\exp(ik|r_a - r_t|)}{|r_a - r_t|} \qquad \text{(a.10)}$$

and $$u_s^a = f(\hat{o}, \hat{i}_s) \frac{\exp(ik|r_a - r_s|)}{|r_a - r_s|} \qquad \text{(a.11)}$$

where $\hat{i}_{at}$ is a unit vector in the direction of $r_a - r_t$ and $\hat{i}_{ts}$ is a unit vector in the direction of $r_t - r_s$; $\hat{o}$ is a unit vector in the direction of $r_a - r_s$ and $\hat{i}_s$ is a unit vector in the direction of propagation of total intensity $<|p^s|^2>$.

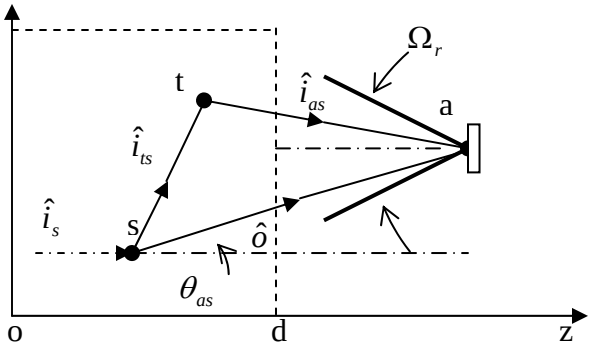

Figure A-2. Geometric illustration of the locations of scatterers and the detector.

An unknown function is defined as following:

$$v_s^t = u_s^a \beta_{as} \qquad \text{(a.11)}$$

$$= u_s^a + \int_0^d dz_t \int_{-\infty}^{\infty} dx_t \int_{-\infty}^{\infty} dy_t u_t^s u_s^t \beta_{ts} \rho \qquad \text{(a.12)}$$

When r_a is located at outside of the slab, the β_{as} function is given by

$$\beta_{as} = 1 + \frac{2\pi i f(\hat{o},\hat{o})\rho}{k(\hat{o},\hat{i}_z)} \int_{z_s}^{d} \exp[i\Delta_{ts}(z_t - z_s)] d_{z_t} \qquad \text{(a.13)}$$

Note that r_t is located at the stationary phase point and therefore $\Delta_{ts} = \Delta_{as} = \frac{2\pi\rho f(\hat{o},\hat{o})}{k\cos\theta_{as}}$ and $\beta_{as} = \exp[i\Delta_{as}(d - z_s)]$. From Equation (a.11), when detecting point *a* is outside of the object ($r_a > d$), we have

$$v_s^a = u_s^a \beta_{as} = f(\hat{o},\hat{i}_s)\frac{\exp(ik|r_a - r_s|)}{|r_a - r_s|}\exp[i\Delta_{as}(a - z_s)] \qquad \text{(a.14)}$$

And therefore,

$$|v_s^a|^2 = |f(\hat{o},\hat{i}_s)|^2 \frac{\exp[-\rho(\sigma_s + \sigma_a)(d - z_s)\sec\theta_{as}}{|r_a - r_s|^2} \qquad \text{(a.15)}$$

where θ_{as} is the angle between $\hat{o}$ and $\hat{i}_s = \hat{z}$, and Ω_r is the solid angle representing the receiving pattern of the receiver. Thus, Equation (a.9) can be written as

$$\langle |p^a|^2 \rangle = \exp[-\rho(\sigma_a + \sigma_s)d]$$

$$+ \rho \int_{\Omega_r} d\Omega_s \int_0^d dz \sec\theta_{as} \, |f(\hat{o},\hat{i}_s)|^2 \exp[-\rho(\sigma_a + \sigma_s)(d - z)\sec\theta_{as} - \rho_a z] \qquad \text{(a.16)}$$

By integrating with respect to z, we have Equation (a.16).

Bibliography

[1] Kremkau, F.W., *Diagnostic ultrasound: principles and instruments*. 6 ed. 2002: W.B. Saunders.

[2] John P McGahan, B.B.G., *Diagnostic Ultrasound*. 2 ed. Vol. 1. 2008, New York: Informa Health Care.

[3] Tempkin, B.B., *Ultrasound Scanning: Principles and Protocols* 3ed. 2009: Elsevier Health Sciences.

[4] Roger C. Sanders, T.C.W., *Clinical sonography: a practical guide*. 4 ed. 2006, Baltimore: Lippincott Williams & Wilkins.

[5] Papadakis, E.P., *Ultrasonic instruments and devices: reference for modern instrumentation, techniques, and technology*. 1999, San Diego: Academic Press.

[6] Jacob Beutel, S.C.H., Yongmin Kim, *Handbook of Medical Imaging: Display and pacs*. 2000: SPIE Press. pp. 278-280.

[7] Rao, N., *"Ultrasound Imaging" in Encyclopedia of Imaging Science & Technology Ed J. Hornak*. 2002: John Wiley & Sons. pp.1412-1435.

[8] Szabo, T.L., *"Diagnostic ultrasound imaging: inside out ", .* 2004: Academic Press. pp. 230-240.

[9] Loizou, C., and Pattichis, C., *Despeckle Filtering Algorithims and Software for Ultrasound Imaging*. Vol. Volume 1 of Synthesis Lectures on Algorithms and Software in Engineering Series. 2008: Morgan & Claypool Publishers. pp. 1-13.

[10] Burckhardt, C., *Speckle in Ultrasound B-Mode Scans.* IEEE Trans. Son. Ultrason., 1978. **25**: p. 1-6.

[11] Meuwly, J.-Y., Thiran, J-P, and Gudinchet, F, *Application of Adaptive Image Processing Technique to Real-Time Spatial Compound Ultrasound Imaging Improves Image Quality.* Investigative Radiology, 2003. **38**(5): p. 257-262.

[12] Huber, S., Wagner, M., Medl, M., et al *Real-time spatial compound imaging in breast ultrasound.* Ultrasound Med. Biol. **28**(2): p. 155-163.

[13] Liasis, N., Klonaris,C. , et al, *The use of Speckle Reduction Imaging (SRI) Ultrasound in the characterization of carotid artery plaques.* European Journal of Radiology, 2007. **65(**3): p. 427-433.

[14] Entrekin, R.R., Porter, B. A., Sillesen, H. H., et al. . *Real-time spatial compound imaging: application to breast, vascular, and musculoskeletal ultrasound.* Semin Ultrasound CT MR. **22**(1): p. 50-64.

[15] Lasser, M.E., Harrison, G. H., *Real-time large-area ultrasound imaging system for aging aircraft inspection.* SPIE Proc., 1998. **3397**(250): p. 250-255.

[16] Lasser, M.E., Lasser, B., Kula J., Rohrer, G., Harrison, G. H., *Developments in real-time 2D ultrasound inspection for aging aircraft.* SPIE Proc., 1999. **3586**(78): p. 78-84.

[17] Lo, S.-C.B., Rich, D, Lasser, M. E., Kula J., Zhao, H., Lasser B., and Freedman, M. T., *C-scan transmission ultrasound based on a hybrid microelectronic sensor array and its physical performance* SPIE Proc. Med. Img., 2001. **4325**(87): p. pp. 89-95.

[18] Liu, C.-C., Lo, S-C. B., Freedman, M. T., Rich, D., Lasser, M. E., Kula, J., Lasser, B., Zeng, J. C. , Ro, D., *Projection ultrasound and ultrasound CT using a PE-CMOS sensor.* SPIE Proc Med Img, 2004. **5373**: p. 61-69.

[19] Liu, C.-C., Lo, S-C B, Freedman, M T, Wang, Y, Rich, D, Kula, J, Lasser, B and Lasser, M E, *Transmission ultrasound computed tomography using a PE-CMOS sensor array: a preliminary animal study*. IEEE Int. Symp. Bio. Img., 2006: p. 908-911.

[20] Liu, C.-C., Lo, S-C B., Freedman, M. T., Wang, Y., Lasser, M.E., Hsieh, T-I., and Sarcone, A., *Investigation of Foreign Objects in Soft-Tissue using a PE-CMOS Ultrasound System: A Preliminary Comparative Study*. SPIE Proc. Med. Img., 2006. **6147**: p. 176-182.

[21] Liu, C.-C., Lo, S-C B., Freedman, M. T., Kula, J., Lasser, B., Lasser, M. E. and Wang, Y., *Transmission and Reflective Ultrasound Images using PE-CMOS Sensor Array*. SPIE Proc. Med. Img., 2005. **5750**: p. 69-76.

[22] Fish, P., *Physics and Instrumentation of Diagnostic Medical Ultrasound*. 1990, West Sussex: John Wiley & Sons, Inc.

[23] Hecht, E., *Optics*. 4 ed. 2002, San Francisco: Addison Wesley. 111-124.

[24] *Quantitative ultrasound: assessment of osteoporosis and bone status*, ed. C.F. Njeh, D. Hans, T. Fuerst, C-C Gluer, and H. K. Genant 1999, London: Martin Dunitz. 50-53.

[25] Crescenti, R.A., Bamber, J. C., Partridge, M, Bush, N. L. and Webb, S. *Characterization of the ultrasonic attenuation coefficient and its frequency dependence in a polymer gel dosimeter*. Phys. Med. Biol., 2007. **52**: p. 6747-6759.

[26] Chivers, R.C., and Hill, C. R., *A Spectral Approach to Ultrasonic Scattering from Human Tissue: Methods, Objectives, and Backscattering Measurements.* Physics in Medicine and Biology, 1975. **20**: p. 799-815.

[27] Parker, K.J., Lerner, R. M., and Waag, R. C. *Attenuation of ultrasound: magnitude and frequency dependence for tissue characterization.* Radiology, 1984. **153**: p. 785-788.

[28] Shrimptont, P.C., *Electron density values of various human tissues: in vitro Compton scatter measurements and calculated ranges.* Phys. Med. Biol., 1981. **26**(5): p. 907-911.

[29] Rayleigh, L., *Theory of Sound* Vol. 2. 1945, Dover, New York.

[30] Morse, P.M., and Ingard, K. U. , *Theoretical Acoustics* 1968: McGraw-Hill

[31] Mie, G., Ann. Physik 1908. **[4] 25**: p. 377.

[32] Kerker, M., *The Scattering of Light and Other Electromagnetic Radiation*. 2 ed. Physical chemistry: a series of monographss. 1969, New York: Academic Press.

[33] Hulst, H.C., *Light scattering by small particles.* 2 ed. Structure of matter series. 1981: Courier Dover Publications. 103-111.

[34] Liu, C.-C., Lo, S-C. B., Freedman, M. T., Rich, D, Lasser, M. E., Kula, J., Lasser, B., Zeng, J. C. , Ro, D., *Projection ultrasound and ultrasound CT using a PE-CMOS sensor.* SPIE Proc Med Img, 2004. **5373**: p. 61-69.

[35] Moulson, A.J., and Herbert, J. M., *Electroceramics: materials, properties, applications*. 1990, New York: Chapman and Hill.

[36] Papadakis, E.P., *Ultrasonic instruments and devices: reference for modern instrumentation, techniques, and technology*. 1999, San Diego: Academic Press.

[37] Shung, K.K., *Diagnostic ultrasound: imaging and blood flow measurements*. 2006, Boca Raton: CRC Press.

[38] Hedrick, W.R., Hykes, D. L. , and Starchman, D. E. , *Ultrasound physics and instrumentation*. 3 ed. Vol. 1. 1995: Mosby.

[39] Moore, J., and Zouridakis, G., *Biomedical technology and devices handbook*. The mechanical engineering handbook series. Vol. 12. 2004, Boca Raton: CRC Press.

[40] Hoskins, P., Thrush, A., Martin, K., and Whitting, T. , *Diagnostic ultrasound: physics and equipment*. 2003, London: Greenwich Medical Media Limited.

[41] Baxter, G.M., Allan, P. L. P. , and Morley, P., *Clinical diagnostic ultrasound*. 2 ed. 1999, Malden: Wiley-Blackwell.

[42] Beutel, J., Kundel, H. L., and Van Metter, R. L. , *Handbook of medical imaging*. Press Monograph Series. Vol. 1. 2000, Bellingham: SPIE Press.

[43] Boreman, G.D., *Modulation transfer function in optical and electro-optical systems*. Tutorial texts in optical engineering. Vol. 52. 2001, Bellingham: SPIE Press.

[44] Patra, S.K., Mishra, N., Chandrakanth, R., and Ramachandran, R., *Image Quality Improvement through MTF Compensation- A Treatment to High Resolution Data*. Indian Cartographer, 2002: p. 86-93.

[45] Lyons, M.E., Chivers, R.C. , and Parker, K.J. , *Absorption dominates attenuation in soft tissues.* IEEE Ultrasonics Symposium, 1986: p. 871 - 874

[46] Lyons, M.E., and Parker, K.J *Absorption and attenuation in soft tissues II-experimental results.* IEEE Trans Ultrason. Ferroelectr. Freq. Control., 1988. **35**(4): p. 511-21.

[47] Michailovich, O.V., and Adam, D. , *A Novel Approach to the 2-D Blind Deconvolution Problem in Medical Ultrasound,*. IEEE Trans. Med. Imag., 2005. **24**(1): p. 86-104.

[48] Taxt, T., *Restoration of Medical Ultrasound Images Using Two-dimensional Homomorphic Deconvolution.* IEEE Trans. Ultrason. Ferroelect., Freq. Control, 1995. **42**(4): p. 543-554.

[49] Vollmann, W., *Resolution Enhancement of Ultrasonic B-scan Images by Deconvolution.* IEEE Trans. Sonics Ultrason., 1982. **29**(2): p. 78-83.

[50] Carotenuto, R., Sabbi, G., and Pappalardo, M. , *Spatial resolution enhancement of ultrasound images using neural networks.* IEEE Trans. Ultrason. Ferroelectr. Freq. Control, 2002. **49**(8): p. 1039-1049.

[51] Kao, C.M., et al *A bayesian approach for edge detection in medical ultrasound images.* IEEE Trans. Nucl. Sci., 1998. **45**(6): p. 3089-3096.

[52] David, J., and Cheeke, N. , *Fundamentals and applications of ultrasonic waves*. CRC series in pure and applied physics. 2002, Boca Raton: CRC Press.

[53] Ensminger, D., and Bond, L., *Ultrasonics: fundamentals, technology, applications*. 3 ed. Dekker Mechanical Engineering Series. Vol. 65. 2008, Boca Raton: CRC Press.

[54] Shung, K., and Thieme, G. A., *Ultrasonic scattering in biological tissues*. 1992, Boca Raton: CRC Press. 75-122.

[55] Van Tiggelen, B.A., and Skipetrov, S. E. , *Wave scattering in complex media: from theory to applications*. NATO Science Series II, Mathematics, physics and chemistry. Vol. 107. 2003, Dordrecht: Kluwer Academic Publishers.

[56] Colton, D.L., and Kress, R., *Inverse acoustic and electromagnetic scattering theory*. 2 ed. Applied mathematical sciences Vol. 93. 1998, New York: Springer.

[57] Milne-Thomson, L.M., *Theoretical hydrodynamics*. 5 ed. 1996, Mineola: Courier Dover Publications.
[58] Longair, M.S., *Theoretical concepts in physics: an alternative view of theoretical reasoning in physics*. 2 ed. 2003, New York: Cambridge University Press.
[59] Ryde, J.W., *The Scattering of Light by Turbid Media- Part II.* Proc. Roy. Soc. (London), 1931. **Ser A 131**: p. 464-475.
[60] Foldy, L.O., *The Multiple Scattering of Waves.* Phys. Rev., 1945. **67**: p. 107-119.
[61] Lax, M., *Multiple Scattering of Waves.* Rev. Mod. Phys, 1951. **23**(4): p. 287-310.
[62] Twersky, V., *On Propagation in Random Media of Discrete Scatterers.* Proc. Amer. Math. Sco. Symp. On Stochastic Processes in Mathematical Physics and Engineering, 1964. **16**: p. 84-116.
[63] Ishimaru, A., *Theory and Application of Wave Propagation and Scattering in Random Media.* Proc. IEEE, 1977. **65**: p. 1030-1061.
[64] Ishimaru, A., *Wave Propagation and Scattering in Random Media*. 1997, New York: IEEE Press.
[65] Wang, Y., and Morris, J. M. , *On Numerical Verification of Time-domain Moment Method in Ultrasound Tomography.* Journal of Biomedical Optics, 1996. **1**(3): p. 324-329.
[66] Dassios, G., Fotiadis, D. I. , Massalas, C. V. , and Kiriaki, K. , *Scattering Theory and Biomedical Engineering Modeling and Applications*. 2000, River Edge: World Scientific Publishing Company.
[67] Kak, A.C., and Slaney, M. , *Principles of Computerized Tomographic Imaging*. 1988, New York: IEEE Press. 275-295.
[68] Kak, A.C., *Computerized tomography with X-ray, emission, and ultrasound sources.* Proceedings of the IEEE, 1979. **67**(9): p. 1245-1272.
[69] Tokumori, K., et al. *Monochromatic X-ray CT using fluorescent X-rays excited by synchrotron radiation*. in *Engineering in Medicine and Biology Society, 2000. Proceedings of the 22nd Annual International Conference of the IEEE*. 2000.
[70] Onishi, Y., et al. *Material discriminated x-ray CT by using conventional microfocus x-ray tube and cdte imager*. in *Nuclear Science Symposium Conference Record, 2007. NSS '07. IEEE*. 2007.
[71] Motomura, N., et al. *Evaluation of a SPECT attenuation correction method using CT data registered with automatic registration software*. in *Nuclear Science Symposium Conference Record, 2003 IEEE*. 2003.
[72] Figueroa, S.D., et al. *Performance characteristics of an integrated small animal SPECT/CT unit*. in *Nuclear Science Symposium Conference Record, 2005 IEEE*. 2005.
[73] Jianguo, Q., et al. *A Multi-Function Compact Small-Animal Imaging System Incorporating Multipinhole Standard and Helical SPECT and Parallel-Hole SPECT*. in *Nuclear Science Symposium Conference Record, 2006. IEEE*. 2006.
[74] Berard, P., et al., *CT acquisition using PET detectors and electronics.* Nuclear Science, IEEE Transactions on, 2005. **52**(3): p. 634-637.
[75] Maramraju, S.H., et al. *An MR compatible PET scanner based on RatCAP for small animal imaging at 9.4 T*. in *Nuclear Science Symposium Conference Record, 2008. NSS '08. IEEE*. 2008.

[76] Le Meunier, L., et al. *High definition PET for cardiac imaging: Preliminary results*. in *Nuclear Science Symposium Conference Record, 2008. NSS '08. IEEE*. 2008.

[77] Bernstein, K.R., et al. *ROC analysis of PET imaging performance of two PET/CT scanners based on lesion detectability in a torso phantom*. in *Nuclear Science Symposium Conference Record, 2006. IEEE*. 2006.

[78] Yasuno, Y., et al. *Real time and full-range complex Fourier domain optical coherence tomography*. in *Biophotonics, 2004. APBP 2004. The Second Asian and Pacific Rim Symposium on*. 2004.

[79] Xiangqun, X., Y. Lingfeng, and C. Zhongping, *Effect of Erythrocyte Aggregation on Hematocrit Measurement Using Spectral-Domain Optical Coherence Tomography*. Biomedical Engineering, IEEE Transactions on, 2008. **55**(12): p. 2753-2758.

[80] Schaefer, A.W., et al., *Real-time digital signal processing-based optical coherence tomography and Doppler optical coherence tomography*. Biomedical Engineering, IEEE Transactions on, 2004. **51**(1): p. 186-190.

[81] Oldenburg, A.L., X. Chenyang, and S.A. Boppart, *Spectroscopic Optical Coherence Tomography and Microscopy*. Selected Topics in Quantum Electronics, IEEE Journal of, 2007. **13**(6): p. 1629-1640.

[82] Ibrahim, F., M. Barbic, and C. Druzgalski. *Stripe Sensor Tomography and application to microcoil Magnetic Resonance Imaging*. in *Health Care Exchanges, 2009. PAHCE 2009. Pan American*. 2009.

[83] Alsindi, N.A., D. Birru, and W. Dong. *Ultra-Wideband Channel Measurement Characterization for Wireless Magnetic Resonance Imaging Applications*. in *Information Sciences and Systems, 2007. CISS '07. 41st Annual Conference on*. 2007.

[84] Hyunjin, P., et al. *Registration methods for histological slides and ex vivo MRI of prostate*. in *Nuclear Science Symposium Conference Record, 2007. NSS '07. IEEE*. 2007.

[85] Norton, S.J., and Linzer, M., *Ultrasonic Reflectivity Tomography: Reconstruction with Circular Transducer Arrays.* Ultrason Imaging., 1979. **1**(2): p. 154-184.

[86] Ermert, H., and Rohrlein, G., *Ultrasound Reflection-Mode Computerized Tomography for In-Vivo Imaging of Small Organs.* IEEE 1986 Ultrasonics Symposium, 1986: p. 825-828.

[87] Ylitalo, J., Greenleaf, J.F., and Bahn, R.C., *Coherent High-Resolution Ultrasound Reflection Mode CT Imaging.* IEEE 1986 Ultrasonics Symposium, 1986: p. 833-836.

[88] Greenleaf, J.F., Johnson, S.A. , and Lent, A.H. , *Measurement of spatial distribution of refractive index in tissues by ultrasonic computer-assisted tomography.* Ultrasound in Medicine and Biology, 1978. **3**(4): p. 327-339.

[89] Lehman, C.D., André, M.P. , et al, *Through transmission US applied to breast imaging.* Academic Radiology, 2000. **7**(2): p. 100-107.

[90] Geenleaf, J.F., Ylitalo, J. , and Gisvold, J.J. , *Ultrasonic computed tomography for breast examination.* IEEE Engineering in Medicine and Biology Magazine, 1987. **6**(4): p. 27-32.

[91] Greenleaf, J.F., Kenue, S.K., et al, *Breast imaging by ultrasonic computer-assisted tomography.* Acoustical Imaging, 1980. **12**: p. 599-614.
[92] Dick, D.E., and et al, *Technical Evaluation of an Ultrasound CT Scanner.* 1977 Ultrasonics Symposium, 1977: p. 176-181.
[93] Jago, J.R., and Whittingham, T.A. , *Experimental studies in transmission ultrasound computed tomography.* Phys. Med. Biol., 1991. **36**(11): p. 1515-1527
[94] Duric, N., and et al. , *Breast Imaging with Ultrasound Tomography: Clinical Results at the Karmanos Cancer Institute.* 2008 International Conference on BioMedical Engineering and Informatics, 2008. **2**: p. 713 - 717.
[95] Hounsfield, G.N., *A Method of An Apparatus for Examination of A Body by Radiation Such as X-ray or Gamma Radiation.* Patent specification 1283915, The Patent Office, 1972.
[96] Kak, A.C., and Slaney, M. , *Principles of Computerized Tomographic Imaging*. 1988: IEEE Press. 49-75.
[97] Herman, G.T., *Fundamentals of Computerized Tomography: Image Reconstruction from Projections*. 2 ed. Advances in Pattern Recognition, ed. S. Singh. 2009, New York: Springer.
[98] Hawkes, P.W., *Advances in imaging and electron physics*. Advances in Imaging & Electron Physics. Vol. 139. 2006, San Diego: Academic Press.
[99] Helgason, S., *The Radon transform*. press in mathematics. Vol. 5. 1999, Cambridge: Birkhäuser.
[100] Gonzalez, R.C., and Woods, R. E. , *Digital image processing*. 3 ed, ed. R.E. Woods. 2007, Upper Saddle River: Pcarson Prentice Hall. 311-387.
[101] Beutel, J., Kundel, H. L.,and Van Metter, R. L. , *Handbook of medical imaging*. Press Monograph Series. Vol. 1. 2000, Bellingham: SPIE Press.
[102] Jähne, B., *Digital image processing*. 2005, New York: Springer. 235-240.
[103] Schreiman, J.S., Gisvold ,J.J. , et al, *Ultrasound transmission computed tomography of the breast.* Radiology, 1984. **150**(2): p. 523-530.
[104] Marmarelis, V.Z., Jeong, J. , et all, *High-Resolution 3-D Imaging and Tissue Differentiation with Transmission Tomography* Acoustical Imaging, 2007. **28**: p. 196-206.
[105] Shull, P.J., *Nondestructive evaluation: theory, techniques, and applications*. Mechanical engineering. Vol. 142. 2002, New York: Marcel Dekker.
[106] Buzug, T.M., *Computed Tomography: From Photon Statistics to Modern Cone-Beam CT*. 2008, Leipeig: Springer.
[107] Hsieh, J., *Computed tomography: principles, design, artifacts, and recent advances*. SPIE Press monograph. Vol. 114. 2003, Bellingham: SPIE Press. 37-90.
[108] Wiegert, J., Rose, G. , et al, *Soft tissue contrast resolution within the head of human cadaver by means of flat panel-based cone-beam CT.* Proc. SPIE Med. Img., 2004. **5368-41**.
[109] Zeng, K., Chen, Z. , et al, *A half-scan error reduction based algorithm for cone-beam CT.* X-Ray Science and Technology, 2004. **12**: p. 73-82.
[110] Lo, S.-C.B., *Strip and Line Path Integrals with Square Pixel Matrix - A Unified Theory for Computational CT Projections.* IEEE Trans. Med. Imag., 1988. **7**(4): p. 355-363.

[111] McPhee, S.J., Tierney, L.M. , Papadakis, M.A. , *Current medical diagnosis and treatment*. 46 ed. Lange Current Series. 2007: McGraw-Hill Professional. 726-745.
[112] D'Amico, A.V., Loeffler, J. S. , and Harris, J.R. , *Image-guided diagnosis and treatment of cancer*. 2003, Totowa: Humana Press.
[113] Xuan, J.-H., Adali, T., Wang, Y., and Siegel, E. , *Automatic detection of foreign objects in computed radiography.* J Biomed Optics, 2000. **5**(4): p. 425-431.
[114] Hwang, J.-J., Quistgaard, J., Souquet, J., and Crum, L. A. , *Portable ultrasound device for battlefield trauma.* IEEE Proc Ultrason Symp, 1998. **2**: p. 1663-1667.
[115] Boyse, T.D., Fessell, D. P., et al *US of soft tissue foreign bodies and associated complications with surgical correlation.* Radiographics RSNA, 2001. **21**(5): p. 1251-1256.
[116] Gibbs, T.S., *The use of sonography in the identification, location, and removal of soft tissue foreign bodies.* J Diag Med Sono, 2006. **22**(5): p. 5-21.
[117] Lewin, P.A., and Busk, H. , *In vivo ultrasonic measurement of tissue properties.* Proc of IEEE Ultrason Symp, 1982: p. 709-712.
[118] Selfridge, A.R., *Approximate properties in isotropic materials.* IEEE Trans Son Ultrason, 1985. **32**(3): p. 381-387.
[119] Wegst, U., *Bamboo and wood in musical instruments.* Annu Rev Mater Res, 2008. **38**: p. 323-349.
[120] Hendrick, R.E., *Breast MRI: fundamentals and technical as*. 2007, New York: Springer. 107-111.
[121] Gavin, P., and Bagley, R.S., *Practical Small Animal MRI*. 2009: Wiley-Blackwell.
[122] Lim, J.S., *Two-Dimensional Signal and Image Processing*. 1990, Englewood Cliffs, NJ: Prentice Hall. p.548.